1-1-2015

Optical and Electronic Interactions at the Nanoscale

Michael Edward Turk
University of Pennsylvania, michaelturk@gmail.com

Optical and Electronic Interactions at the Nanoscale

Abstract
In this dissertation, we discuss optical and electronic interactions in three nanometer scale semiconductor systems in a broadly defined sense. These studies are performed using time-integrated and time-resolved optical spectroscopies and temperature- and field-dependent electrical transport measurements. We first discuss the construction and optimization of an optical apparatus for performing broadband, time-integrated and sub-picosecond fluorescence and absorption measurements. Using this apparatus, we then characterize the impact on the optically-excited carrier relaxation dynamics of cadmium selenide quantum dots due to a surface treatment previously shown to increase interparticle coupling, namely the solution exchange of native, aliphatic ligands for thiocyanate followed by subsequent sample annealing. We find that this ligand treatment leads to faster surface state electron trapping, a greater proportion of surface photoluminescence, and an increased rate of nonradiative decay due to enhanced interparticle coupling. In contrast to trends previously observed at room temperature, we also show that at 10 K the band-edge absorptive bleach is dominated by 1Sh hole occupation in the quantum dot interior. In the second study detailed here, we use this time-resolved photoluminescence apparatus to demonstrate an enhancement of radiative rates in cadmium sulfide nanowires due to plasmonic enhancement from interactions of hot excitons with a concentric electrically conductive silver coating. In the final experiment we return to cadmium selenide quantum dots to investigate the electronic interactions among quantum dots in high-mobility indium-doped field effect transistors at low temperature. We show that application of a gate bias to the transistor to accumulate electrons in the quantum dot channel increases the "localization product" (localization length times dielectric constant) describing transport at the Fermi level, as expected for Fermi level changes near a mobility edge. Our measurements suggest that the localization length increases to significantly greater than the quantum dot diameter and further that application of gate bias decreases the mobility gap separating localized and extended states.

Degree Type
Dissertation

Degree Name
Doctor of Philosophy (PhD)

Graduate Group
Physics & Astronomy

First Advisor
James M. Kikkawa

Keywords
field effect transistor, plasmonics, quantum dots, time-resolved absorption, time-resolved photoluminescence, ultrafast spectroscopy

Subject Categories
Condensed Matter Physics | Nanoscience and Nanotechnology | Optics

OPTICAL AND ELECTRONIC INTERACTIONS AT THE NANOSCALE

Michael Edward Turk

A DISSERTATION

in

Physics and Astronomy

Presented to the Faculties of the University of Pennsylvania

in Partial Fulfillment of the Requirements for the Degree of Doctor of Philosophy

2015

Professor James M. Kikkawa

Supervisor of Dissertation

Professor Marija Drndić

Graduate Group Chairperson

Dissertation Committee

Nader Engheta, H. Nedwill Ramsey Professor, Electrical and Systems Engineering

Charles Kane, Class of 1965 Endowed Term Chair Professor, Physics

Allison Sweeney, Assistant Professor, Physics

Douglas Durian, Professor, Physics

OPTICAL AND ELECTRONIC INTERACTIONS AT THE NANOSCALE

Acknowledgments

All aspects of my work in this dissertation were supported by the U.S. Department of Energy Office of Basic Energy Sciences, Division of Materials Science and Engineering, under Award No. DE-SC0002158.

I would like to thank Jay Kikkawa for the opportunity to partake in the studies described in this dissertation and for his comprehensive and insightful mentorship as an experimental physicist.

Thanks to Patrick Vora, Annemarie Exarhos, Mehmet Noyan, and Jing Cai for working with me on these experiments and for vibrant discussion, help, and friendship. Thank you also to my Penn committees for all of their contributions to this process.

I have been privileged to work with collaborators in the groups of Chris Murray, Cherie Kagan, and Ritesh Agarwal, specifically Aaron Fafarman, Ben Diroll, Ji-Hyuk Choi, Soong Ju Oh, Chang-Hee Cho, and Carlos Aspetti. I am grateful to have had the opportunities to work with them in studying the fascinating systems described in this dissertation.

Thanks go to Rebecca Perry and machinists Harold "Buddy" Borders and Jeff Hancock for their invaluable help at crucial moments during these experiments. Thanks also to Mike Maikowski of Spectra-Physics for his guidance and assistance in keeping our lasers running at peak performance, enabling many of the experiments described here.

Beyond Penn, I would also like to thank Ted Corcovilos, Miloš Milosavljević, Nai-Chang Yeh, and Itai Cohen for their mentorship in my studies at Caltech and Cornell.

Thank you to my parents, Jim and Louise, for your tireless support and love and for always putting your children's educations first. Thank you to my brother, Matthew, for blazing the path and being a sounding board all these years. Thanks also to Cheryl and Mike Jenkins and Carol and Elliot Cole for welcoming me as family and helping me keep perspective along the way. I would also like to thank my friends, whose contributions are

too numerous to count, for reminding me there is more to life than just the laboratory.

Finally, I am deeply grateful to my wife, Katie, for her ceaseless patience and encouragement on the hard days and for celebrating with me on the good days. I could not ask for a better teammate.

ABSTRACT

OPTICAL AND ELECTRONIC INTERACTIONS AT THE NANOSCALE

Michael Edward Turk

Professor James M. Kikkawa

In this dissertation, we discuss optical and electronic interactions in three nanometer scale semiconductor systems in a broadly defined sense. These studies are performed using time-integrated and time-resolved optical spectroscopies and temperature- and field-dependent electrical transport measurements. We first discuss the construction and optimization of an optical apparatus for performing broadband, time-integrated and sub-picosecond fluorescence and absorption measurements. Using this apparatus, we then characterize the impact on the optically-excited carrier relaxation dynamics of cadmium selenide quantum dots due to a surface treatment previously shown to increase interparticle coupling, namely the solution exchange of native, aliphatic ligands for thiocyanate followed by subsequent sample annealing. We find that this ligand treatment leads to faster surface state electron trapping, a greater proportion of surface photoluminescence, and an increased rate of nonradiative decay due to enhanced interparticle coupling. In contrast to trends previously observed at room temperature, we also show that at 10 K the band-edge absorptive bleach is dominated by $1S_{3/2h}$ hole occupation in the quantum dot interior. In the second study detailed here, we use this time-resolved photoluminescence apparatus to demonstrate an enhancement of radiative rates in cadmium sulfide nanowires due to plasmonic enhancement from interactions of hot excitons with a concentric electrically conductive silver coating. In the final experiment we return to cadmium selenide quantum dots to investigate the electronic interactions among quantum dots in high-mobility indium-doped field effect transistors at low temperature. We show that application of a gate bias to the transistor

to accumulate electrons in the quantum dot channel increases the "localization product" (localization length times dielectric constant) describing transport at the Fermi level, as expected for Fermi level changes near a mobility edge. Our measurements suggest that the localization length increases to significantly greater than the quantum dot diameter and further that application of gate bias decreases the mobility gap separating localized and extended states.

Table of Contents

List of Tables

List of Figures

Preface

The following articles were published in connection with work described in this dissertation.

1. Chang-Hee Cho, Carlos O. Aspetti, Michael E. Turk, James M. Kikkawa, Sung-Wook Nam, and Ritesh Agarwal. Tailoring hot-exciton emission and lifetimes in semiconducting nanowires via whispering-gallery nanocavity plasmons. *Nature Materials*, 10:669–675, 2011. doi:10.1038/nmat3067

2. Annemarie L. Exarhos, Michael E. Turk, and James M. Kikkawa. Ultrafast spectral migration of photoluminescence in graphene oxide. *Nano Letters*, 13(2):344–349, 2013. doi:10.1021/nl302624p

3. Michael E. Turk, Ji-Hyuk Choi, Soong Ju Oh, Aaron T. Fafarman, Benjamin T. Diroll, Christopher B. Murray, Cherie R. Kagan, and James M. Kikkawa. Gate-induced carrier delocalization in quantum dot field effect transistors. *Nano Letters*, 14(10): 5948–5952, 2014. doi:10.1021/nl5029655

4. Michael E. Turk, Patrick M. Vora, Aaron T. Fafarman, Benjamin T. Diroll, Christopher B. Murray, Cherie R. Kagan, and James M. Kikkawa. Ultrafast electron trapping in ligand-exchanged quantum dot assemblies. *ACS Nano*, 9(2):1440–1447, 2015. doi:10.1021/nn505862g

Chapter 1

Overview

This dissertation will focus on the interplay of confinement and localization at the nanometer scale, two phenomena that lead to novel and exciting avenues of research in semiconductor physics and optoelectronics. A particle is said to be localized if it has a well defined position in space; as we will discuss, localization can arise in physical systems for several reasons including both energetic and spatial disorder in the potential landscape. The concept of confinement, in the sense of limiting the spatial extent of a system to less than it would naturally occupy, is closely related and produces fascinating phenomena as we will discuss below.

Confinement, in general, becomes relevant to a physical system when the mean free path decreases to the wavelength scale of an excitation. At such a length scale, constructive interference for longer wavelength excitations is no longer possible upon propagation through a system; this condition defines the minimum energy of permissible standing waves via the dispersion relationship

$$E = E(\vec{k}) = E\left(\frac{2\pi}{\lambda}\right) \tag{1.1}$$

where $\vec{k}$ is the wavevector of an excitation in the system and λ is the wavelength of such an

oscillation, in an isotropic system. For macroscale systems, the De Broglie wavelength is defined by $\lambda = \frac{h}{p}$ where h =6.626 $\times 10^{-34}$ J s is Planck's constant, and p is the classical momentum of the object given by $p = mv$ with m mass and v velocity.

Ekimov and Henglein in the 1980's showed that confinement leads to size-dependent optical properties in nanocrystalline semiconductors.[45] As summarized by Efros and Efros,[46] the magnitude of this size-dependent confinement energy depends on the relative size of the nanocrystal radius a compared to the Bohr radius a_B of the bulk exciton in the semiconductor, where a_B is defined as

$$a_B = \hbar\kappa/\mu e^2 \tag{1.2}$$

with κ the bulk dielectric constant of the semiconductor, $\mu = \frac{m_e m_h}{m_e + m_h}$ the reduced mass of the exciton, and m_e and m_h the effective masses of the conduction band electron and valence band hole, respectively. With regard to quantum dots, we will focus here on the strong confinement regime where $a_B \gg a$ and the allowed optical transitions occur at discrete energetic positions which are determined by the radius a (Chapter 2). In Chapter 3 we describe the construction and optimization of an optical apparatus tailored to measure the ultrafast electron and hole relaxation dynamics in strongly confined semiconductor nanocrystals made of cadmium selenide which have tunable optical spectra in the visible range.

Chapter 4 describes our low-temperature studies of close-packed CdSe quantum dot solids under several different ligand treatment and annealing conditions. As synthesized, the quantum dots are passivated by long, aliphatic, insulating ligands. A ligand exchange and annealing process developed by our collaborators was shown enhance the electronic coupling among nanocrystals, and in these experiments we study how the structual and chemical changes induced by this process impact carrier relaxation dynamics and lead to

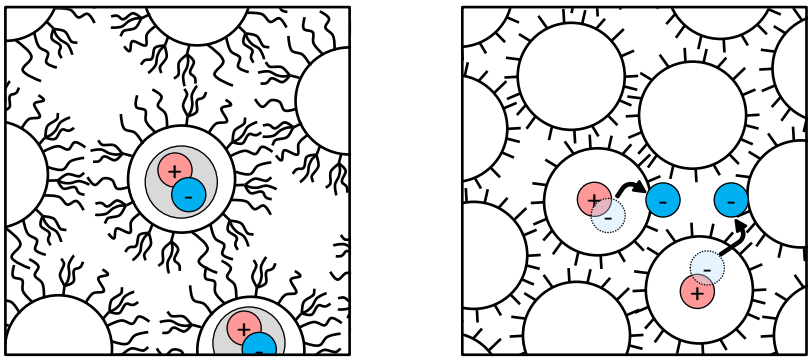

Figure 1.1: Cartoon schematic of randomly close-packed nanocrystal films studied in optical experiments. Left: long, insulating, aliphatic ligands separate quantum dots when drop cast as synthesized, and photo-excited charges remain as excitons in the QD core to long times. Right: exchanged and annealed films show spectroscopic evidence of fast electron trapping.

fast electron trapping from the quantum dot core to surface states (Figure 1.1).

Similarly, confinement can also enhance the coupling between electron plasma oscillations in a metal at a metal-dielectric interface and optical fields.[11, 224] These collective excitations are known as plasmons, and such surface confinement permits channeling of light at length scales shorter than the optical wavelength in free space.[73] In contrast with dielectric waveguides such as optical fibers, decreasing the lateral dimensions of a plasmonic waveguide can decrease the external extent of the mode. The trade-off of such increased confinement is increased excitation dissipation rates and reduction in phase and group velocities. Spatially tapered metallic nanostructures are commonly used to achieve this mode confinement, and enhancements of local field strength by factors of one-thousand can be achieved dependent on the nanoscale surface quality and termination of the structure. For plasmons, confinement and localization are clearly intertwined, and in Chapter 5 we will discuss one such example of tailored interactions between confined surface plasmons and the radiative rate of cadmium sulfide nanowires. These nanowires are coated with

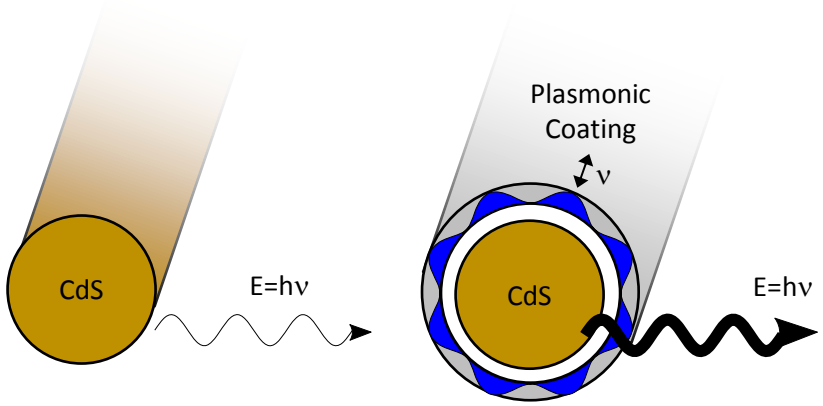

Figure 1.2: The radiative rate of cadmium sulfide nanowires (left) is enhanced by coating with a silica insulating layer and an outer silver plasmonic coating (right). By tuning the diameter of the CdS core, whispering-gallery resonances develop in the electron plasma of the silver layer.

a small insulating layer of silicon dioxide and a conductive coating of silver; the CdS nanowire diameter can be tuned to create a plasmon resonance in the surrounding silver coating. As depicted schematically in Figure 1.2, This resonance dramatically increases the radiative rate, thereby both increasing the total photoluminescence and decreasing the duration of this photoluminescence.

Although not the focus of this Dissertation, the impacts of confinement also arise in other situations such as changes to the vibrational phonon spectra available in a system. Calculations of the bulk phonon spectra assume that infinite plane waves are possible, so the reduction in dimensionality modifies the permitted phonons if the external medium to the physical system does not have an overlapping phonon spectrum. This type of confinement becomes relevant only at very small length scales of several tens of lattice parameters.[7] In nanocrystalline materials the Raman spectra are typically broadened with a dispersion-dependent energy shift. For single-walled carbon nanotubes (SWNTs) which have a hollow center, the chirality of the nanotube controls the periodicity and thereby

the phonon dispersion spectrum leading to a rich spectrum of optical, acoustic, and radial breathing modes.[41] The finite size, structural asymmetry, and stoichiometry all complicate the determination of this phonon spectrum.

The discussion in this Introduction so far has focused on phenomena that arise due to physical confinement in electrical and vibrational systems. Localization is a counterpart to confinement, and whereas confinement refers to the collection of states available in a system under a set of restrictive conditions, localization is characterized by lack of diffusion in the absence of an impetus.

The physical mechanism underlying electronic localization varies with experimental conditions, whether it is the disorder in site position from one site to another (Mott localization) or disorder in the energetic landscape at regularly spaced sites (Anderson localization), but the net result is similar in both cases. In a localized electronic state, the system requires some source of activation energy for transport (of whatever physical form) to occur. In electronic systems, the lack of an activation energy is the key difference between metals and insulators: transport in metals is activationless, such that, even in the absence of thermal energy to randomly excite carriers into the conduction band, electrical transport can still occur. Therefore, it should be noted that while the resistance of a metal may still vary with temperature and increase as temperature decreases, any material with finite conductivity at zero temperature will necessarily be defined as a metal.

Although Anderson initially proposed his theory of localization in the context of electronic transport, Anderson localization is not limited to electronic systems.[139] Indeed, a classical wave version of the same phenomenon exists where the energy of the wave replaces the electron energy, and signs of localization are present in the field intensity distribution. In cold atomic gasses, laser speckle has been used to produce spatial disorder in the potential landscape which can be controlled; the level of diffusion was shown to vary with amplitude of the applied disorder potential.[14] Macroscopic disorder in a thin

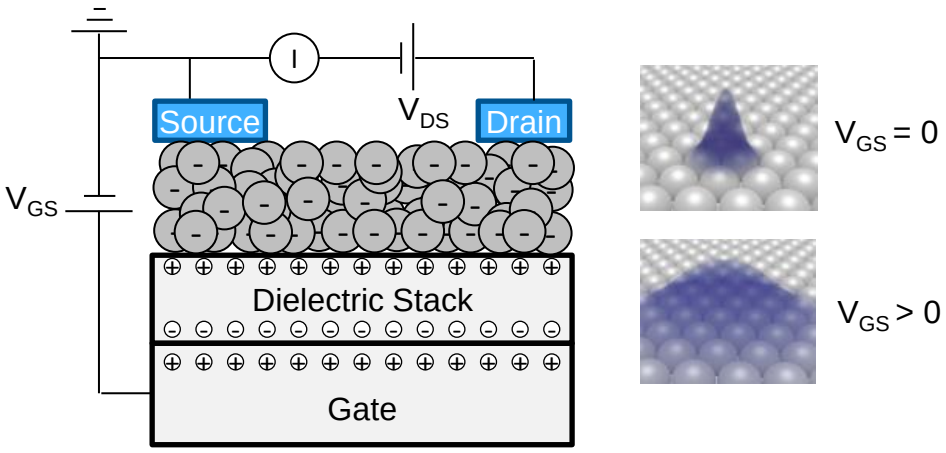

Figure 1.3: Left: quantum dot field effect transistor schematic. Right: application of a gate bias delocalizes the electron across multiple quantum dots.

aluminum plate was also shown to localize acoustic waves at sufficiently low frequency such that diffusion is strongly impeded when the wavelength is comparable to the mean free path.[239] This scale-dependent diffusion is a marker of Anderson localization in classical systems. Scale-dependent and time-resolved diffusion measurements also showed that light transmission through systems with a mean scattering length comparable to the light wavelength also undergo an Anderson transition.[241, 219] Localized modes have even been predicted to exist in photonic bandgap systems in the presence of a certain level of disorder.[32]

In Chapter 6 we provide a broad overview of localization and transport in disordered materials in general and nanocrystalline materials specifically, and in Chapter 7 we study a system that combines electronic confinement and tunable localization. We describe temperature and magnetic field transport studies of quantum field-effect transistors that were developed by building upon the ligand treatments studied in Chapter 4.[27, 28] Whereas Chapter 4 focuses on exciton interactions with surface states and ligands and Chapter 5

studies exciton interactions with resonant electron plasma oscillations in a conductive cavity, Chapter 7 investigates the interplay of the confinement and localization as one approaches the transition to delocalized states through tunable control of the Fermi level, concluding our study of the interplay of confinement and localization in optical and electronic systems.

Chapter 2

Introduction

Colloidal semiconductor quantum dots (QDs) are of broad interest due to the composition, size, and shape tunability of their optical and electronic properties produced in part by the spatial confinement of the wavefunction.[222, 184] Numerous excellent reviews and books have been written on the theory and experimental history of semiconductor quantum dots,[131, 45, 120, 232, 180, 222, 240, 130, 70] and here we provide only a brief overview as is necessary to understand the experiments described in this Dissertation.

As alluded to in Chapter 1, quantum dots straddle a very interesting point between bulk semiconductors and individual molecules. At macroscopic length scales, the electronic bandstructure is well approximated by the properties of an infinite periodic lattice. In contrast, in molecular form the precise quantum mechanical interactions of atomic orbitals determines the permitted electronic energy states and relevant relaxation dynamics. Colloidal quantum dots are particles, typically composed of up to several thousand atoms, in which the natural length scales of the electron and hole are similar to or larger than the length scale of the particle.[177] This particle confinement discretizes the continuum of states in momentum space that is otherwise available, and the surrounding insulating medium imposes a restriction that the wavefunction must decay outside of the confines of

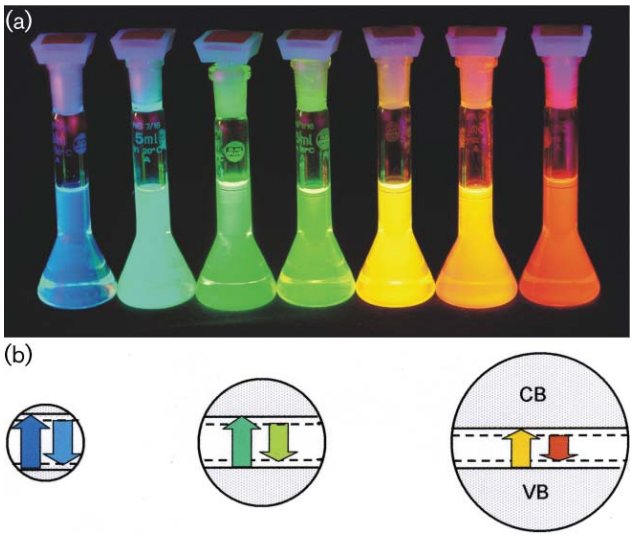

Figure 2.1: (a) Photoluminescence of CdSe-CdS core-shell quantum dots with diameters from 1.7 nm (blue) up to 6 nm (red). (b) Schematic demonstrating the size-dependence of absorption (up arrow) and photoluminescence (down arrow) where longer arrows represent higher energy transitions. Reproduced from Ref. 201 with permission of The Royal Society of Chemistry.

the quantum dot. Thus, by tuning the size of the nanocrystal, the confinement potential concomitantly changes and the energy of allowed states changes as well. Figure 2.1 shows the photoluminescence (PL) from a size series of quantum dots excited by ultraviolet light, demonstrating the tunability of the bandgap separating the lowest conduction band and highest valence band state.

2.1 Quantum Size Levels

The regime of confinement depends on the relative size of several scales: a_{phys}, a_e, a_h, and a_{exc}, the physical radius of the particle and the Bohr radii of the electron, hole, and exciton, respectively.[177, 46] The Bohr radii a_x are defined by

$$a_x = \frac{\kappa m_e a_0}{m^*} \tag{2.1}$$

where m^* is the effective mass of the particle under consideration (using the reduced mass $m_{exc} = m_e m_h/(m_e + m_h)$ for the exciton), $a_0 = \frac{4\pi\varepsilon_0\hbar^2}{m_e e^2}$ is the Bohr radius of the Hydrogen atom, κ is the dielectric constant of the medium, and m_e is the mass of the electron. We are principally concerned with the *strong confinement* case for which a is smaller than all of these radii.

The first approximations of the allowed wavefunctions in a spherical quantum dot are found by considering the solutions to an infinite confining potential $V(r)$ of radius a[46]:

$$V(r) = \begin{cases} 0 & \text{for } r < a \\ \infty & \text{for } r > a. \end{cases} \tag{2.2}$$

Such a model ignores many intricacies of physical quantum dot systems, but it provides a strong starting point for discussion and a nomenclature for discussing the permitted electron and hole orbitals. The solutions of the Schrödinger equation in 3D for such a spherically symmetric infinite potential are of the form[177]

$$\phi_{n,l,m}(r,\theta,\phi) = C_{n,l}\frac{j_l(k_{n,l}r)Y_l^m(\theta,\phi)}{r} \tag{2.3}$$

with $C_{n,l}$ a normalization constant, Y_l^m the spherical harmonic of order m and degree l, and $j_l(k_{n,l}r)$ the l^{th} order spherical Bessel functions. The spherical bessel functions are scaled by

$$k_{n,l} = \frac{\alpha_{n,l}}{a} \tag{2.4}$$

such that wavefunction has a node at the radius a of the nanocrystal, with $\alpha_{n,l}$ the n^{th} zero of j_l. The energy of a particle with mass m with such a wavefunction is given by

$$E_{n,l} = \frac{\hbar^2 k_{n,l}^2}{2m} = \frac{\hbar^2 \alpha_{n,l}^2}{2ma^2} \tag{2.5}$$

Application of this particle-in-a-sphere model to quantum dots requires the effective mass approximation (EMA). Using E_g to represent the bandgap of the material in the bulk, in this approximation the energy of an exciton in such a QD is given by

$$\begin{aligned} E_{exciton} &= E_g + E_h(k) + E_e(k) \\ &= E_g + \frac{\hbar^2 k^2}{2m_h^*} + \frac{\hbar^2 k^2}{2m_e^*} \end{aligned} \tag{2.6}$$

where m_h^* and m_e^* are the effective masses of valence band holes and conduction band electrons, respectively, determined by the parabolic curvature of the band structure in bulk near the band edge. The allowed values of k are determined by the zeroes of the Bessel functions j_l in Equation 2.4; quantum dots with smaller diameters more strongly confine the wavefunctions and thereby have higher energy discretized states. This size-dependent confinement can be seen visually by comparing the photoluminescence of a series of CdSe-CdS core-shell quantum dots with varied diameters, as shown in Figure 2.1.

The excitonic states of the QD are frequently referenced by the quantum numbers of the constituent electron and hole in the effective mass approximation using the notation of nL_J where n reflects the number of radial nodes in the envelope wavefunction of the QD, L represents the angular momentum of the envelope wavefunction can be $(0 = S)$, $(1 = P)$, $(2 = D)$, etc., and J is the unit-cell angular momentum of the hole or electron. Considering cadmium selenide, while the conduction band arises from twofold degenerate s-type orbitals of the cadmium atoms, the sixfold degenerate valence band arises from the p-type orbitals of the selenium atoms.[50] A valence band hole has angular momentum contributions from the constituent spin of the hole ($s = 1/2$) and from the atomic p-type orbitals with $l = 1$. Therefore, after accounting for spin-orbit coupling, the angular momentum of a hole in bulk can be $J_h = 3/2$ or $J_h = 1/2$. Similarly because the bulk conduction band electron is composed of s-type orbitals, the angular momentum J_e of the electron will always be

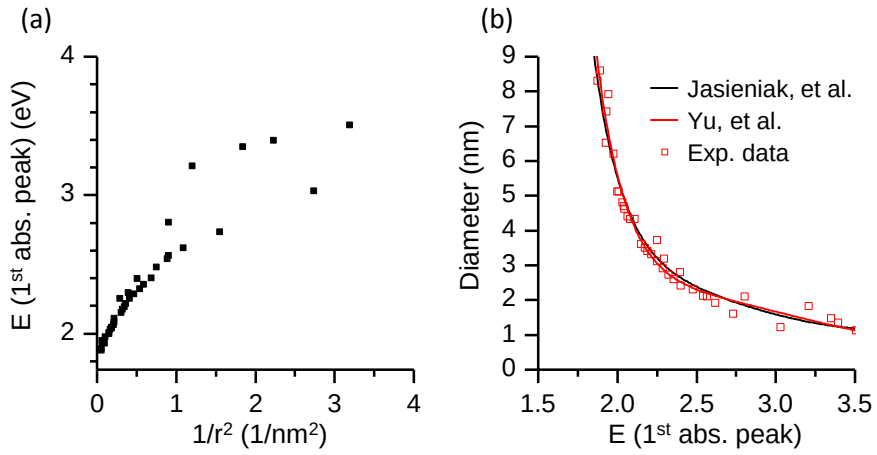

Figure 2.2: (a) Energy of first absorption feature in CdSe quantum dots vs. $1/r^2$. (b) Measured diameter of quantum dot vs. energy of first absorption feature. Black line from Jasieniak, *et al.*,[97], red line from Yu, *et al.*,[250]. Experimental data points taken from Refs. 250, including points from Refs. 217, 168, and 187.

$J_e = 1/2$. This simple picture of an infinite spherical potential neglects many complications such as coulomb repulsion, crystal field splitting in the crystal lattice, and the exchange interaction between the electron and hole. [177, 242]

Comparing the experimentally observed size dependent energies of the first absorption feature with $1/r^2$ (Figure 2.2a), we see that the size-dependence is clearly more complicated than a simple single-band effective mass approximation which would appear as a straight line on this plot. Experimental data points were extracted from Ref. 250, including points from Refs. 217, 168, and 187.

Several empirical reference equations are available to determine the quantum dot diameter using the absorption peak position and electron microscopy-determined sizes. Yu, *et al.*, (Equation (2.7)) and Jasieniak, *et al.*, (Equation (2.8)) provide the following empirical formula to determine the CdSe QD diameter D based on central absorption wavelength λ in

nanometers.[250] These two relations are very similar and are both plotted in Figure 2.2b.

$$D = (1.6122 \times 10^{-9})\lambda^4 - (2.6575 \times 10^{-6})\lambda^3 + (1.6242 \times 10^{-3})\lambda^2 - (0.4277)\lambda + (41.57) \quad \text{(Yu)} \tag{2.7}$$

$$D = (1.62974 \times 10^{-9})\lambda^4 - (2.85743 \times 10^{-6})\lambda^3 + (1.8873 \times 10^{-3})\lambda^2 - (0.54736)\lambda + (59.60816) \quad \text{(Jasieniak)} \tag{2.8}$$

The $\vec{k} \cdot \vec{p}$ perturbative model, using the Luttinger Hamiltonian,[153][152] provides a more accurate picture of quantum dot states for $\vec{k}$ near 0. Numerous groups have contributed greatly to the theoretical calculations of wavefunctions and dynamics in CdSe QDs using atomistic, empirical pseudopotential, and ab-initio calculations.[173, 20, 21, 171, 59, 57, 56, 210] These calculations allow for detailed investigations of theoretical expectations of exciton and biexciton decay, multiexciton recombination, Auger processes, and trapping to surface states (Section 2.3). Seminal papers by Ekimov, *et al.*,[50] and Norris, *et al.*,[178] use the methods of Kane[110] to demonstrate impressive connections between theory and experimental observations of size-dependent optical transitions.

Norris, *et al.*, used photoluminescence excitation (PLE) to trace the positions of the spectrum of energy levels in CdSe QDs. The size-dependent positions of many states are shown in Figure 2.3. In this experiment, Norris produced a range of CdSe QD sizes and observed the modulation of PL at the band edge as the excitation energy was varied, observing a rich spectrum of transitions. We note that due to a mixing of valence subbands that mixes states with angular momentum l_h with $l_h + 2$ (i.e. mixing S ($L_h = 0$) and D ($L_h = 2$)), a modification of the notation described above for hole states is necessary because only parity and the total angular momentum $F = L_h + J$ are conserved: nL_F.[178] The electron wavefunction involves only one band and is still well represented by nL. These PLE

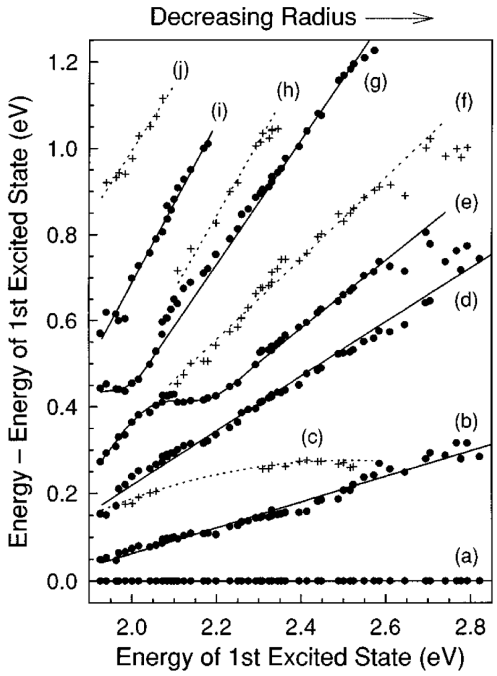

Figure 2.3: Optical transitions in CdSe quantum dots vs. energy of first excited state. Reprinted figure with permission from D. J. Norris and M. G. Bawendi, Physical Review B, 53, 16338, 1996. Copyright 1996 by the American Physical Society.[178]

studies were extended, using fluorescence line narrowing, to observe the size-dependence of the fine structure in the band-edge $1S_{3/2h}1S_e$ exciton as discussed in Section 2.2.[179]

2.2 Fine Structure and the Dark State

Studies of the fine structure have been very important in understanding relaxation kinetics of CdSe nanocrystals.[43, 175, 179, 242, 21] As shown in the right panel of Figure 2.4, the lowest energy exciton, $1S_{3/2h}1S_e$, is split by crystal symmetry and the exchange interaction, and the appropriate quantum number becomes $N = F_h + F_e$ where $F_{e,h} = L_{e,h} + J_{e,h}$. In the lowest excited state, $F_e = 0 + 1/2 = 1/2$ and $F_h = 3/2$, so the total angular momentum can be either 1 or 2. The states in the $N = 1$ branch are higher in energy than those in

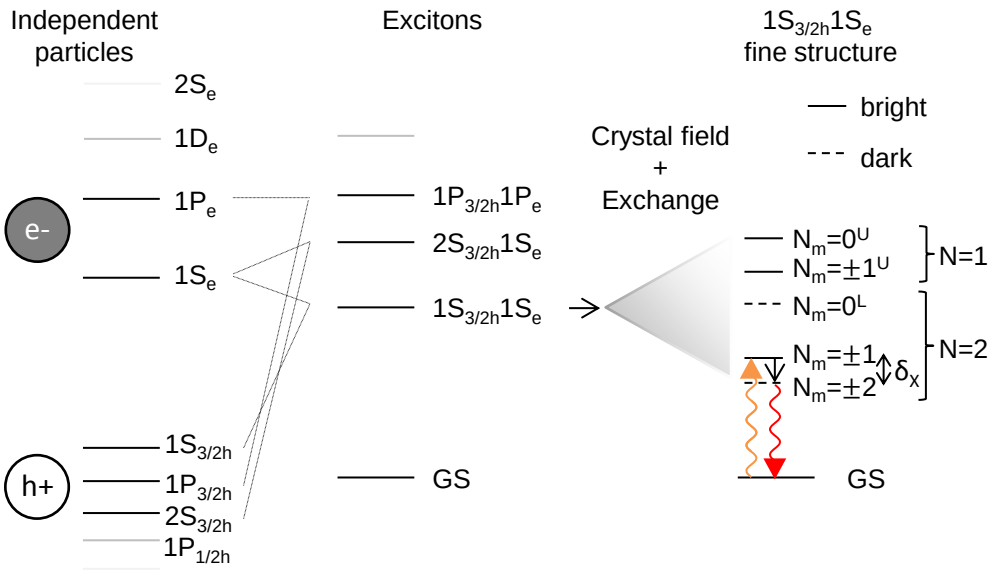

Figure 2.4: Band structure diagram in quantum dots. (Left) Allowed electron and hole states. (Middle) Excitonic states. (Right) Fine structure of the band edge $1S_{3/2h}1S_e$ exciton after accounting for crystal field and exchange effects showing the homogeneous Stark shift δ between the primary optically bright absorptive transitions with $N_m = \pm 1$ and the dark states with $N_m = \pm 2$.

$N = 2$. Reviews of this are provided by Refs. 131 and 242. Efros, *et. al*, showed that the observed Stokes shift between the strongest absorptive state and observed fluorescence $\delta_X = E(N_m = \pm 1^U) - E(N_m = \pm 2)$ is explained by the stronger transition oscillator strength of higher lying states $N_m = \pm 1^U$ state and the lower energy of the $N_m = \pm 2$ dark state.[48]

Excitons thermalize into this low energy state from which dipole transitions to the ground state are optically forbidden in the absence of a phonon. With $N_m = \pm 2$ and $N_m = \pm 1^L$ separated by several meV, thermal population of the $N_m = \pm 1^L$ state become increasingly unlikely at low temperature, leading to radiative lifetimes of order tens of nanoseconds at room temperature and microseconds at low temperatures.[37] Magnetic field-dependent studies of the band-edge exciton at 1.7 K showed that the application of a magnetic field can shorten the PL lifetime, providing evidence for the presence of this optically passive dark state at the band-edge.[175, 48]

2.3 Carrier Relaxation in Optically Excited Quantum Dots

Optically excited charge carriers can relax via a variety of physical mechanisms. Upon photoexcitation, carrier thermalization to a hot, highly energetic distribution occurs on the sub-100 femtosecond timescale.[180] The picosecond timescale for excited-carrier cooling to the band edge[209, 109] typically precludes this except at low temperatures where relaxation progresses more slowly.[84] We refer the reader to several recent reviews that discuss in depth the relaxation processes for hot excitons in quantum dots.[189, 109, 108, 173]

2.3.1 Auger Processes and the Phonon Bottleneck

Historically, the $\sim$100 meV separation between quantized electronic states with different n (i.e. $1P_e$to $1S_e$) was predicted to slow the relaxation of carriers among these levels due to the low probability of a single phonon interaction permitting this relaxation, a phenomenon termed the "phonon bottleneck."[12] In CdSe QDs, the longitudinal optical phonon energy of 26.5 meV was predicted to demand simultaneous emission of multiple phonons for relaxation.[191] Instead, relaxation of hot excitons in CdSe QDs occurs via multiple pathways: Auger processes, phonon relaxation, and interaction with surface ligands. When an electron relaxes via Auger processes, the electron transfers energy to the hole; the hole then quickly relaxes through the more dense manifold of hole states to the band edge via phonon and ligand mechanisms.[47, 79, 109, 189] This subpicosecond process can repeat until the electron has relaxed to the conduction band edge. In addition, the finite size of the nanocrystal and confinement effects on the phonon spectrum may lift degeneracies and generate a spectrum of phonons while also enhancing the electron-phonon coupling, thereby

speeding up the electron decay,[116] although an acoustic phonon bottleneck may still exist for the final stages of relaxation.[53] In the absence of the hole, and thereby the Auger relaxation pathway, the electron relaxation to the band edge can be slowed significantly, increasing from 250 fs to 3 ps.[126] Energy transfer to vibrational modes of ligands has also been implicated as a mechanism for fast relaxation.[81, 189]

2.3.2 Ligand Interactions, Surface States, and Trap States

A recent review by the Weiss group summarized many of the conclusions regarding the impact of ligands on carrier relaxation in QDs.[189] Numerous research groups have devoted significant efforts to understanding the influence of ligands and surface treatments on carrier relaxation, and in Chapter 4 we will discuss the impact of on carrier relaxation of a particular CdSe QD surface treatment.

A schematic depiction of the trapping pathways is shown in Figure 2.5. Electrons are energetically favored to relax to the lowest unoccupied state available, so if the LUMO (lowest unoccupied molecular orbital) of a ligand attached to the surface is at a lower energy than the QD conduction band $1S_e$ state, surface trapping will be favorable. Conversely, because holes relax inversely with electrons, a hole will trap to a surface ligand if the HOMO (highest occupied molecular orbital) of the ligand is at a higher energy. It is important to note that the impact of ligands on hole and electron trapping depends heavily on the composition of the quantum dot, as the energetic positions of the top of the valence band and the bottom of the conduction band differ among materials and shift the energetic balance among orbitals.[243] For example, although the bandgap of CdSe is larger than that of CdTe, both the valence and conduction bands of CdSe are at a more negative potential than CdTe, with more than 0.5 eV separating the CdTe and CdSe valence bands.[243, 83, 99] As a result, ligands orbitals with energy in the intermediate region between the HOMO and

LUMO of CdSe and CdTe may be energetically favorable to trap a hole from CdSe while simultaneously being unfavorable for trapping from CdTe.[243]

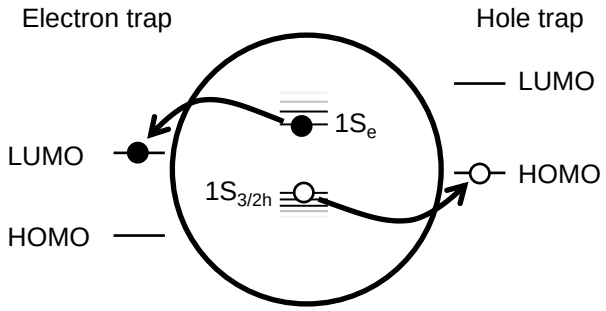

Figure 2.5: Ligand trapping schematic for electrons and holes in quantum dots as described in text.

In the CdSe QD literature, the majority of surface trapping mechanisms associate these surface traps with orbitals that accept holes, basing these claims primarily on density functional theory (DFT) calculations of orbital energies. For example, the Weiss group performed numerous investigations of the impacts of various ligand species such as anilines and phenyldithiocarbamate ligands and found that different ligands can produce either electron and hole traps on the QD surface, attributed via DFT calculations.[132, 58] Buckley, *et al.*, observed that chalcogenol (Se, Te, S) ligands on CdSe QDs cause rapid hole trapping to the surface based on observations of sub-nanosecond quenching of the PL decays.[18] Using infrared transient absorption, tuned to measure intraband populations and relaxation, the Guyot-Sionnest group found that electrons relax more slowly from $1P_e$to $1S_e$ with thiocresol as opposed to trioctyl phosphine oxide (TOPO) and pyridine, and they assign this to the hole traps from Cd-S bonds.[79] Other studies have also reported fast hole trapping in CdSe quantum dots.[93]

On the other hand, fast electron trapping (sub-picosecond to picosecond) has also been reported from CdSe to methylene blue[92] and quinone[19] among others.[58, 19]. Infrared

and visible time-resolved absorption studies showed fast electron transfer to Re-bipyridyl complexes from CdSe quantum dots. Fast electron trapping has been observed CdS QDs in a number of chemical environments.[94]

Experimental claims of fast electron and hole trapping frequently use time-resolved absorption measurements, and in many cases these rely on a particular interpretation of features in these spectra. We will discuss this further in Section 3.1 and Chapter 4, providing evidence that the commonly used measurement of a single transient absorption feature is insufficient to assign dynamics to either electron or hole populations.

Califano and Gómez-Gampos proposed a model of Auger-mediated trapping (AMT) for trapping in semiconductor quantum dots.[71, 20] In this mechanism, the trapped carrier traps to the surface and transfers excess energy to the remaining core carrier. Califano and Gómez-Campos model the QDs atomistically and account for specific bonding character of each surface atom, finding similarity to the range of relaxation timescales found by Knowles, *et al.*[133]

The precise nature of the surface-trapped state has been a topic of vigorous debate. The predominant view is that of a distribution of trap states on the surface of the nanocrystal located between the valence and conduction bands. Decay from these trap states is slow and sometimes radiative at energies below the bandgap. Jones, in the Scholes group, proposed [101, 102] that a simple classical energy transfer model with a single surface state can reproduce many of the conclusions of a trap model. The Kambhampati group proposed a similar model based on Marcus-Jortner semiclassical energy transfer,[103] arguing that such a model can produce the low-energy PL historically associated with deep traps.[162, 161] The key claim of these reports is that this surface state has a non-zero "configuration coordinate" which they identify as QD polarization, and, although it is not significantly lower in absolute energy, it is separated by an energetic barrier to trapping. This energy barrier is said to produce signatures in the temperature dependence of bandedge PL and

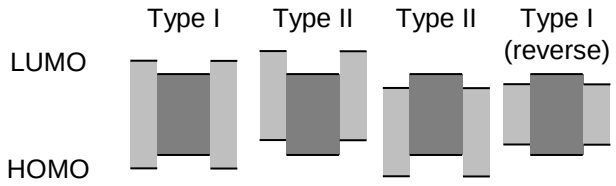

Figure 2.6: Core-shell quantum dot energy schematic. Cores represented by dark grey, shells by light grey. Relative height and position of top (bottom) of boxes represents bandgap and conduction band (valence band) of core or shell.

surface PL, and surface emission (sub-bandgap emission) occurs via coupling to the ground state at this non-zero configuration coordinate. Because the core ground state is centered at zero configuration coordinate of the QD and the energy of the core state increases with configuration coordinate, PL emitted from the surface state will be at energies smaller than the zero-coordinate bandgap. Mooney, *et. al*, find further evidence for this model in their temperature dependent studies of CdSe QD PL.[163]

2.3.3 Core-Shell Structures

Core-shell quantum dots are those in which a core of one semiconductor material is surrounded by another semiconductor.[196, 230, 23] In these conditions, the absolute positions of the valence and conduction bands in the core versus the shell differ, producing different energetic incentives for carrier localization in each medium (Figure 2.6).[196] In a type I configuration, the bandgap of the shell is greater than the core, confining both electron and hole to the core. In type II configurations, the valence or conduction band of the shell lies within the bandgap of the core and carriers will become spatially separated due to carrier relaxation. Reverse type-I band alignments have a shell of smaller bandgap material, causing partial or complete confinement of both carriers to the shell.

Hines and Guyot-Sionnest reported the first instance of core-shell nanoparticles and found that this shell coating both passivated the surface of the core and increased the band-edge fluorescence quantum yield to 50%.[88] Core-shell quantum dots have recently seen significant improvements with applications in lighting,[23] and CdSe-CdS core-shell nanocrystals can be synthesized with a narrow size distribution (4%), low fluorescence intermittency (blinking), and 97% quantum yield.[24]

Controlled engineering of the confingement using the band offset between core and shell conduction and valence bands can drastically modify the decay kinetics and relaxation pathways in a nanocrystal, in some cases leading to charge separated states or optical gain as we further discuss in Section 2.3.4.[170, 183, 115, 254, 40, 238]

2.3.4 Biexcitons and Multiexcitons

The presence of multiple excitons in a single quantum dot can change the energetic landscape and decay kinetics significantly. The absorption spectrum from a single exciton state to a biexciton state differs from ground to exciton and similarly from a biexciton to a higher order multiexciton. The spectrum depends on the interaction among the excitons and the degeneracy of the states; for example, the twofold degenerate $1S_e$ conduction band in CdSe means that two relaxed excitons will completely block further transitions into any states involving this lowest-energy electron state.

As discussed earlier in Section 2.2, the Stokes shift $\delta_X = E(X_{Abs}) - E(X_{PL})$ between absorptive and emissive transitions can be understood in the context of the fine structure of the excitonic state. The presence of an exciton in the QD modifies the Stokes shift between further absorptive and emissive transitions to $\delta_{XX} = E(XX_{Abs}) - E(XX_{PL})$. The biexciton binding energy then is $\Delta_{PL} = E(X_{PL}) - E(XX_{PL})$. Additional transition shifts are likely in the presence of multiexcitons.[208]

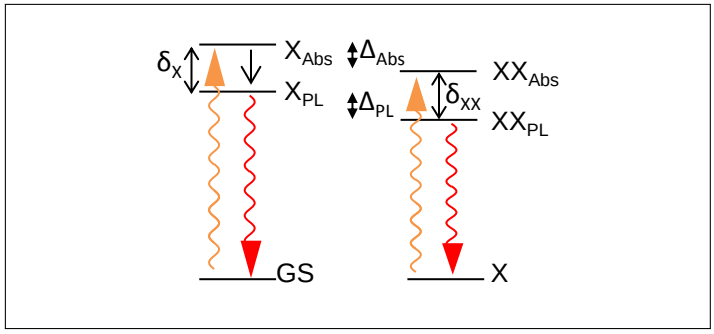

Figure 2.7: Schematic showing the energetic shifts of biexcitons.

Auger processes can cause multiexciton configurations to rapidly decay on the time scale of tens of picoseconds, becoming faster with decreasing QD size.[129] Radial changes in nanocrystal composition such as core-shell structures (discussed in Section 2.3.3) can also lead to the observation of optical gain enabled by modification of relaxation pathways due to selective changes to the wavefunctions of electrons and holes.[127, 34, 40, 64]. For example, "giant" core-shell quantum dots can decrease the availability of Auger decay pathways, allowing multiple excitons to survive on a nanosecond timescale.[64] The strength of these Auger processes has been shown to depend heavily on spatial separation of carriers and the presence of abrupt confining potentials that break symmetry in quantum dots, such that shells and graded confinement potentials suppress the Auger processes.[170, 238].

2.3.5 Interactions and Environment

Beyond the impact of the ligands attached to an individual quantum dot, the local environment also plays a large role in transport and carrier relaxation. For example, the local dielectric environment can modify the energetic position of the band-edge absorption,[140] and as described below energy transfer and charge separation are possible in the presence of other quantum dots and materials.

By comparing the PL yield of large and small (6.2 nm and 3.85 nm diameter, respec-

tively) QDs dispersed in solution to close-packed QD solids, Kagan demonstrated that, when close-packed, smaller, higher-energy QDs transfer energy to the larger acceptor QDs via Förster resonance transfer. [105, 104] Energy transfer among nanocrystals with a distribution of sizes was also shown in drop-cast films and Langmuir-Blodgett assemblies using time-resolved photoluminescence measurements; these studies demonstrate shorter lifetimes for smaller nanocrystals.[36, 3] Studies of energy transfer and exciton diffusion in quantum dots by the Tisdale group found that increased ligand length and shell thicknesses decreases the exciton diffusion length and that excitons can become trapped at local minima in the energy landscape at low temperatures.[4, 190] Increasing the separation of layers of single component films can decrease energy transfer between those films.[31, 150, 117] Increasing the QD spatial density in films also increases the diffusion of excitons, decreasing the fluorescence lifetime of the higher energy fluorescence while increasing the lifetime of the lower energy fluorescence as excitons diffuse to lower energy sites.[151]

Studying films and dispersions with different capping ligands, Gao, *et al.*, showed that increased coupling in films as compared to colloidal dispersions enhances the carrier cooling rate.[62] Additionally, energetic disorder in the QD band-edge states from QD to QD was also shown to play a larger role than expected in quantum dot solids as charge carriers aggregated on the lower energy "hotspots" and decayed via Auger interactions in highly coupled quantum dot solids even at exciton fluences much less than one exciton per QD.[63]

Similarly, in films composed of both CdSe and CdTe quantum dots, an energetic incentive exists for electron transfer from CdSe to CdTe due to the band offsets of the conduction and valence bands in spite of the larger bandgap in CdTe.[15] Charge transfer can also occur from QDs to TiO_2 films and nanoparticles, even on ultrafast (femtosecond to picosecond) timescales.[197, 198, 225] We will further discuss recent advances in interparticle coupling in Chapter 6 and Chapter 7, as recent advances have led to applications

in numerous types of quantum dot electronic devices.

2.4 Conclusions

Quantum dots provide a rich and complex playground to understand the interplay of confinement with surface chemistry, energy transfer, and charge carrier relaxation dynamics. Approaching these systems as an experimentalist, it is clear that optical and electronic experimental methods will both be extremely valuable in understanding charge carrier dynamics and interactions in these nanoscale semiconductor materials.

Chapter 3

Optical Apparatus: Time-Integrated and Time-Resolved Photoluminescence and Absorption

3.1 Introduction

As discussed in Chapter 2, carrier relaxation in quantum dots and interactions between core and surface processes involves timescales ranging from sub-picosecond to picosecond (hot carrier relaxation, hot exciton photoluminescence, electron-hole separation, surface and ligand trapping, bright state band-edge photoluminescence) and nanosecond-microsecond timescales (emission from the dark exciton). [37] Optical spectroscopies are extremely valuable for probing both the linear, time-integrated response of the systems to light and the temporally evolving dynamics at short time scales. We detail in this Chapter a visible range

optical apparatus to observe time-resolved and time-integrated photoluminescence and optical absorption in order to investigate these various interactions and relaxation processes in nanocrystal films (Chapter 4) and plasmonically coated nanowires (Chapter 5). We will discuss the motivation, design considerations, construction, and optimization of this apparatus, starting with an introduction to the information obtainable with these techniques in this Section, describing different candidate TRPL techniques in Section 3.2, focusing on the time-resolved photoluminescence (TRPL) apparatus in Section 3.3, continuing with the time-resolved absorption (TRA) configuration in Section 3.4, and finishing with a brief description of some experimental hurdles and optimizations involved in these experiments in Section 3.5.

Time-integrated fluorescence is a widely used and straightforward technique to investigate the electronic structure of quantum dots. In the absence of time-resolved measurements, direct assignment of relaxation rates and decay pathways is significantly more tenuous. However, observation of photoluminescence at a particular energy reveals the presence of an optically active electronic transition at that energy and the involvement of the constituent initial and final states in the decay pathways of the quantum dot. In principle it may also be possible to observe emission as carriers relax to the band-edge, but the dominance of non-radiative relaxation pathways to the band edge make observing intraband emission challenging and hot-exciton emission is typically a small factor, as we discuss in Chapter 5. Time-integrated photoluminescence measurements thereby primarily inform the experimentalist of the final radiative pathways followed by carriers in their trajectory to the ground state from optically active excitonic states, and time-resolved photoluminescence indicate the time-dependent population and lifetime of optically bright emissive states in a system, decaying as that population decreases either radiatively or nonradiatively.

Similarly, linear optical absorption also provides the experimentalist a wealth of information on the available optical transitions in a sample in the ground state. However, in

systems where the presence of an excitation modifies the available states for an additional excitation, time-resolved absorption measurements allow a window into the relaxation dynamics of individual carriers as they pass through the electronic states of the system.

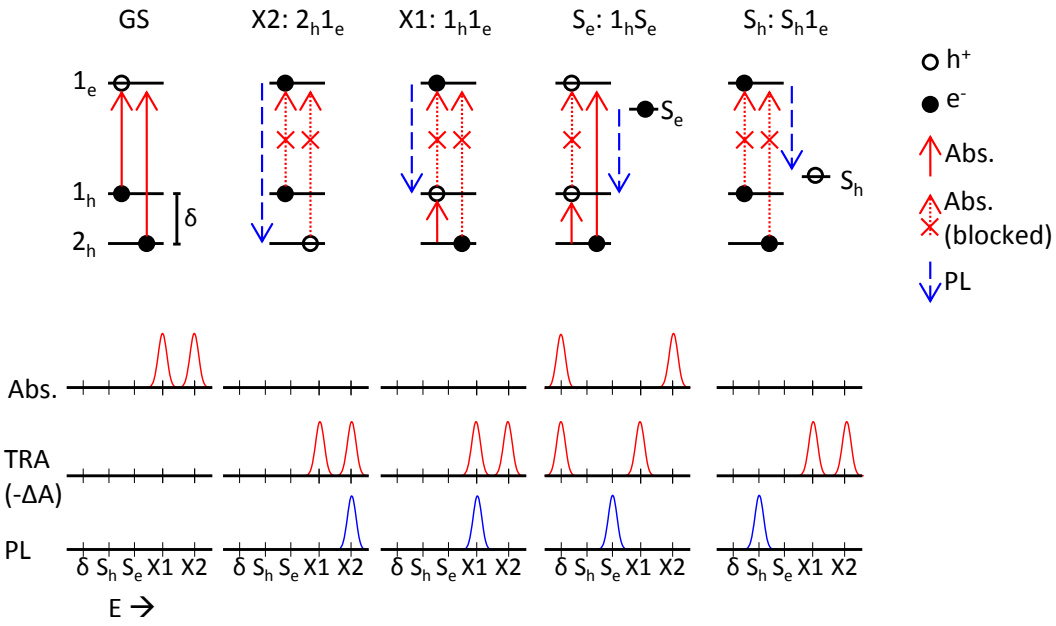

Figure 3.1: Schematic example of absorption, time-resolved absorption, and photoluminescence signal interpretations. Solid circles represent electrons, hollow circles holes. Available absorptive transitions are marked with solid red arrows; blocked absorptive transitions marked with dotted red arrows with $\times$ marks. Photoluminescence signals marked with dashed blue arrows. States are marked at the top of each column.

Pump-probe time-resolved absorption measurements fill that gap by observing the pump-induced changes in the absorption spectra of a sample. We show an example of the types of signals and associated energetic positions that can arise in absorption and photoluminescence spectroscopy in Figure 3.1. In this example, we ignore spin degeneracy and consider each state to have a maximum occupation of one carrier. In the ground state (GS), absorptive optical transitions, labeled with solid red arrows, are allowed from the

electron-occupied valence band states 1_h and 2_h to the unoccupied conduction band state 1_e, with energies labeled X1 and X2, respectively. After excitation into X1 or X2, the presence of the electron in 1_e blocks further transitions from 1_h or 2_h, producing a decrease in the absorption (negative ΔA) at the energies of X1 and X2. Although populations of both X1 and X2 bleach the X1 and X2 transitions identically, the presence of a hole in 1_h (due to X1 or S_e) induces an absorptive transition at energy $\delta = E(X2) - E(X1)$. If X1 and X2 are close in energy, this transition may be difficult to resolve, but X1 and X2 are directly distinguishable with photoluminescence spectroscopy where PL is emitted at characteristic energies. Depending on the fine structure within X1 and X2, it may also be possible to observe stimulated emission.

The use of TRA and TRPL measurements in concert can thereby help to tease out the populations of optically active and inactive electron and hole states. Considering a generalized surface state that accepts electrons (S_e) or holes (S_h), the TRA signals of each would differ because of the shared 1_e state of X1 and X2, as shown in Figure 3.1.

The magnitude of TRA bleach signals depends heavily on the degeneracies of the different states. Increased degeneracy in a given state will decrease the impact on TRA of carrier occupation in that state: for example, if instead of single degeneracy the 1_h state had many-fold degeneracy, the presence of a hole (S_e state) might only negligibly bleach the X1 transition thereby decreasing the TRA signal at X1 to make the sample appear similar to the ground state.

By combining time-resolved photoluminescence and time-resolved absorption, we may be able to disentangle the relative contributions from occupation of individual hole and electron states in our systems.

3.2 Time-Resolved Photoluminescence Techniques

Numerous methods exist for measuring the temporal dependence of photoluminescence from samples. A brief description of some of these methods is provided in the following sections, and a summary of some typical key parameters is provided in Table 3.1. We will first compare these methods and then elaborate on the construction of the optical Kerr gate (OKG). As discussed in Section 3.2.5, the OKG provides broadband, time-resolved observation of optically emissive processes on the sub-picosecond to nanosecond time scales. Furthermore, the OKG permits time-resolved two-dimensional imaging when sample emission is spectrally integrated and detectors are configured appropriately. Although many experimental challenges must be overcome to optimize the OKG, its time resolution, spectral width, and configurability are well matched to the samples we investigate in Chapters 4 and 5.

3.2.1 Streak Camera

Streak cameras provide broadband fluorescence maps and have been previously used in TRPL measurements of quantum dots.[157, 164, 156, 195, 84, 165] Incident photons to the detector are converted to electrons; these electrons are accelerated through a mesh and pass through "sweep electrode." This sweep electrode applies a time-varying potential to deflect electrons prior to arrival at the multi-channel plate (MCP) that amplifies the electron current. The final charges on the detector are proportional to TRPL signal, and the temporal profile is encoded in the displacement of the charges. The time resolution is therefore dependent on the sweep rate, which can be adjusted, and the jitter in reproducibly sweeping at the same time. Streak cameras are capable of very high time resolution in the single-shot mode, but jitter in the relative timing of electronic control and signalling reduces this resolution when multiple shots are combined.

Method	Resolution (typ.)	Advantages	Disadvantages	Representative Refs.
TCSPC	30 ps	Commercially available, single photon sensitivity	Electronics limited time resolution, single spectral bin	[102, 133]
Streak camera	35 ps	Commercially available, direct time & spectral readout	Electronics limited (jitter)	[157, 164, 84]
Upconversion	250 fs	Time resolution	Challenging alignment, limited spectral range	[115]
Intensifying CCD	80-200 ps	2D imaging, broadband spectra, commercially available	Electronics limited (jitter)	[218]
Kerr gate	250fs	Time resolution, 2D imaging, broadband spectra	Background from gate medium & long integration times	[220, 9]

Table 3.1: Time-resolved photoluminescence measurement techniques. Performance characteristics as listed are "typical" rather than "best."

3.2.2 Time-Correlated Single Photon Counting

Time-correlated single photon counting (TCSPC) is a staple technique for measuring lifetimes on picosecond to nanosecond time scales in QD systems.[18, 154, 102, 133, 10, 36] TCSPC systems are commercially available and have time-resolutions as low as 25 ps. TCSPC systems measure the relative timing of a pump pulse detected by a trigger diode and resultant photons emitted from the sample; the resolution is determined by the precision of this delay detection. However, a "dead time" interval occurs after detection of a single

photon wherein no additional signals can be measured, so care must be taken to acquire signals at sufficiently low excitation so all photons are counted properly. TCSPC systems frequently use photomultiplier tubes or avalanche photodiodes as detectors. The time-resolved decay signal is determined by creating a histrogram from many such detection events. Spectrally resolved decay maps can be acquired by sweeping over wavelengths with a spectrometer.

3.2.3 Intensifying CCD

In an intensifying CCD (ICCD), photons first impinge upon a photocathode which releases electrons upon contact. These electrons are accelerated to a multi-channel plate (MCP) which amplifies the current. The time resolution of an ICCD is determined by the time to enable and disable the gate between photocathode and MCP and the time, if relevant, to enable/disable the amplification in the MCP. ICCDs have been used to measure fluorescence decays of tryptophan,[218] have resolutions as low as 25 ps, and are commercially available from multiple vendors.

3.2.4 Fluorescence Upconversion

Fluorescence upconversion is an application of sum-frequency mixing using a non-linear crystal to measure the femtosecond and picosecond fluorescence dynamics of a sample.[106] A very good review of this technique was provided by J. Shah.[212] This technique has been applied to QD to measure ultrafast fluorescence transients at short times, particularly by the Klimov and Rosenthal groups.[115, 16, 67, 66, 122, 229, 157, 133, 123, 125, 245, 2] The bandwidth of this upconverted signal depends on the nonlinear crystal and the geometric configuration of the experiment.[54, p. 84]

Sum-frequency generation can occur in materials with a strong 2nd order non-linear

susceptibility. In these materials, when certain phase-matching conditions are met for the propagation of two beams of light with frequencies ω_1 and ω_2, the 2nd order susceptibility can lead to the generation of light at frequency ω_3 where

$$\omega_3 = \omega_1 + \omega_2 \tag{3.1}$$

The other constraint is that for generation to occur throughout the nonlinear medium, the wavevectors for each beam must also obey

$$\vec{k_1} + \vec{k_2} = \vec{k_3} \tag{3.2}$$

where $|\vec{k_i}| = \frac{n_i}{\lambda_i}$ with $i = 1,2,3$, n is the index of refraction along the direction of propagation, and $\lambda = 2\pi c/\omega$ is the wavelength of the light in vacuum. In a collinear setup where all beams are propagating in the same direction this leads to

$$\frac{n_1}{\lambda_1} + \frac{n_2}{\lambda_2} = \frac{n_3}{\lambda_3}. \tag{3.3}$$

Although these constraints are trivially satisfied in vacuum, in general the wavelength-dependent index of refraction in a material prevents this phase matching condition. However, in an anisotropic crystal, the index of refraction n depends on the direction of propagation and polarization; in a uniaxial crystal where n is identical for two directions, the two indices of refraction are labeled n_o for the "ordinary" (identical in two directions) and n_e for the "extraordinary" indices of refraction. In this case, the phase matching condition is met for

$$\frac{1}{n_i^2} = \frac{\sin^2\theta}{n_{e,i}^2} + \frac{\cos^2\theta}{n_{o,i}^2}. \tag{3.4}$$

In general, sum-frequency generation processes like that used in fluorescence upconver-

sion must involve at least one extraordinary ray to satisfy the phase matching condition. The efficiency of the upconversion process decreases quickly as the fluorescence wavelength moves away from the central phase-matched wavelength and the phase-matching condition is no longer well satisfied. The time resolution of this process is determined by the group velocity mismatch between the pump and fluorescence beams, as a greater mismatch will cause different slices in time to overlap at different sections of the crystal.

The principal disadvantages to fluorescence upconversion in detecting time-resolved photoluminescence signals are the low efficiency of the upconversion process and the bandwidth limitations imposed by the phase matching conditions. The upconversion process also means that signals must be detected at a separate wavelength than at emission.

3.2.5 Optical Kerr Gate

The optical Kerr gate[42][54, pp. 82-86] is effectively a broadband optical shutter produced by a transient birefringence induced in a medium placed between two crossed polarizers; its time resolution is limited only by the nonlinear response of the Kerr medium and the pulse duration of the gating laser. We will now discuss the theory underpinning its operation.

Considering a monochromatic, coherent beam of light travelling in the z direction incident on a linear polarizer, we will have a vertically polarized electric field E_i given by

$$\vec{E_i} = E_0 \hat{y} \exp i(kz - \omega t) \tag{3.5}$$

for the wave after the first polarizer. Now consider the impact of a birefringent optic at $z = 0$ with an optical axis at an angle θ from the $\hat{y}$ direction and a thickness L. The ordinary and extraordinary indices of refraction for light polarized along the optical axis $\hat{e}$ and perpendicular to it are given by n_e and n_o, respectively. In terms of θ, the coordinate system

in terms of the laboratory frame axis is given by

$$\hat{e} = \sin\theta\hat{x} + \cos\theta\hat{y} \tag{3.6}$$

$$\hat{o} = \cos\theta\hat{x} - \sin\theta\hat{y}. \tag{3.7}$$

Therefore, we can project the incident electric field $\vec{E}_i$ onto these coordinates as

$$\vec{E} = \hat{e}\cos\theta\exp(k_e z - \omega t) - \hat{o}sin\theta\exp(k_o z - \omega t) \tag{3.8}$$

The principal effect of the birefringent optic is the difference in index of refraction along $\hat{e}$ and $\hat{o}$. The phase shift in the two components induced by this difference is determined by $k_{o,e} = \frac{2\pi n_{o,e}}{\lambda}$. Therefore, the phase shift $\phi_{o,e}$ in the two components of $\vec{E}$ at the end of the optic at $z = L$ is given by

$$\phi_{o,e} = k_{o,e}z = \frac{2\pi n_{o,e}}{\lambda} = \frac{2\pi n_{o,e}L}{\lambda}. \tag{3.9}$$

and therefore

$$\vec{E} = \hat{e}\cos\theta\exp(\phi_e - \omega t) - \hat{o}sin\theta\exp\phi_o - \omega t \tag{3.10}$$

Now we consider the impact of a second polarizer, crossed to the first to pass horizontally polarized light, at some position $z = d$ later. This polarizer will only pass electric fields

polarized along the $\hat{x}$ direction, so we need only consider the projection along the $\hat{x}$ axis.

$$E_x = E_e \sin\theta - E_o \cos\theta \tag{3.11}$$

$$= \sin\theta\cos\theta(\exp(i\phi_e) - \exp(i\phi_o)) \tag{3.12}$$

$$|E_x|^2 = \sin^2\theta\cos^2\theta(2 - \exp(i(\phi_e - \phi_o)) - \exp(i(\phi_o - \phi_e))) \tag{3.13}$$

$$|E_x|^2 = 2\sin^2\theta\cos^2\theta(1 - \cos(\underbrace{\phi_e - \phi_o}_{\Delta\phi})) \tag{3.14}$$

$$|E_x|^2 = \sin 2\theta \sin^2\left(\frac{\Delta\phi}{2}\right) \tag{3.15}$$

The transmission through the second polarizer is clearly maximized when the optic axis is at $\theta = 45^\circ$, so the transmission will scale as $T = \sin^2(\Delta\phi/2)$ under this condition. We now consider $\Delta\phi = \frac{2\pi L\Delta n}{\lambda}$ with $\Delta n \equiv n_e - n_o$. In an isotropic medium, all axes of the medium have identical n, and Δn is zero except under the effect of an outside force. However, in certain materials a strong applied electric field can induce large changes in the index of refraction along the axis of the applied field. In this case, the induced change in birefringence along an axis scales as

$$\Delta n = \gamma I \tag{3.16}$$

where γ is the nonlinear refractive index of the material, I is the intensity of the beam. Pulling this all together for a time-varying $I(t)$, we find that the transmission for an optimally oriented gate beam with polarization oriented at $45^\circ$from vertical, the overall transmission of such a system scales as

$$T(t) = \sin^2\left(\frac{\pi L\gamma I(t)}{\lambda}\right). \tag{3.17}$$

The efficiency of the OKG therefore depends on the wavelength to be investigated and the nonlinear coefficient of the Kerr medium. This nonlinear coefficient index arises from

both electronic and molecular mechanisms,[89] and the impact and choice of Kerr mediums will be discussed in Section 3.3.4.

3.3 Time-Resolved Photoluminescence Apparatus

Several good reviews of the construction of an optical Kerr gate are provided by Good reviews by Takeda, *et al.*, and Arzhantsev and Maroncelli.[220, 9] Gundlach and Piotrwiak also used an optical Kerr gate for sub-picosecond fluorescence measurements at room temperature in a configuration that used reflective Cassegraine objectives instead of the 150 mm effective focal length off-axis parabolic mirrors used here.[77] A schematic diagram of our experimental apparatus is shown in Figure 3.2. The 1 kHz, 800 nm, 120 fs output is frequency doubled in a BBO crystal to generate the 400 nm pump beam for PL, TRPL, TRA measurements. The 800 nm gate beam is used to generate a transient birefringence in the Kerr medium between the two sets of crossed polarizers, P1 and P2; P3 and P4. All spectra are acquired with a 0.55 m spectrometer (Jobin-Yvon Triax 552) and a thermoelectrically cooled CCD (Spec-10, Princeton Instruments).

The spatial extent of the gated fluorescence region of the sample is limited by the power that can be safely captured or deflected prior to reaching the second set of polarizers. An off-axis gating geometry permits capture of greater spatial extent of fluorescence from the sample because we can capture the gate beam after it has expanded (Figure 3.2). The gate beam is focused using a 500 mm focal length lens, coming to focus approximately 40 mm after passing through the Kerr medium. The time resolution of this configuration as used in the experiments of Chapter 4 was 500 fs. At focus, a 500 mW beam is intense enough to ionize the air through which it passes and generates a dim, white streak of emission in mid-air. As mentioned in Section 4.4, this focused beam is intense enough to ablate fused silica brass, aluminum, and anodized aluminum. The gate beam is captured by a razor

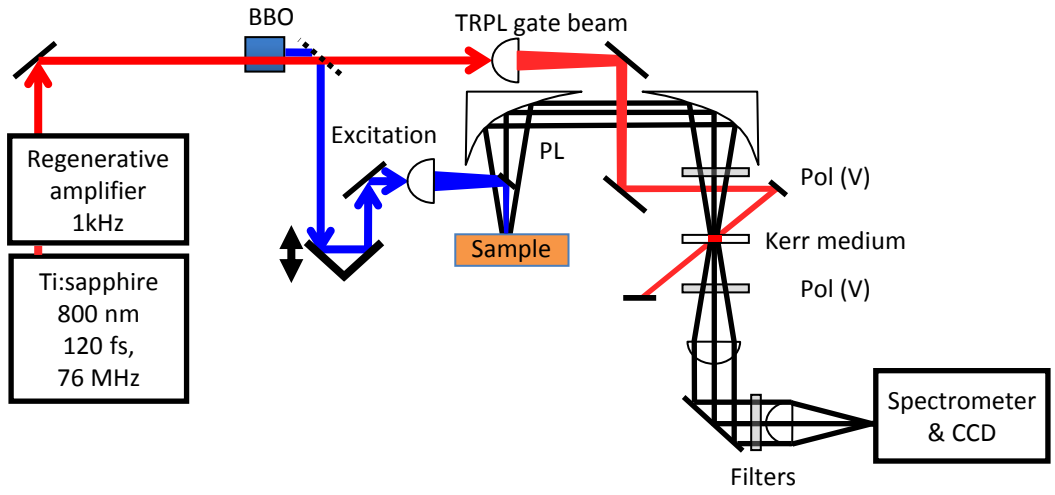

Figure 3.2: Schematic of off-axis time-resolved photoluminescence apparatus. Polarizers are co-polarized (V,V) for DC PL measurements and cross-polarized (V, H) for TRPL. Dotted lines show dichroic optics; dashed lines show broadband splitters.

stack beam stop approximately 190 mm after focus after it has expanded to a diameter that does not damage the beamstop. For the CdSe QD experiments described in Chapter 4, we use this focused beam to precisely score sample substrates to cleave to the desired size for mounting in the Microstat.

3.3.1 Optical Layouts

For the experiment described in Chapter 5 we used the on-axis gating configuration as shown in Figure 3.3. The instrumental response time in this configuration was shorter, 240 fs, but the gated region of the fluorescence was smaller to match the small size of the region of interest of the sample.

The relative delay of the 800 nm gate beam and 400 nm pump beam is controlled by a stepper motor (Shimano Kenshi SST42D1040) driven mechanical delay line with

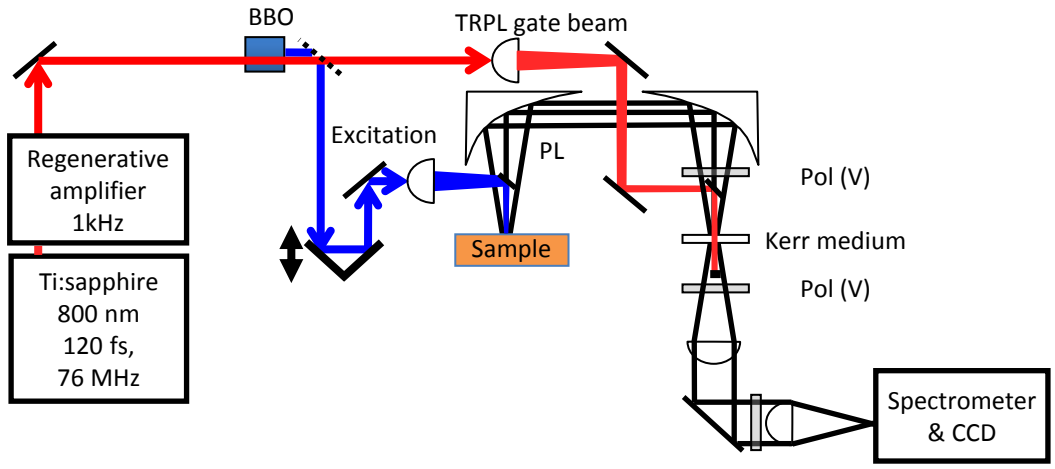

Figure 3.3: Schematic of on-axis time-resolved photoluminescence apparatus. Polarizers are co-polarized (V,V) for DC PL measurements and cross-polarized (V, H) for TRPL / Kerr gate measurements. Dotted lines show dichroic optics; dashed lines show broadband splitters.

a retroreflector (PLX, Inc.) with 23 fs step size. Beams are controllably blocked during experiments by black cards brought into and out of the beam paths using stepper motors.

In all TRPL experiments, the pump and excitation beams are blocked using dielectric filters after the analyzer polarizer. The pump beam is blocked using Newport 20-CGA420 long pass filters, and scattered gate light is blocked using an Edmund Optics NT64-332 750 nm short wave pass filter at the entrance to the spectrometer.

Typical instrument response times for the TRPL experiments in the on- and off-axis configurations are approximately 240 fs and 500 fs, respectively. Resolution as configured is 11 nm for absorption measurements and 15 nm for PL measurements. Time-integrated polarized PL measurements on drop cast samples are made by co-polarizing the polarizer pair around the Kerr medium.

3.3.2 Polarizer Selection and Placement

In our configuration we use four Moxtek PFU-04C wire-grid polarizers. These polarizers are mounted in custom-designed holders mounted on rotary mounts from Opto-Sigma (part number 114-0220). Polarizer P1 is mounted in a non-rotating manner, while P2, P3, and P4 are able to rotate independently. Mounting P1 stationary reduces the profile of the polarizer mount. The markings on these mounts permit reproducible rotation to 5'. The polarizers have lithographically printed wires on one side of the substrate, and for protection of these surfaces we mounted (P1 and P2) and (P3 and P4) on combined mounts with the wires on the inner faces. Although these polarizers have a wide acceptance angle and high contrast ratio (5,000:1 for one pair), the off-axis parabolic mirrors require careful consideration of polarizer placement.

We tested various configurations in order to determine peak performance of the polarizers and the constraints possible in the OKG geometry where PL must be telescoped onto the Kerr medium. These configurations are shown schematically in Figure 3.4 and the resulting extinction ratios are shown in Table 3.2. All configurations use two pairs of polarizers; the first pair is configured to pass only vertically polarized light and the second passes horizontally polarized light.

3.3.3 Substrate Selection

Numerous substrate materials were tested to minimize the undesired background fluorescence as shown in Figure 3.5. Ultraviolet (UV) grade fused silica (Suprasil 2 from Meller Optics, Nikon VUV from Volume Precision Glass, Corning High Purity Fused Silica (HPFS) 7980 from Edmund Optics), was found to have low background fluorescence. We use the readily available 0.5 mm thick Corning HPFS 7980 substrates from MTI Corporation (not shown here).

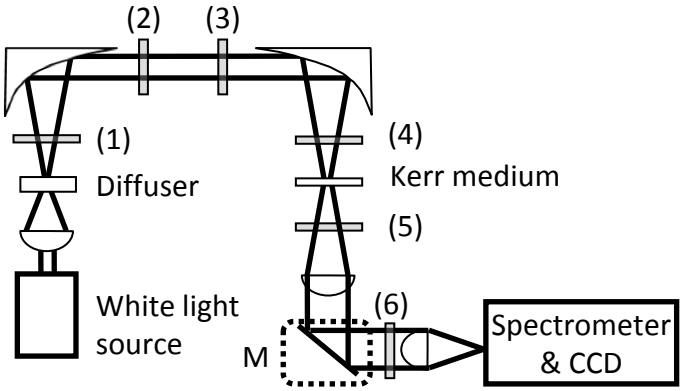

Figure 3.4: Schematic of polarizer locations for extinction measurements.

P1, P2 Loc.	P3, P4 Loc.	Extinction Ratio	Comment
2	5	(not measured)	Vertical region of extinguished region varies with polarizer angle. Visible to naked eye.
2	6	300	OPM at position marked "M." Spherical aberrations present, only a small region is at focus on CCD. Visible to naked eye.
1	5	4000	
4	5	40000	Fused silica Kerr medium in place
4	5	80000	Configuration used for TRPL
2	3	250000	Beam propagates colinear with the polarizer axis

Table 3.2: Polarizer extinction ratios in varied experimental geometries. Polarizers P1 and P2 (vertically polarized) located at position as marked in Location 1 and Polarizers P3 and P4 (horizontal) at position as marked in Location 2 of Figure 3.4

3.3.4 Kerr Medium Selection and Mounting

The design of an optical Kerr gate depends strongly on the choice of Kerr medium, the temporal resolution desired for the experiment, and the absolute intensity of emission

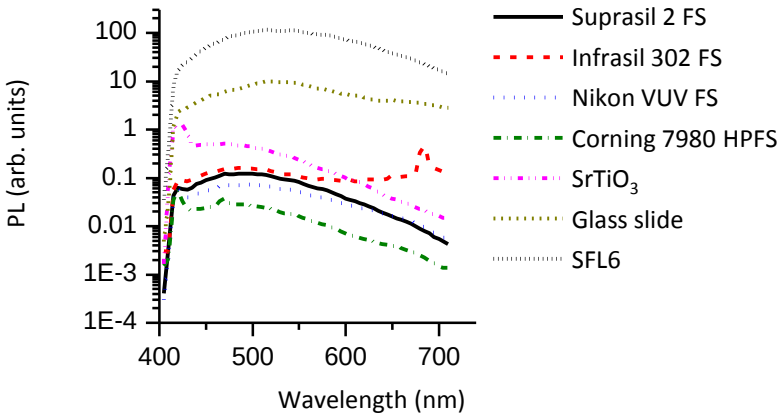

Figure 3.5: Fluorescence from candidate sample substrates excited at 400 nm.

from the samples under investigation. Kerr electronic polarizability is the cause of the large nonlinear index in glasses and may contribute to the fast response in some liquids. Molecular reorientation is the cause of large nonlinear index in liquids such as CS_2.[54, p. 83][89]

A key detractor from the optical Kerr gate is background fluorescence produced by the gate beam in the Kerr medium. Because this fluorescence occurs in between the two polarizers, it is not possible to use polarization optics to selectively cancel it; any such action will directly increase the background signal from the sample that passes through the analyzer.

Time-resolved photoluminescence measurements with an optical Kerr gate will have signal contributions (N_{total}) from several sources:

$$I_{total} = I_{gated} + I_{KB} + I_{leakage} \tag{3.18}$$

where I_{gated} is the desired gated signal, I_{KB} is any undesired background signal produced by the gate beam inside of the Kerr medium, and $I_{leakage}$ is the signal produced at the sample at any time that passes through the medium when the gate beam is not enabled.

Material	Contrast ratio	Geometry	Comment
UV grade Fused silica	35000	Amorphous, 0.76mm	
GGG	11000	(111) polished	MTI Corp.
YAG	18000	(100) polished	MTI Corp.
$SrTiO_3$	210	(unk.) polished	
SFL2	17000	Amorphous	VPG
SFL5	17000	Amorphous	VPG
SFL7	15000	Amorphous	VPG

Table 3.3: Polarization contrast ratio for various Kerr media materials.

The experimental signal to background ratio is therefore a tradeoff between these three parameters as we will discuss below.

Numerous optical glasses and crystals have been considered in the search for the ideal Kerr medium. Nakamura, *et al.*, studied a series of 16 glasses and 3 crystals and found that $SrTiO_3$ was a promising candidate for its ratio of non-linear susceptibility to background fluorescence.[169] Yu, *et al.*, suggest yttrium aluminum garnet (YAG, $Y_3Al_5O_{12}$) and galodinium gallium garnet (GGG, $Gd_3Ga_5O_{12}$.[251] We tested the polarization contrast ratio of these and other media as described in Table 3.3 and found that the polarization contrast ratio was nearly twice as good in UV grade fused silica as compared to other candidate Kerr media materials.

In choosing a Kerr medium, one must also contend with undesired background photoluminescence generated by the gate beam. We found, in agreement with Takeda, *et al.*,[220] that fused silica also provided an optimal balance of gating efficiency with our 800 nm, 120 fs, 0.5 mJ pulses compared to the photoluminescence from the fused silica Kerr medium. All other materials we tested ($SrTiO_3$, YAG, GGG, SFL 2, SFL 5, SFL 6,

SFL 57) had either a substantially worse ratio of greater background photoluminescence to gated signal or significantly worse polarization contrast ratios, which would produce much greater leakage signal. Comparisons of background fluorescence from the Kerr medium to gated signal are shown in Figure 3.6. The Suprasil 2 substrate (fused silica) clearly produces far less background fluorescence than other media tested (Figure 3.6a and Figure 3.7a). Although fused silica gates the signal less efficiently than some other media tested (SFL 57, SFL2, SFL6, GGG), the ratio of gated PL to background fluorescence is more than 10 times better (Figure 3.7). The differences between these results and those of Yu, Gundlach, and Piotrowiak [251] may be due to the small magnitude of the fluorescence signal we measure as opposed to the beam of an optical parametric amplifier they use as a probe beam which may dwarf the Kerr medium background fluorescence.

We stress that this low fluorescence is necessary in order to measure the very low signals necessary for our experiments. In the case of our least emissive samples, with the Kerr gate's efficiency of 10 % we are measuring only 20 background-subtracted counts in a 120 s exposure with 0.5 W power operating the Kerr gate, so the gate background fluorescence must be extremely low. We discuss background subtraction methods further in Section 3.3.6 and note that fluorescence peaks develop in the fused silica emission at approximately 650 nm after long exposures to the 800 nm gate beam at high intensity as seen previously.[22, 172] Future effort on this experiment will further investigate additional Kerr media, including new formulas of high purity fused silica and liquid Kerr media such as benzene and carbon disulfide.[9, 158, 95] Additionally, further experimental efforts may permit the use of an optical parametric amplifier to gate at longer wavelengths and thereby extend the detection range of this apparatus.[206]

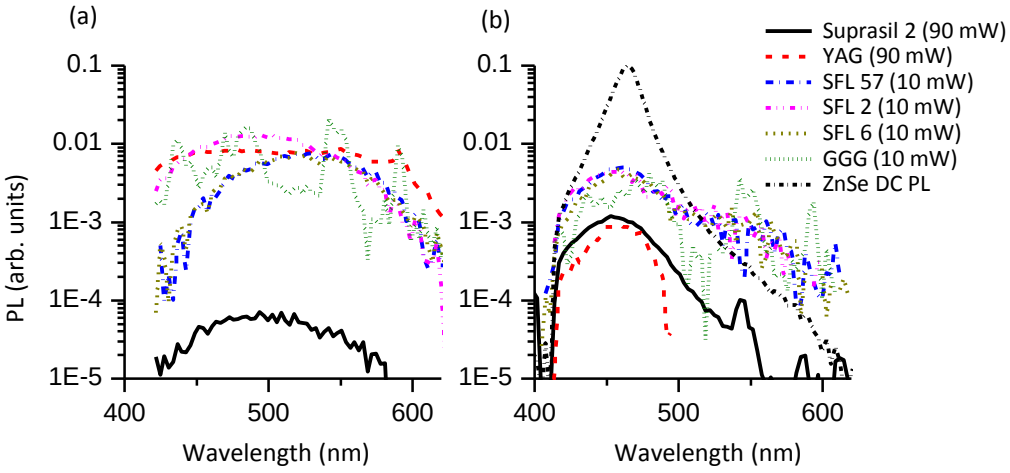

Figure 3.6: (a) Fluorescence background from Kerr media, scaled for laser power, gated with 800 nm gate beam with powers as specified in the legend. (b) Gated PL signal from ZnSe thin film, scaled for laser power, excited at 400 nm.

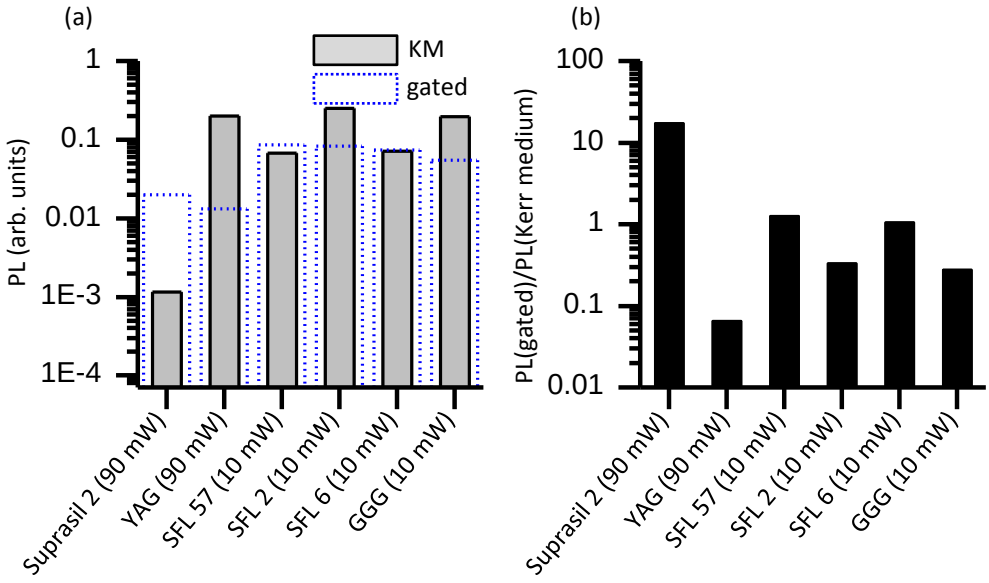

Figure 3.7: Comparison of candidate Kerr media. (a) Integrated Kerr media background fluorescence (black solid outline, gray fill) and gated fluorescence from ZnSe (blue dotted outline, no fill) for different Kerr media as listed. PL is scaled for different laser powers as listed. (b) Ratio of gated fluorescence to Kerr medium background fluorescence.

3.3.5 Sample Environment Control

For the plasmonic nanowires experiment described in Chapter 5, oxygen degrades the plasmonic silver outer coating on nanowires. We designed and constructed an air-tight sample holder to house these samples, and we loaded them in an Argon environment to prevent sample degradation.

For CdSe nanocrystal measurements described in Chapter 4, samples were measured using an Oxford Microstat HE. Temperature control with the Microstat is achieved through continuous flow of liquid cryogens (helium or nitrogen) and a resistive heater controlled by a Cryocon Model 62. A transfer stick is inserted into a liquid helium dewar; the other end of this transfer line flows the cryogen across a cold finger on which the samples are mounted. Flow is achieved by vacuum applied to the exhaust port of the transfer stick. Flow is modulated by a needle valve located at the end of the transfer stick at the bottom of the cryogen dewar. We created a custom feedback loop in LabVIEW to drive a stepper motor attached to this needle valve to maintain temperature as dewar pressures and liquid levels varied through an experiment in concert with the resistive heater.

The membrane vacuum pump line on the transfer stick introduced significant vibrations into the sample position during low-temperature experimental runs. These vibrations were minimized by replacing the short (approximately 5 m), hard-walled plastic tube with a long (approximately 15 m, more flexible Tygon tube that did not transfer vibrations.

The original rear plate of the Microstat HE and coldfinger sample mount had an insufficiently large aperture to measure multiple 2 mm by 10 mm samples during the same experimental run. To resolve this, a custom cold-finger sample mount was fabricated for the Microstat HE to permit mounting of multiple samples simultaneously. A new rear plate was constructed with a larger optical window for absorption measurements in a transmission geometry (see Section 3.4).

3.3.6 Background Reduction In Time-Resolved Photoluminescence

At each delay position, we collect spectra with and without the pump beam exciting the sample. In the absence of the pump beam, the only signal collected by the camera is undesired signal from the gate beam in the fused silica Kerr medium.

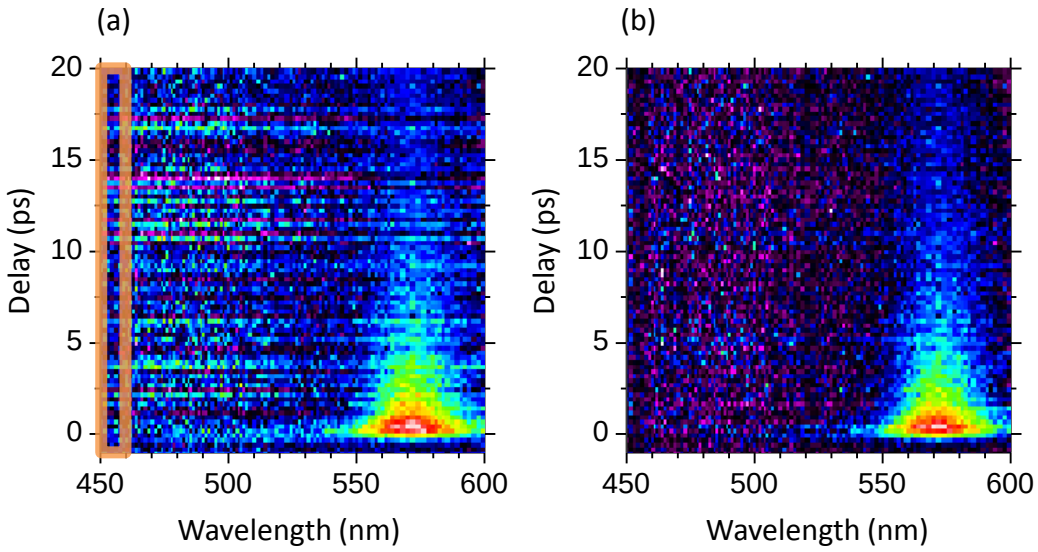

Figure 3.8: TRPL gate background reduction technique example. (a) Raw time-resolved photoluminescence (TRPL) signal. (b) TRPL signal after use of 450-460 nm region to subtract background PL from Kerr medium.

The background emission from the gate beam-excited fused silica and the CdSe quantum dots studied in Chapter 4 are significantly different in their emission peak positions. The Kerr gate background emission in the region of the nanocrystal band-edge emission scales linearly with the background in the 450 nm to 460 nm spectral region. Because QD emission is much weaker from 450 nm to 460 nm, we use this region to infer the magnitude of background emission across the entire collected spectrum in our CdSe QD TRPL scans. The gate background scan collected with each signal scan is scaled proportionate to the 450 nm to 460 nm region and subtracted from the gated signal scans. This results of this

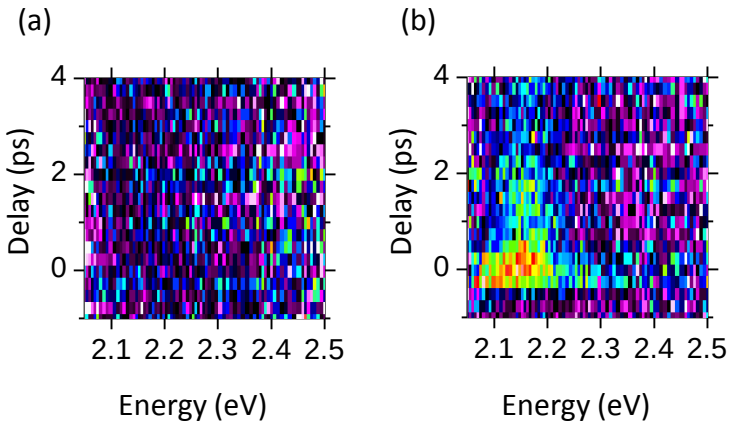

Figure 3.9: (a) TRPL signal from fused silica at 10 K. (b) TRPL signal from CdSe QDs with SCN annealed at 200 ° °C at 10 K under identical exposure and integration conditions.

process are shown visually in Figure 3.8, and it allows collection of TRPL signals at even lower signal levels than would otherwise be possible.

Additionally, we verify that the fused silica sample substrates produce no measurable TRPL signal at our excitation fluence. Figure 3.9a shows the TRPL signal for a fused silica substrate at 10 K. Figure 3.9b shows an identical scan on a QD sample.

3.3.7 Kerr Medium Mounting

We observed that strain-induced birefringence can degrade the achieved polarization contrast ratio when Kerr media are mounted using retaining rings. To minimize this contrast reducing effect, we mount Kerr media in a strain-free manner with Crystalbond 509:

- A small piece of Crystalbond 509 is placed onto a brass mount.
- The KM is placed on top and both are heated with a hot plate until the Crystalbond melts.

- The KM is lightly pressed at opposing edges with wood tips of laboratory cotton swabs to ensure parallelism with the mount.
- The KM is removed from heat and an inverted borosilicate glass beaker is used to prevent dust contamination of the Kerr medium surface.

3.3.8 Kerr Medium Position Optimization

Because of the intensity of the gate medium, even small defects in the surface of the Kerr medium produce background noise in TRPL measurements. Lateral position of the Kerr medium is controlled by two micrometers that can be driven with stepper motors. Prior to TRPL scan sequences, an optimal position for the Kerr medium is determined by rastering its position and collecting Kerr medium background fluorescence spectra at each location. Initial checks are performed using the infrared optical viewer to detect scattering off of dust, and we then raster across the Kerr medium surface using these stepper motors to find the location with minimum PL in the range of interest.

3.4 Time-Resolved Absorption Apparatus

The 1 kHz, 800 nm, 120 fs output from a regenerative amplifier (Spectra-Physics Spitfire) is sampled with an uncoated UV fused silica wedge. This low fluence beam is focused through a 0.375 inch sapphire plate to generate a pulsed white light continuum. After sampling, the majority of the 800 nm beam is frequency doubled in a BBO crystal to generate the 400 nm pump beam for photoluminescence (PL) and time-resolved measurements.

Time-resolved absorption measurements are performed without rastering because we must detect changes in $\Delta T/T$ to 10^{-3} , and, even with high quality films, translating the sample during measurement introduces larger systematic imbalances between the sample

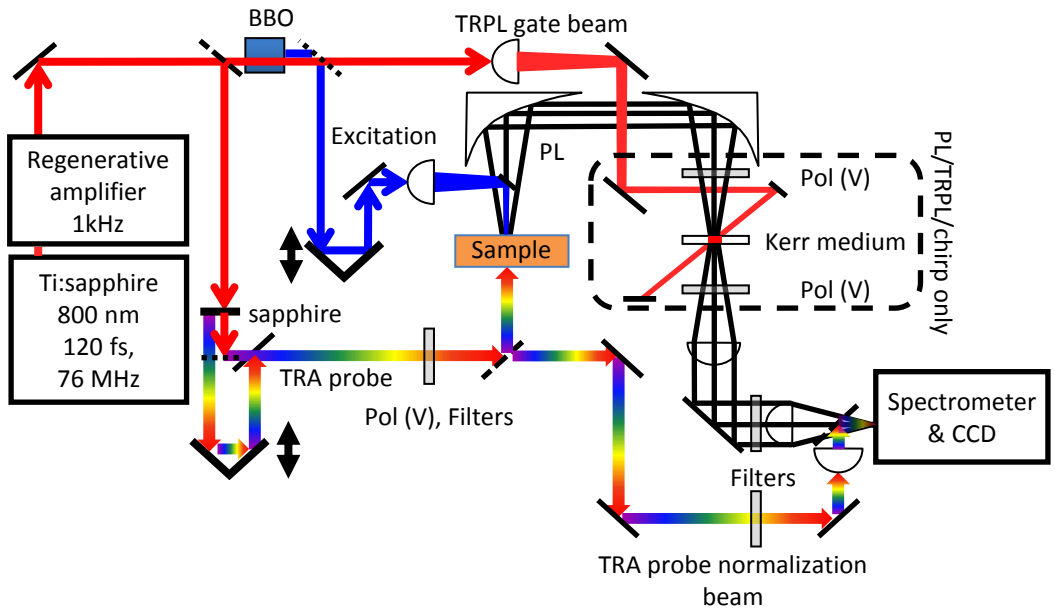

Figure 3.10: Schematic of combined time-resolved photoluminescence and absorption apparatus. Polarizers are co-polarized (V) for DC PL measurements and cross-polarized (V, H) for TRPL / chirp measurements. Dotted lines show dichroic optics; dashed lines show broadband splitters.

and reference arms. To compensate, we employ low excitation powers and design scans to monitor the reproducibility of measurements, as described for our quantum dot studies in Section 4.4.1. Sample locations are chosen to have an optical transmission between 0.4 and 0.65 at the band-edge exciton ($1S_{3/2h}1S_e$) absorption, and we observed generally higher signal to noise ratios for more transmissive samples. At each time delay, different configurations of the white light beam (W) and pump beam (P) are used: pump only (P) to record PL, pump and white light probe ($P+W$) to capture time-resolved absorption, and white light probe only (W) to normalize any sample changes with time. The white light beam is split into reference and sample arms to normalize any fluctuations in white light generation. Signal and reference beams are vertically displaced at the entrance to the spectrometer and on the CCD to collect signal and reference arm spectra concurrently for

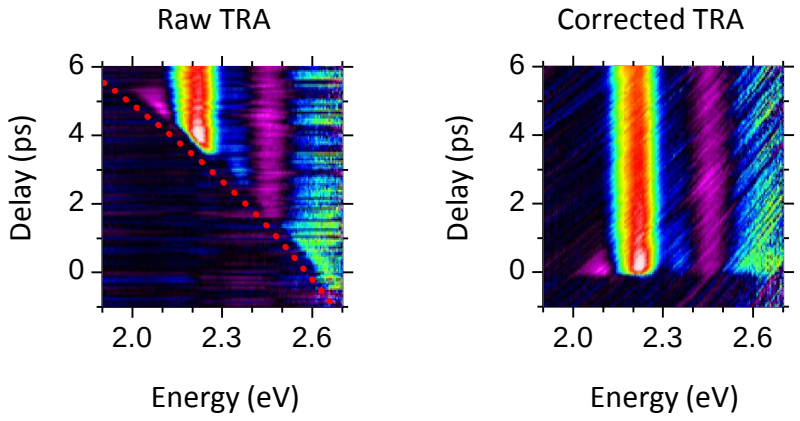

Figure 3.11: White light supercontinuum chirp removal example. (a) Raw time-resolved absorption map overlaid with the temporal profile of white light probe (red dotted line). (b) Time-resolved absorption map after correction for chirp of white light probe.

each beam configuration. TRA signal is then calculated as follows:

$$\frac{\Delta T}{T_0} = \frac{(S_{P+W} - S_P) - \frac{S_W}{R_W}(R_{P+W} - R_P)}{\frac{S_W}{R_W}(R_{P+W} - R_P)} \tag{3.19}$$

where subscripts denote the presence of the white light beam (W) and the pump beam (B) and S and R refer to the detected signal and reference beams, respectively. To prevent ghosting during readout, beams are shuttered electronically during the CCD exposure window using the Pockels cells in the regenerative amplifier. The reader is referred to Ref. 203 for additional discussion of noise reduction in TRA experiments.

3.4.1 Chirp Correction

A schematic for the chirp correction method is shown in Figure 3.11. Raw time-resolved absorption scans (Figure 3.11a) show clear evidence of wavelength-dependent temporal delays. The time dependence of the white light supercontinuum (Figure 3.11a, red dotted line) is measured using the optical Kerr gate in the off-axis configuration ("TRPL") shown

in Figure 3.2. The split-off 800nm that generates the supercontinuum is mechanically delayed relative to the gate beam. This delay is then varied to capture the entire temporal profile of the supercontinuum.

TRA maps are corrected at short time delays ($t < 10$ps) to account for actual arrival time of different wavelengths, causing the diagonal streaking shown in Figure 3.11b as lower energy features are corrected to earlier times. Although the temporal precision of TRA features is limited to the duration of the white light pulse, the temporal accuracy is limited to the precision of the chirp measurement via the OKG. We estimate the error in our chirp calibration does not exceed $2.6\,\mathrm{fs\,nm^{-1}}$. The supercontinuum temporal profile used for this correction was measured with the microstat and fused silica substrate in place. We note that it may be possible to use thinner white-light generating media that would produce significantly less chirp in the white light supercontinuum. The chirp may in the future also be characterized by observing TRA signals on a blank cover slip or substrate.[203, 149]

3.5 Experimental Optimization

Through the development of the low-temperature time-resolved photoluminescence and absorption apparatus, numerous opportunities arose for improvements in experimental run stability and signal quality. Below, we detail some of these observations and the techniques used to improve data collection.

3.5.1 Laser Stability

White light supercontinuum generation, frequency doubling of the 800 nm fundamental beam to 400 nm, and the optical Kerr effect are all non-linear processes. Because of this, we noticed that fluctuations and drift in the stability and power of the fundamental 800 nm beam caused degradation in the stability and performance of TRPL and TRA.

The final output of the Spitfire is the combined result of many processes and feedback loops as shown schematically in Figure 3.12. A continuous wave (CW) Coherent Verdi V-5 at 532 nm and 4.55 W drives a Coherent Mira 800 producing an 800 nm pulse with 10 nm bandwidth with approximately 1 W total power and 120 fs pulses at 76 MHz. The Mira pulses seed the Spectra-Physics Spitfire regenerative amplifier which selects one pulse per millisecond and amplifies it to 1 mJ. To do this, the pulses to be amplified are stretched in time, selected for amplification with polarization optics, amplified, and then recompressed. Pockels cells controlled by the Synchronized Delay Generator (SDG) are electrically driven to trap and dump pulses in the amplification cavity of the Spitfire. The Spitfire amplifier is pumped by a Spectra-Physics Evolution X Q-switched laser at 1 kHz and 7.4 W with pulses of order 100 ns. While the Coherent Verdi and Mira were found to be extremely stable with turnkey operation, we observed a slow degradation in the output of the Evolution X that pumps the regenerative amplifier, thereby introducing instability in the Spitfire output. The Evolution X has several internal temperature control systems which we will discuss below.

Thermal control in the Evolution is provided by a combination of resistive electrical heaters and chilling water from a Lytron chiller. The AlGaAs diodes in the Evolution are temperature controlled using a closed loop multi-channel temperature controller. Each diode has a heatsink cooled by the Lytron water flow and heated by a resistive electrical heater; the temperature controller produces a stable temperature, typically between 65 °F and 80 °F, by balancing the heater with the heat flow of the liquid. We observed a slow drift of the optimal temperature of these diodes on the time scale of months and any time the Lytron water temperature changed.

Similarly, the frequency-doubling LBO crystal was also found to have a drift in optimal temperature on time scale of months. At the ideal temperature, the output of the Evolution decreases symmetrically with respect to fluctuations in temperature. Off-peak, however, these fluctuations lead to increases or decreases in Spitfire output as the temperature drifts

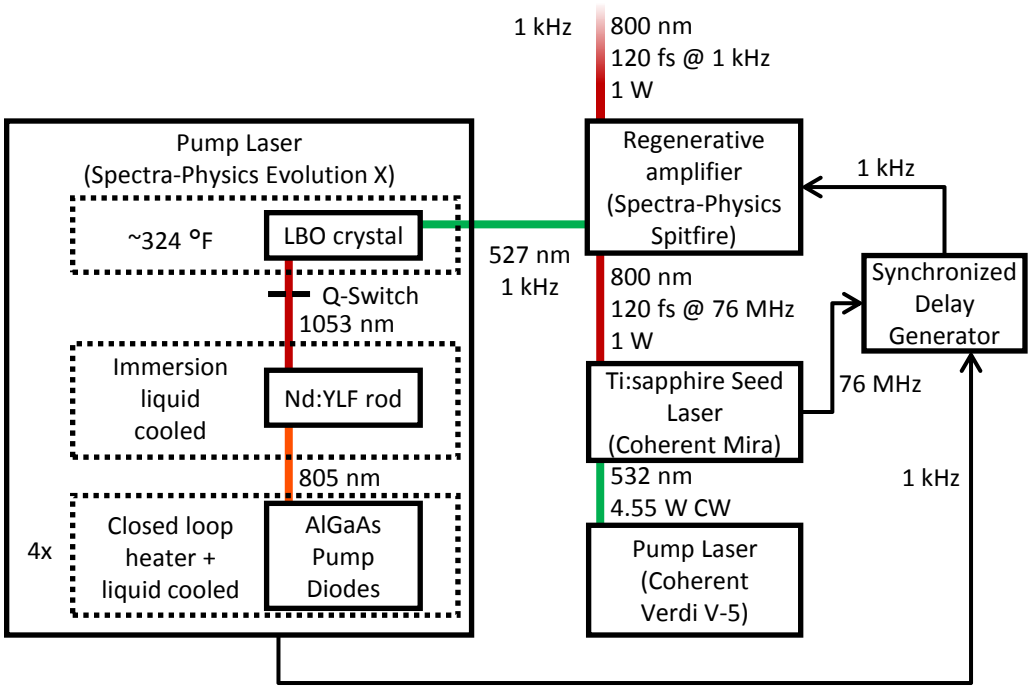

Figure 3.12: Schematic of laser processes and temperature control.

toward or away from the optimal temperature, as shown in Figure 3.13. Whether the output power fluctuations are correlated or anticorrelated with deviations from the ideal Evolution LBO temperature may depend on when during amplification the pulse is dumped from the regenerative amplifier cavity.

3.5.2 Laser Chilling System

Another large factor in experiment performance is a slow degradation of output from the Evolution X. We found that this decrease in laser power of up to 10% can be directly connected with cleanliness of the liquid cooling system. In the Evolution, the cooling water envelopes the Nd:YLF lasing medium rod which is pumped in four locations by the 805 nm diode pump beams through this cooling water. We show a schematic layout, including

one diode pump beam, in Figure 3.14. Although the chilling lines are filtered with a 1 µm GE Hytrex filter, any debris that develops in the cooling water has the opportunity to be burnt into the laser rod or the window toward the diodes. Such an aggregation will directly degrade the overall performance of the Evolution output.

We used several mechanical and chemical methods to mitigate this degradation. Mechanically, we replaced the graphite rotary vane pump (Fluid-O-Tech) originally installed on the Lytron chiller with an external, magnetically driven centrifugal pump (Little Giant TE-6-MD-CK) with a carbon-filled Kynar housing and impeller and a mica-filled teflon bushing. Although this pump is designed for high flow and low pressure, it is expected to produce minimal debris in the chilling water. Additionally, we installed an ultraviolet mercury lamp in the chiller tank, but this was not found to change the overall buildup of material significantly.

Separately, several chemical procedures were found to improve the laser output performance as we describe below.

Vinegar Purge

Vinegar (dilute acetic acid, consumer grade), was recommended to clean off any organic debris on the laser rod. The procedure we used is as follows:

- Disconnect chiller, pump, and filter from Evolution.
- Properly dispose of treated cooling water if desired and drain hoses connected to Evolution.
- For cleaning Evolution only (not the chiller):
  - If only cleaning the Evolution, fill an external reservoir with 1.5-2 gallons of distilled, filtered water and 0.5 L commercial vinegar.

  - Connect small external pump (Little Giant 2-MD-SC), Evolution, and reservoir in closed loop

- For cleaning entire chilling loop, fill Lytron with distilled water and 0.5 L of commercial vinegar.

- Circulate for 6-12 hours. Monitor for signs of discoloration in water that can indicate chemical reactions with metal connections in Evolution. Inspect solution, dispose, and repeat.

- Flush system with distilled water at least four times prior to reconnecting with chiller system.

- Fill chiller with treated cooling water or distilled water and circulate with new 1 µm filter in place for sufficient time to remove any residual debris prior to activation of Evolution.

We note that we have observed, after several days of vinegar purging, a blue tint consistent with copper acetate in the color of the water. The vinegar cleaning was stopped at this point to prevent any further damage to the system.

This vinegar purge, followed by distilled water filling of the chiller, was found at times to provide up to a 5% increase in the system output from 9.5 W to 10 W.

Pluronic P-123

Pluronic P-123 is a high molecular weight (number average molecular weight 5800) triblock-copolymer (poly (ethylene oxide), poly (propylene oxide), poly (ethylene oxide)) surfactant manufactured by BASF found to efficiently disperse graphene in aqueous solution.[75]

We found that overnight circulation of a 5% (by weight) solution of P-123 in a system with degraded performance led to an 8% increase in the output of the Evolution (from 8.4 W to 9.1 W). After the P-123 cleaning, we observed that the temperature tuning of the diodes and steering of the high reflectors in the laser cavity each produced an additional 2% increase (from 9.1 W to 9.3 W to 9.55 W) in the power output of the Evolution. A subsequent vinegar cleaning as described above further raised the total output by 4% to 10 W. Additional cleaning with P-123 was not found to increase power further. Further tests indicate that P-123 followed by vinegar may be equalled in effectiveness by vinegar alone.

Although P-123 is soluble in water, its high viscosity and slow rate of solution requires careful attention during solution preparation. Small quantities of P-123 were added at a time to a two-gallon reservoir circulated in closed loop with a centrifugal pump to prevent clogging and freezing the centrifugal pump. P-123 was observed to leave a slippery residue and required at least four rounds of water purges through the Evolution to remove residue and bubbles.

Nalco Treated Water

Following a new recommendation from Spectra-Physics, we worked with two solutions from Nalco: 460-CCL2567, an alkaline closed loop cleaner, and 460-PCCL104, a premixed liquid corrosion inhibitor. PVC gloves, labcoat, and goggles are recommended for handling these chemicals.

- Drain the entire closed loop system.
- Replace the GE Hytrex filter.
- Fill cooling system with Nalco 460-CCL2567 without dilution.

- Circulate for at least 8 hours. Recommend circulating overnight.
- Completely drain system and purge with distilled water four times and circulate for 15 minutes.
- Drain system and replace filter.
- Fill cooling system with Nalco 460-PCCL104 corrosion inhibitor at full strength.

We found that this procedure and coolant produced a 6% increase (from 9.4 W to 10 W) and maintained similarly high power levels for up to six months. Further cleaning with P-123 and vinegar did not enhance the overall power output compared to the Nalco treatments alone. This is our recommended solution for cleaning and preventing corrosion.

3.5.3 TRPL: Sample Rastering

During TRPL measurements on the CdSe thin films samples studied in Chapter 4, the sample is continuously translated in-plane to prevent sample degradation. Raster patterns are chosen to remain on optically dense regions of the sample and typically sampled 2 mm^2 to 5 mm^2.

Initially, the Microstat HE was mounted on micrometer-driven stages designed for high-precision positioning (Newport series UMR8 stage and 460P micrometer). Rastering was achieved by attaching gears to the micrometers that drive these stages and then driving these gears with stepper motors.

During low temperature operation, a transfer stick connects the Microstat HE to the liquid helium dewar. Continuous rastering with the load of the mounting block, Microstat, and liquid helium transfer line led to unexpected sticking and freezing of the micrometers driving these stages during experiments. Micrometer motion was improved by regreasing with Green Grease, but slipping eventually occurred again.

We redesigned the Microstat mounting configuration and replaced these stages with a heavy duty lead-screw driven stage (Aerotech ATS-302). Bearings and lead screw were greased with Green Grease and have since performed without problems, although we note that the manufacturer has recommended using Starrett Tool Oil on the lead screw with Kluber Isoflex LDS18 Special A grease on top of this oil in the case that problems arise.

The ATS-302 stage has a lead of 0.5 mm. We drive the horizontal stage with a gear reduction of approximately 3:1 and the vertical stage with a reduction of 2:1. Both stages are driven by SST42D1040 stepper motors by Shimano Kenshi Corporation.

3.5.4 TRA Noise Reduction: Pump and Probe Beams

Because both signal and reference arm spectra are collected during the same CCD exposure, it is important to avoid cross-contamination of beam spots between CCD regions. We prevent this issue by focusing the white light supercontinuum beam *after* a 300 µm pinhole and then telescoping the image of the pinhole onto the sample. When the sample and pinhole are co-focused, the illuminated region of the sample is defined by the pinhole and can be positioned appropriately on the CCD. This reduces noise due to fluctuations in beam size from supercontinuum generation instabilities and from noise due to air currents. Even minor fluctuations in the beam position and size can produce relatively large noise because the magnitude of TRA signals is at the 10^{-3} level.

Room air currents are additionally reduced by enclosing the entire experiment. This improves directional stability of the white light probe and 3 eV pump beam on the sample.

3.5.5 TRA Noise Reduction: Pulse Timing

As described above, the signal and reference arms are both collected by the same CCD using two vertically separated regions of the chip. Spectra are collected by digitizing the

full frame of the CCD and then vertically binning the top and bottom halves separately in post-processing. Overall TRA spectra at a given delay are collected by acquiring typically 30 spectra and averaging them.

The maximum digitization rate of the SPEC-10 is 1 MHz, corresponding to a 134 ms readout time for a full frame image on a CCD with 1340x100 pixels. With a 1 kHz laser repetition rate, this finite readout time implies that 134 pulses from the laser will impinge on the CCD during readout if the laser is enabled. It is therefore necessary to prevent exposing the CCD to light during this readout sequence. The simplest approach would be a mechanical blocking mechanism such as a shutter or blocking card controlled by stepper motor. The long duration of TRA scans and the high number of exposures would quickly lead to wearing out many shutters. With the typical 300 ms exposure used in these experiments, one million activations occur within ten days, thereby limiting the utility of magnetic optical shutters. As configured, stepper-motor controlled blocking cards do not have the time precision necessary to clip beams symmetrically as needed here.

We circumvented these hardware limitations through computer control of the Synchronized Delay Generator (SDG) that electrically controls the Pockels cells inside of the Spitfire regenerative amplifier. Pockels cell 2 controls whether amplified pulses leave the amplification cavity. The SDG can be computer-controlled via an RS-232 serial port. To prevent ghosting, we use a buffer of 50 ms before and after dumping the Spitfire pulse to ensure the CCD is ready for collection and that dumping has completed prior to collection of charge. This is schematically shown in Figure 3.15.

3.5.6 TRA Noise Reduction: Sample Position

As shown in Figure 3.16, different sections of the same sample (labeled Region 1 and Region 2) can demonstrate a significantly different noise profile. We recommend checking

at various locations on solid samples to determine the most uniform region to avoid noise due to steering deviations.

3.5.7 TRA Noise Reduction: Recommendations

The experimental optimizations described in this Chapter led to significant overall improvements in the noise of TRA measurements as shown by comparing the "Initial" and "Optimized" curves in Figure 3.16. Here we briefly outline recommendations for minimizing noise in the TRA system.

- Verify optimization of Evolution LBO temperature and Spitfire pulse selection. (Section 3.5.1)
- Using the CCD and spectrometer in 2D imaging mode, ensure that signal and reference beams are well separated, equal in size, and well defined by the pinhole. (Section 3.5.4)
- Optimize pump and probe beam noise with no sample in place to minimize noise from sample.
- Optimize SDG timing to prevent ghosting. (Section 3.5.5)
- Check multiple sample locations to determine smoothest region with best noise profile. (Section 3.5.6)
- Use filters on signal and reference arms to record as flat of a spectrum as possible on both signal and reference arms and filter for optimal pixel counts in 2D imaging.

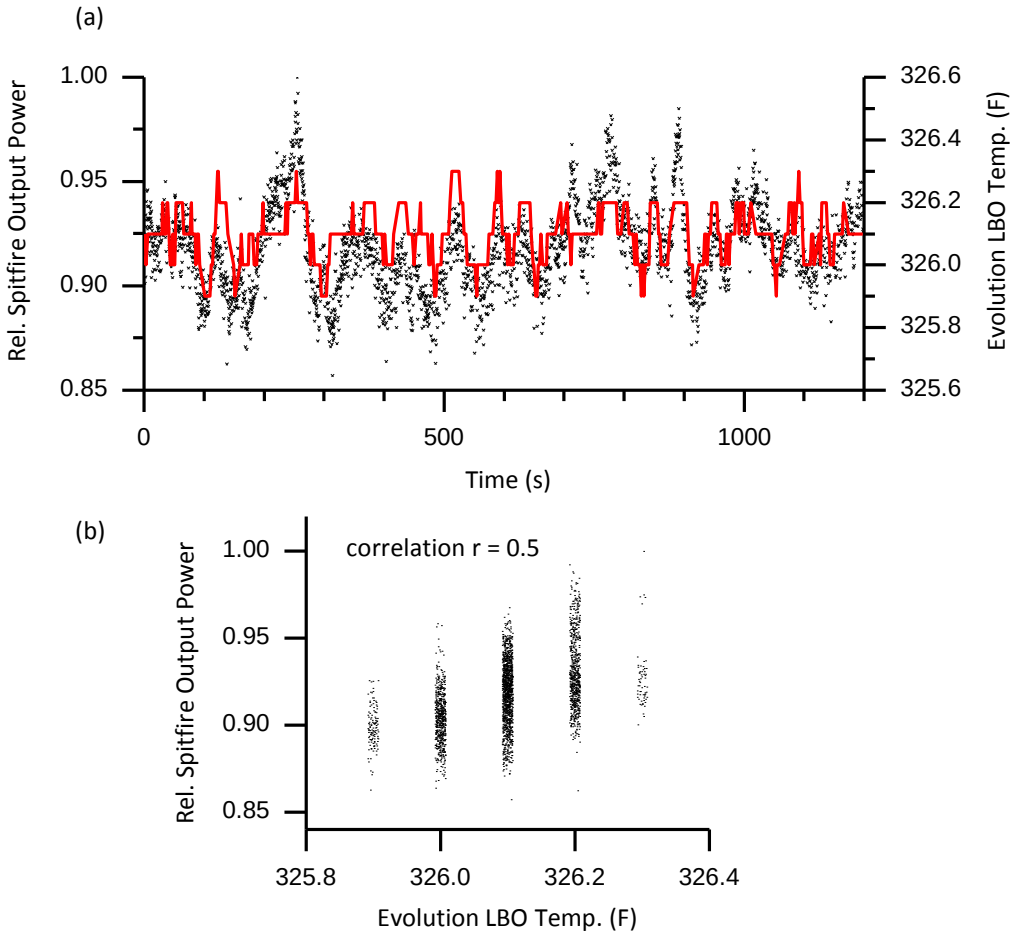

Figure 3.13: Noise due to Evolution LBO temperature fluctuations. (a) Monitored, scaled output of Spitfire regenerative amplifier (black $\times$, left axis) and Evolution LBO crystal temperature (red line, right axis) vs. time. (b) Spitfire output vs. Evolution LBO crystal temperature, showing positive correlation. Points have been horizontally spaced at each temperature for ease of viewing.

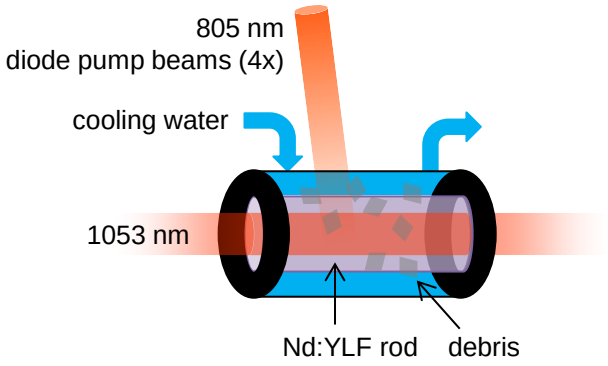

Figure 3.14: Schematic of Evolution-X Nd:YLF rod apparatus

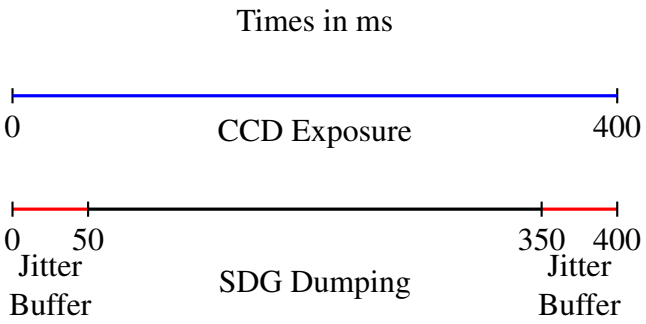

Figure 3.15: Schematic of delays and exposure lengths used with the SDG to eliminate ghosting during TRA signal readout.

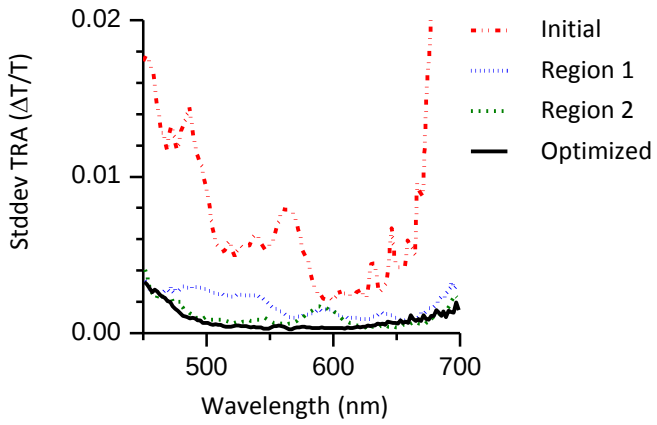

Figure 3.16: Noise reduction in TRA. Standard deviation of TRA signal vs. wavelength for several configurations: as initially configured (red dot dot dash), for two different regions of the sample (blue dash, green dot), and optimized (black, solid).

Chapter 4

Ultrafast Electron Trapping in Quantum Dot Solids

4.1 Introduction

Semiconductor quantum dots (QDs) have been the focus of intense study for their size-tunable properties with applications in light-emitting devices, photovoltaic devices and printable electronics [137, 120, 86, 213, 121, 118]. The size, shape, composition, and surface chemistry of QDs, as well as their temperature and local environment, are all of great importance, modifying photoluminescence (PL) yields, shifting optical transitions, and impacting electrical conductivity.[189, 161, 87, 105, 163, 10, 52, 30, 35, 27, 119, 142]. Time-resolved optical spectroscopies can directly monitor relaxation pathways that respond sensitively to these parameters, and there exists a rich literature measuring the population-averaged response of QDs dispersed in solutions and polymer matrices.[124, 209, 109,

29, 74, 133] To date, ultrafast optical studies of close-packed colloidal QD solids have been more limited in number,[228, 136, 62, 35, 15, 223] and although the majority of these studies have typically been performed at room temperature, measurements at low temperature offer the potential for increased sensitivity to environmental changes as well as a sharper view of relaxation processes.

In this Chapter, we study the impact of surface treatment on the low temperature (10 K) optical properties of CdSe QD solids. The ligand exchange and annealing process used here[52] has laid the foundation for high mobility CdSe field effect transitors we will discuss in Chapter 7. Here we employ time-resolved absorption (TRA) and photoluminescence (TRPL) spectroscopies to gain insight into the ligand exchange and annealing process through excited state dynamics. Because both TRA and TRPL implementations developed here are broadband with sub-picosecond time resolution, we are able to show that exchanging aliphatic native ligands (NL) for thiocyanate (SCN) and subsequently annealing the samples increases electron trapping rates by two orders of magnitude. We demonstrate a need to modify the conventional interpretation of CdSe QD time-resolved absorption spectra in this experimental configuration and show that the electron, not the hole, traps first out of the core excitonic state.

4.2 Results and Discussion

Time-*integrated* optical absorption spectroscopy is routinely used for the characterization of QD systems, providing information on sample size and homogeneity, as well as interparticle coupling.[250, 55, 140] As previously reported for similar samples, SCN ligand substitution and thermal annealing shifts and broadens the quantized band-edge optical absorption peak ($1S_{3/2h}1S_e$ in the effective mass approximation[178]) in these QD solids (Figure 4.1).[52] Whereas time-integrated absorption reflects the optical properties of core states,[141]

time-integrated band-edge PL is heavily impacted by conditions that influence carrier trapping to the surface.[107, 189] We study four samples: CdSe QDs with native, aliphatic ligands (NL); native ligands exchanged for SCN (SCN); exchanged and subsequently annealed at 100°C (SCN 100C); and exchanged and subsequently annealed at 200°C (SCN 200C). As previously shown by several of us using scanning electron, atomic force, and optical microscopies on identically prepared samples, the sample preparation and spin coating process used here and described below produces uniform, randomly close-packed, optically smooth, and crack-free thin films over large areas.[27] Fourier transform infrared spectroscopy (FTIR) shows that SCN exchanges 90% of the NL ligands used in synthesis, and that annealing to 200°C significantly decomposes SCN.[27]

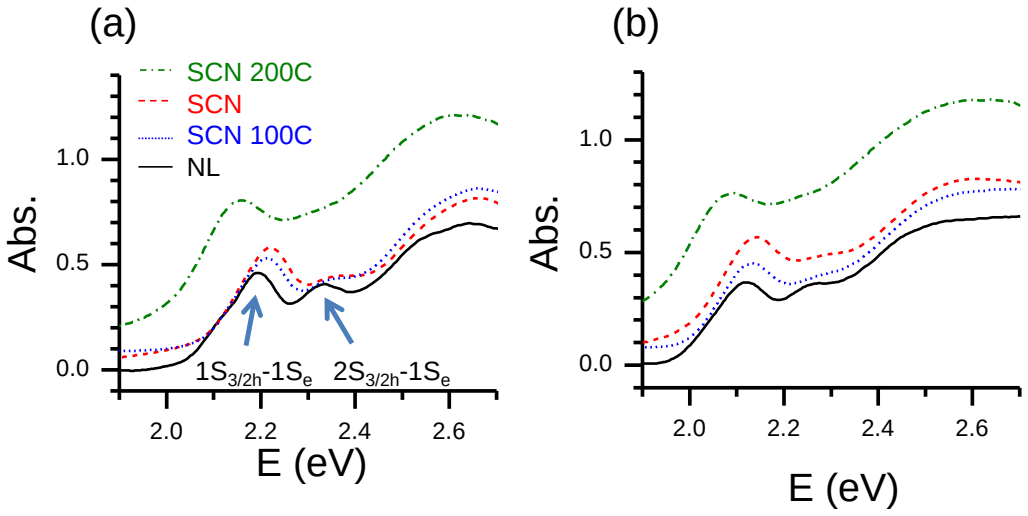

Figure 4.1: Optical absorption at (a) 10 K and (b) room temperature for CdSe QD solids. CdSe passivated with NL (black, solid line), SCN (red, dashed line), SCN annealed at 100°C (blue dot), SCN annealed at 200°C (green dash dot). Arrows (a) mark optical transitions.

The exchange and annealing processes dramatically decrease both the total integrated PL (band-edge plus sub-bandgap, surface emission) and the relative strength of band-edge PL compared to surface emission (Figure 4.2). While band-edge PL requires both an

electron and a hole in a QD core state,[138] sub-bandgap PL involves QD surface states for which carrier hops back to higher energy core states require thermal fluctuations unlikely at 10 K.[10, 162, 229, 18, 161] Band-edge photoluminescence is therefore unlikely after any carriers have trapped to surface states, and the decreased band-edge PL relative to surface emission after exchange and annealing is a signature of an increased surface trapping rate in these samples.

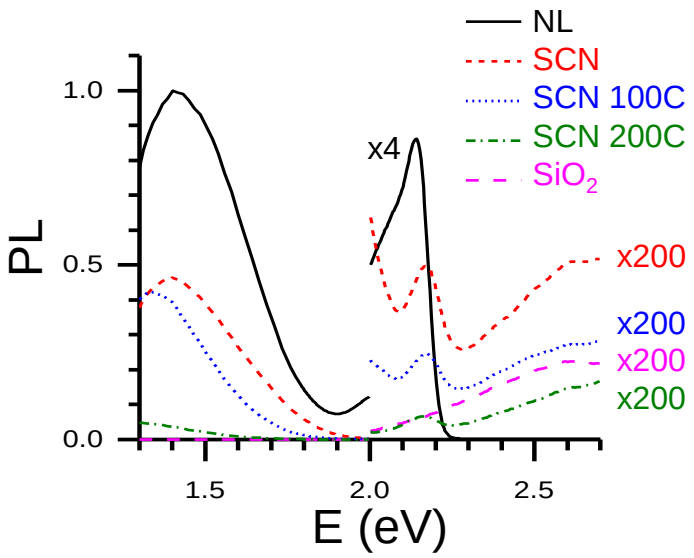

Figure 4.2: Photoluminescence spectra excited at 3.1 eV at 10 K for CdSe QD solids and fused silica (SiO_2) substrate. CdSe passivated with aliphatic native ligands (black, solid line), SCN (red dashed line), SCN annealed at 100°C (blue dot), and SCN annealed at 200°C (green dash dot).

Representative room temperature time-integrated optical absorption spectra for nanocrystal solid samples used in measurements are shown in Figure 4.1b. Apparatus movement during cooldown prevents measurement of identical regions at room temperature and 10 K. As is the case at low temperature (Figure 4.1a), an initial blueshift is present upon exchange of aliphatic native ligands (NL) for SCN, followed by subsequent redshifts after annealing to 100°C and 200°C. All samples exhibit similar blueshifts in the energy of the ground state exciton absorption after cooling to 10 K from room temperature (Figure 4.1).

Integrated photoluminescence at and below the band edge, scaled relative to NL at 10 K, is shown for all samples in Figure 4.3a after spectral and Jacobian corrections.[160] Band-edge emission is calculated by integrating PL from 2.06 eV to 2.30 eV; surface emission is determined by integrating over all measured photon energies below 2.06 eV. We plot the surface to band-edge quantum yield (QY) ratio for all samples in Figure 4.3b, showing that the surface PL becomes relatively stronger after exchange.

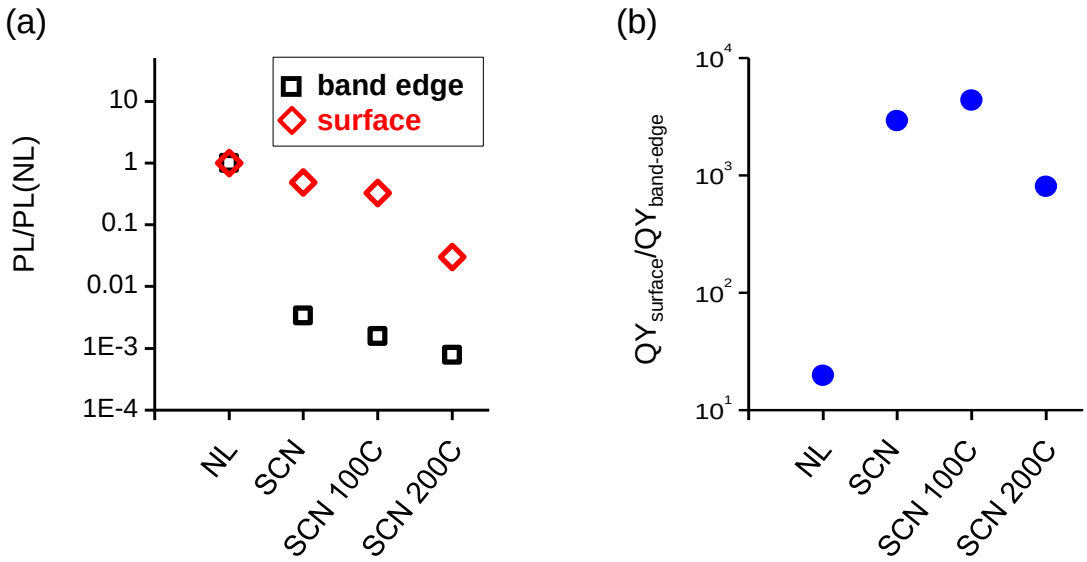

Figure 4.3: (a) Integrated photoluminescence (PL) at 10 K of QD films at band edge and surface relative to the NL sample. All samples are excited with the same total power and power density, and are virtually opaque at the excitation density of 400 nm. (b) Relative quantum yield (QY) ratio of surface emission to band edge emission.

As discussed in Section 3.1, time-resolved photoluminescence (TRPL) measurements can provide more direct insight into the non-equilibrium kinetics of QDs and help to clarify the interplay of core and surface states.[102, 10, 100, 229, 66, 243, 165, 101] Previous TRPL studies have demonstrated long radiative lifetimes from surface trapped states, attributing these trap states to electron traps at unpassivated Cd or hole traps at unpassivated Se.[10, 229, 18] Annealing to 100°C is not expected to change the QD surface properties

significantly, whereas annealing to 200°C decomposes SCN and we may then expect a concomitant change in charge dynamics.[27]

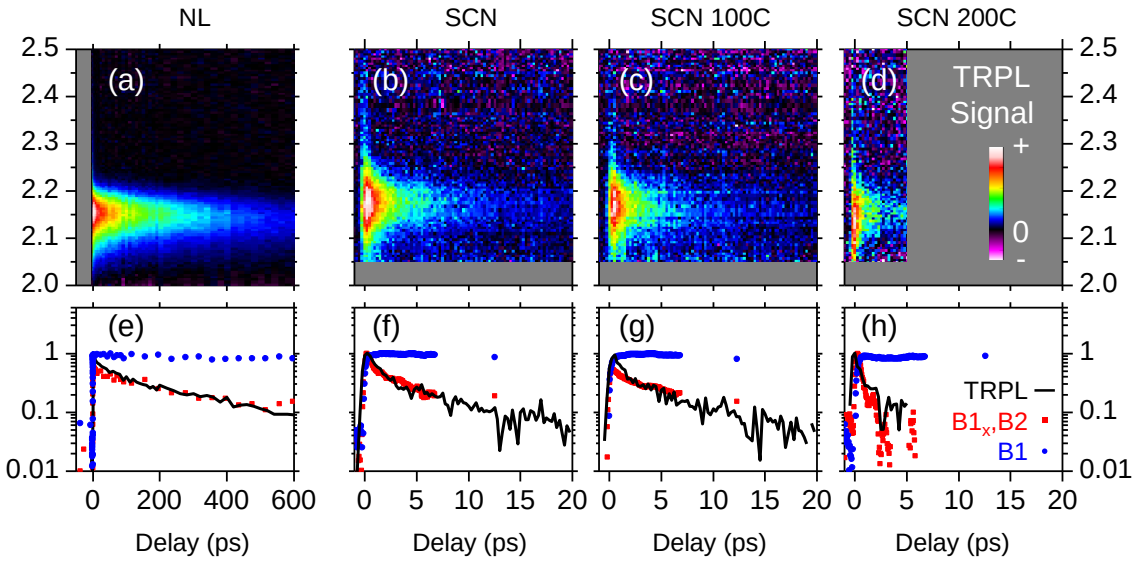

Figure 4.4: (a-d) Time-resolved photoluminescence spectral maps at 10 K for CdSe QD thin films with (a) NL, (b) SCN, (c) SCN annealed at 100°C, and (d) SCN annealed at 200°C. (e-h) Spectrally integrated TRPL (black) compared and contrasted with TRA features $\{B1_x, B2\}$ (red) and B1 (blue). Note that (a, e) show different timescales than (b-d, f-h). TRPL maps are scaled for contrast.

TRPL measurements, shown in Figure 4.4, reveal dramatic decreases in band-edge PL lifetime with ligand exchange and annealing, showing that changes in time-integrated PL reflect dynamical changes upon QD surface treatment. The PL signal from the pristine NL sample decays over hundreds of picoseconds in agreement with previous short-time TRPL measurements,[165] but the exchange of NL for SCN drastically shortens the PL lifetime to tens of picoseconds. Annealing the exchanged sample at 100°C leaves TRPL decays largely unchanged, but further annealing to 200°C hastens the TRPL decay so the observed transient approaches the instrument response limit. The decreases in TRPL lifetime in exchanged and annealed samples echo decreases in time-integrated band-edge PL (Figure

4.2), and indicate increased capture rates of the bright exciton by pathways other than band-edge PL. The latter may include non-radiative relaxation, although the increase in relative quantum yield for surface state emission (Figure 4.3) indicates that some portion emerges as surface PL.

Our PL data, taken by itself, could be rationalized in terms of our surface treatments. In particular, decay pathways alternative to band-edge PL could arise from a higher trap density upon exchange, which is further increased upon annealing at 200°C. The replacement of NL by SCN (without annealing) increases the number of electron and hole traps on unpassivated surface atoms due to reduced overall surface coverage,[52, 28] and is expected to further introduce hole traps associated with the SCN ligands,[28, 18] so the appearance of additional traps after exchange is easily understood.[98] Moreover, thermal annealing to 200°C decomposes SCN and leaves S atoms bonded to Cd,[76, 27] a process likewise expected to increase the number of hole traps in the SCN 200C sample.[119] Although these increases in hole trap density could account for the progressive decrease in PL lifetimes, considerations of TRA described below indicate an increase in *electron* trapping.

Time-resolved absorption (TRA) measures pump-induced changes in transmission, $\Delta T/T_0$, subsequent to pump excitation (see Section 3.1). Quantum dot TRA measurements have a long history in measuring carrier relaxation and the impact of surface treatments, and signals emerge from numerous effects including bleached transitions from state-filling, shifts in absorption spectra leading to photoinduced absorptions, exciton-phonon coupling that modulates TRA signals, and optical gain.[189, 109, 130, 208, 205, 204, 127] Prior TRA experiments have shown that electrons relax quickly to the band edge through Auger heating of the holes[124] and ligand interactions [81] and that holes relax primarily through ligand interactions with minor contributions from phonons.[33] Figure 4.5a superimposes a time-integrated absorption spectrum (black), a scaled exemplary TRA time slice (red), and a corresponding TRA 2D map. Features A1, B1, and B2 are labeled following the convention

introduced in Ref. 128. Figure 4.5b shows schematically the corresponding single particle electron and hole states associated with these transitions.[178] The energetic location and time duration of the photoinduced absorption A1 probe the biexciton binding energy and hot-exciton relaxation,[208, 209] and the presence of the bleach signals labeled B1 and B2 indicate decreased transition strength at the $1S_{3/2h}1S_e$ and $2S_{3/2h}1S_e$ optical transitions, respectively.[128] Because the physical interpretation of time-resolved absorption signals at energies above the B2 feature is complicated by the high density of optical transitions, we do not focus on interpreting those features here.[178]

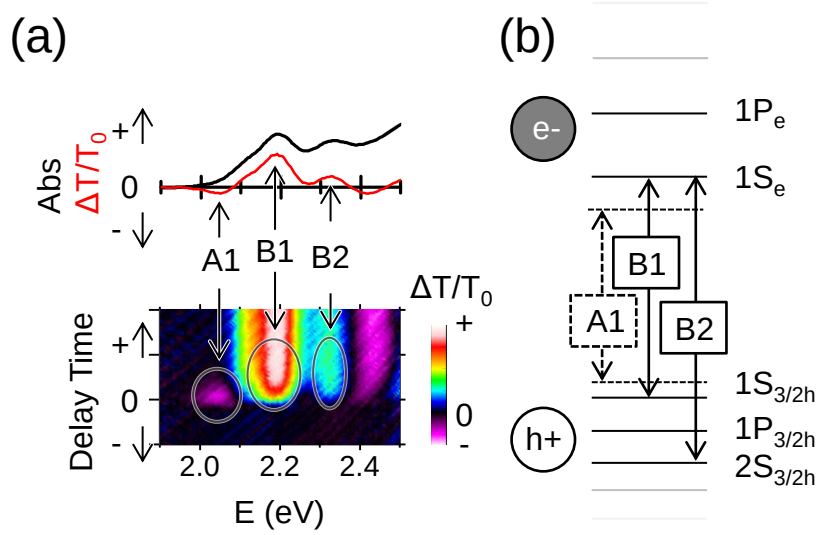

Figure 4.5: (a) Scaled time-integrated absorption spectrum (black) and time-resolved absorption spectrum (red, 0-0.5ps) for CdSe NL QD thin film sample showing photoinduced absorption feature A1 and bleach features B1 and B2. (b) Correspondence between time-resolved absorption features and QD optical transitions as described in text.

These optical transitions can in principle be bleached by the presence of charge carriers in either or both of the constituent hole or electron states of the QD. We will label the sub-components of the B1 bleach as $B1_x$, $B1_e$, and $B1_h$, for which absorption at the $1S_{3/2h}1S_e$ transition is blocked by occupancy of the $1S_{3/2h}1S_e$ exciton, $1S_e$ electron, and $1S_{3/2h}$ hole states of the QD, respectively. Within the band-edge B1 bleach the precise location of $B1_x$,

$B1_e$, and $B1_h$ vary to some extent,[21, 53] but this variation is much less than the separation between the B1 and B2 bands.

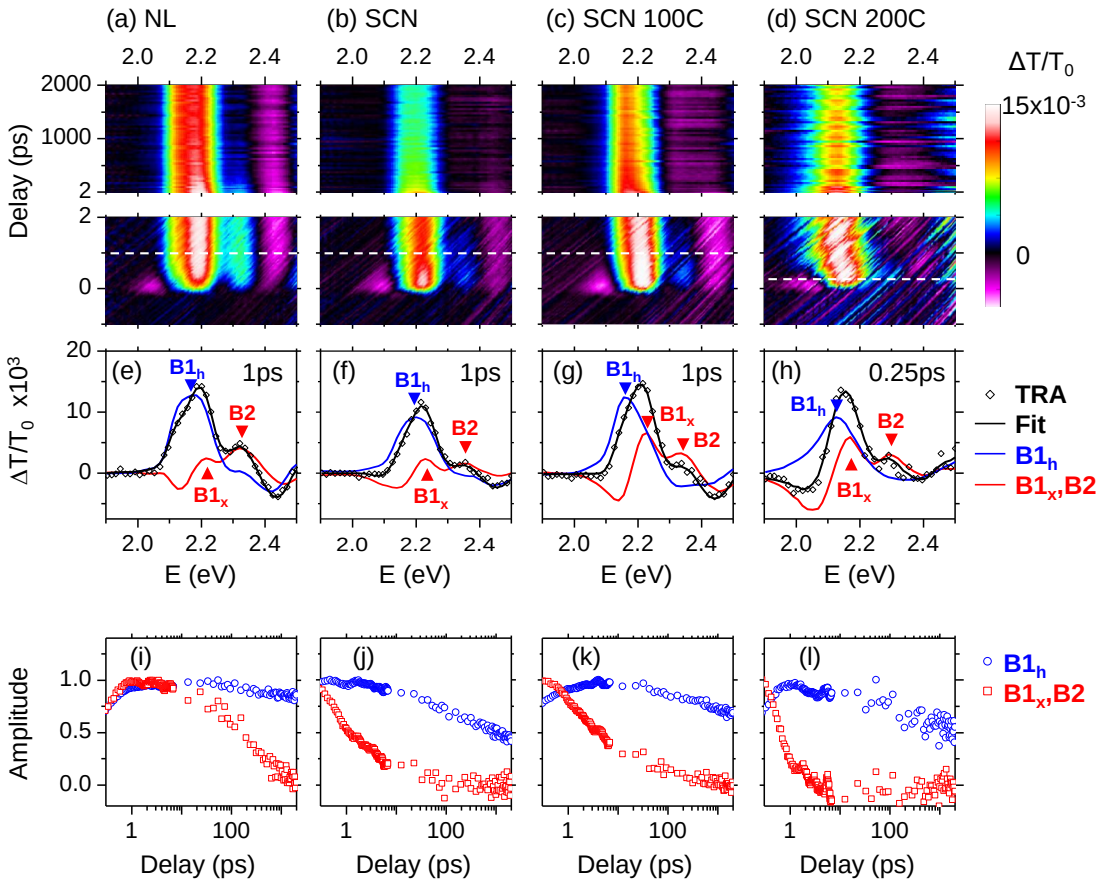

Figure 4.6: Time-resolved absorption (a-d) spectral maps, (e-h) time slices and (i-l) decay profiles at 10 K for CdSe QD thin films. Dotted lines in spectral maps indicate the times for which time slices are taken. Samples are (a,e,i) NL, (b,f,j) SCN, (c,g,k) SCN annealed at 100°C, and (d,h,l) SCN annealed at 200°C. TRA maps are fit using two principal spectra (blue and red lines in e-h) and their decay profiles (blue and red symbols in i-l). Spectral maps are negative-time background subtracted.

The TRA 2D maps in Figures 4.6a-d show that the aggregate B1 bleach in all samples persists beyond the 2 ns time window of this experiment and significantly longer than the sub-nanosecond decay of TRPL observed in all samples. This difference can be quickly seen by comparing TRA B1 (blue) and TRPL (black) curves in Figures 4.4e-h. Thus,

dynamics of B1 are relatively insensitive to surface treatment when compared to TRPL. Because the TRPL decay measures the depopulation of core *excitons*, the presence of B1 well after band-edge TRPL disappears must be due to only $B1_e$ or $B1_h$, or conversion to a dark[175] exciton. Because of the relative similarity of B1 dynamics among the samples and the progressively faster decay of TRPL upon exchange and annealing, we may conclude that the surface treatment process used here predominantly modifies the decay kinetics of only one charge carrier, or accelerates interconversion to the dark exciton.

Further inspection of Figures 4.6a-d indicates that these surface treatments hasten *electron* surface trapping. First, the rapid decay of the A1 absorption feature (circled in Figure 4.5a) shows that excitons relax to the $1S_{3/2h}1S_e$ state within the first picosecond,[209] and since $kT \sim 1$ meV is much smaller than the 100 meV separation of the $1S_{3/2h}$ and $2S_{3/2h}$ states, Boltzmann occupation of the $2S_{3/2h}$ states is minimal. Subsequent dynamics of the B2 bleach therefore cannot reflect $2S_{3/2h}$ hole state occupation and must arise from the $1S_e$ electron. Second, the dramatic changes in decay rate for B2 upon surface treatment are closely matched by similar changes in the TRPL (red and black curves in Figure 4.4e-h, respectively). We may therefore identify electron surface trapping as the process that gives rise to rapid PL quenching and decreases the time-integrated photoluminescence yield in the SCN, SCN 100C, and SCN 200C samples. Note that because transitions to both the $1S_{3/2h}1S_e$ and $2S_{3/2h}1S_e$ exciton states require available $1S_e$ states,[178] an electron in the $1S_e$ state should contribute bleaches to both B1 and B2.[130] At room temperature it has been commonly observed that the decays of B1 and B2 mirror each other, implicating occupation of the $1S_e$ state as a common denominator.[124, 209, 207] In contrast, in our low-temperature measurements the lifetime of the aggregate B1 bleach is much longer than that of B2 for all samples (Figures 4.6a-d and Figures 4.4e-h), which cannot be due to a $1S_e$ electron or a dark exciton. We instead attribute the longer life of B1 relative to B2 to the presence of a long-lived hole in the $1S_{3/2h}$ state and interpret the decay of the B2 bleach as

reflecting the rapid surface trapping of an electron that leaves this hole remaining in the QD core.

The hole contribution to B1 is commonly argued to be small in principle due to greater degeneracy of the hole states and thermal distribution of holes to higher-lying states.[130] To assess the plausibility that the $B1_h$ bleach due to hole state occupation can contribute significantly to the B1 transition at low temperatures, we consider the impact of thermal state occupation on available optical transitions in relevant electron-hole charge configurations. Previous calculations by Califano, *et. al*, showed that excitons, biexcitons, and trions have different radiative lifetimes.[21] In Section 4.4.4 we use these predictions to calculate expected B1 TRA amplitudes from each charge configuration using a Boltzmann distribution of initial state occupations for electrons, holes, and excitons. In contrast to prior assertions that B1 measures only the $1S_e$ occupation in CdSe QDs (in our framework either through $B1_x$ or $B1_e$),[124, 209, 207] our calculations indicate that the presence of *either* an electron or a hole in the QD core produces a strong B1 TRA signal at all temperatures from 10 K to 300 K with only a weak temperature dependence. Although predictions show the contribution of an exciton to B1 is greater than that of a hole or an electron, the predicted $B1_h$ signal from the hole is actually stronger than the $B1_e$ signal due to the electron at all temperatures calculated. These calculations confirm that a core-state hole can efficiently bleach the B1 transition at 10 K, validating our assignment of the long-lived B1 signal to $B1_h$.

Analysis of the fine structure within B1 further reinforces these conclusions. Figures 4.6a-d shows that the aggregate B1 feature redshifts with time in all samples, and the TRA spectra, particularly Figures 4.6e-g, show that this redshift actually corresponds to a redistribution of amplitude between two peaks within B1. We denote the lower (higher) energy peak $B1_h$ ($B1_x$), nomenclature validated by their temporal dynamics. Analysis using singular value decomposition, described in Section 4.4.2, identifies two distinct

temporal behaviors that account for the TRA maps for all but sub-picosecond time delays. A long-lived component is associated with the lower energy peak $B1_h$, and a short-lived contribution is associated with the upper energy peak $B1_x$ *as well as B2*. The spectra and time dependence of the long- and short-lived components are shown in Figures 4.6e-h and 4.6i-l, respectively. A third, sub-picosecond component described in Section 4.4.2 is associated with thermalization of hot carriers. These findings reveal that the temporal dynamics of B2 mirror not only the dynamics of TRPL but also $B1_x$(Figures 4.4e-h). Since B2 measures electron occupation, the accord between B2 and $B1_x$ indicates that the decay of $B1_x$ reflects the destruction of the $1S_{3/2h}1S_e$ exciton through electron trapping to the surface. Additionally, the agreement between $B1_x$ and TRPL indicates that $B1_x$ measures the population of *bright* excitons. In Figures 4.6i-l we summarize the temporal evolution of $B1_h$, $B1_x$, and B2, whose associated peaks are marked by triangles in Figures 4.6e-h. Since we have already established that the B1 component that out-lasts both TRPL and B2 is due to $1S_{3/2h}$ holes in the QD core, the remaining lower energy component of B1 is $B1_h$. We note that in this analysis $B1_x$ and $B1_h$ are separated by more than 30 meV in all four samples. Although relaxation of an exciton from the lowest energy bright exciton state into the optically forbidden dark state[48, 175] would redshift the B1 feature,[135] as discussed above the trapped electron evidenced by the B2 decay precludes this as an explanation for $B1_h$.

We use the established method of singular value decomposition (SVD)[155] to fit TRA maps. Details are provided in Section 4.4.2. The application of SVD to TRA spectra in particular has been discussed in a review by Ruckebusch, *et al.*[203] In brief, SVD finds a collection of spectra $Q_k(\lambda)$ and time decays $C_k(t)$ such that the observed TRA map is reproduced by $\sum_k C_k Q_k$. If there are only n distinct time behaviors in a data set, SVD will return significant values of Q_k for only the first n spectra. Thus, SVD is particularly good at identifying the number of independently evolving features in a TRA map.

In our case, SVD analysis shows three temporally distinct features. Moreover, the entire TRA map except the earliest, sub-picosecond delays can be described using only two components (Figure 4.8, Section 4.4.2). This is physically sensible since one expects carrier thermalization to appear as a distinct component on the sub-picosecond time scale. Thus, the first two principal components account for the dynamics that are the focus of this manuscript.

SVD analysis does not uniquely determine the components, allowing for orthogonal rotations that mix them,[155] so that linear combinations need to be chosen on physical grounds. The above isolation of the subpicosecond component pushes all of the relevant analysis into the first two components. For all possible linear combinations of these two, an upper energy pair of features occurs together, denoted $B1_x$ and B2 in Figure 4, indicating that these have identical time dependence. Moreover, for the linear combination in which $B1_x$ and B2 dominate one component, the remaining SVD component is dominated by a single, lower energy feature denoted $B1_h$ in Figures 4.6e-h. These linear combinations thus isolate the physics of the different subsystems with the least intermixing.

Given the expectation discussed earlier that exchange and annealing principally increase the density of hole traps, our finding that these treatments primarily increase electron trapping is surprising. One mitigating consideration is that, to the extent that Cd-S surface bonds may be viewed as assembling a CdS shell, hole trapping may be impeded by differences in bandgap and by the formation of a quasi-type-II band alignment, which further localizes the hole in samples sufficiently annealed to decompose SCN.[65, 115] We also note that cyclic voltammetry measurements of samples annealed at 250°C have shown that such annealing introduces mid-gap states close to both the conduction and valence band edges, and that the former may introduce electron traps in the SCN 200C sample.[28]

Additionally, increased coupling between QDs may introduce trapping pathways that do not arise in isolated QDs. For example, the increased interparticle coupling and greater

electrical conductivity previously demonstrated in these SCN exchanged samples[52] likely increases exciton and charge carrier diffusion to lower energy QDs.[62, 4, 190] Recent room temperature studies of QD solids demonstrated that excitons can become concentrated at low energy "hotspots," enabling multi-exciton phenomena when excitation densities surpass a rather low threshold of 10^{-3} excitons per quantum dot.[63] Under these conditions, which are met in this study, Auger processes can produce fast, radiationless recombination as well as hot carrier generation that enhances the likelihood of carrier trapping. Electron trapping would benefit more from the latter because kinetic relaxation is more facile for holes. Greater coupling, combined with spatial disorder in the degree of that coupling, can also explain the fast blueshift in TRPL observed in the SCN 200C sample (Figure 4.4d). By the arguments given above, PL transients from more highly coupled regions would decay more quickly. Since those regions would tend to have lower energy band-edge emission, once this contribution decays the remaining TRPL signal would shift to higher energies as observed.

4.3 Conclusion

Low temperature time-resolved optical measurements of these QD solids show progressively faster electron trapping to the QD surface upon ligand exchange and annealing. Combining time resolved absorption and photoluminescence, we find that holes within the QD, rather than electrons, are responsible for the bleach of the band-edge transition. Our finding that electron trapping is dominant at low temperature comes as a surprise given what is known about the surface treatment in these QDs. Although we argue that enhanced interparticle electronic coupling may increase electron trapping through multiexciton phenomena, additional study is needed to understand the interplay between electron and hole traps in this system. We further recommend additional studies to resolve the conflicting

interpretations of B1 here and in the literature.

4.4 Methods

TRPL measurements were acquired using the the off-axis gating method described in Section 3.3 and Figure 3.2.

Cadmium selenide QDs passivated with aliphatic ligands are prepared by the method described by Qu and Peng and processed as previously described by Fafarman, *et al.*[194, 52] The native ligands are solution exchanged with SCN, and samples are then spin-cast onto 0.5 mm thick UV Fused Silica substrates (MTI Corporation) and, wherever indicated, annealed under nitrogen on a hot plate for 5 min to increase electronic coupling among QDs. Extensive characterization of films resulting from this process is reported in Ref. 27. Sample substrates are cleaved and mounted in an optical cryostat (Oxford Microstat-HE) under a majority argon atmosphere that is immediately evacuated. Sample substrates are prepared as described in Section 4.4.3.

TRPL is performed with the off-axis gating configuration (described in Section 3.3 and shown in Figure 3.2) that permits broadband study of short delay times without determining *a priori* the wavelength range of interest. TRA measurements are acquired as described in Section 3.4. Briefly, in TRPL and TRA the samples are excited using the 400 nm doubled output of a 1 kHz, 120 fs regenerative amplifier with an approximately 350 μm diameter spot size with 15 μW time-averaged power. For TRPL, the 800 nm fundamental beam is used to create an optical Kerr gate (OKG).[220, 9] For TRA, the fundamental beam is sampled to generate a white light supercontinuum. The chirp of the white light supercontinuum probe is calibrated with the OKG (Section 3.4.1). Instrument response times for the TRPL and TRA experiments are approximately 500 fs and 120 fs as configured. Spectral resolution as configured is 10 nm for absorption measurements and 13 nm for photoluminescence

measurements. Less than 0.1 photons are absorbed per QD per pulse.[97, 141] Kerr gate background fluorescence reduction using the 450 nm to 460 nm spectral range was applied as described in Section 3.3.6.

Singular value decomposition analysis of TRA spectra is described in Section 4.4.2 below. This analysis yields the temporal decays of $B1_h$, $B1_x$, and B2 shown in Figures 4.4 and 4. The aggregate B1 bleach signal, denoted simply 'B1', is computed by integrating the B1 bleach over its bandwidth (1.9 to 2.3 eV).

4.4.1 Reproducibility of TRA Scans

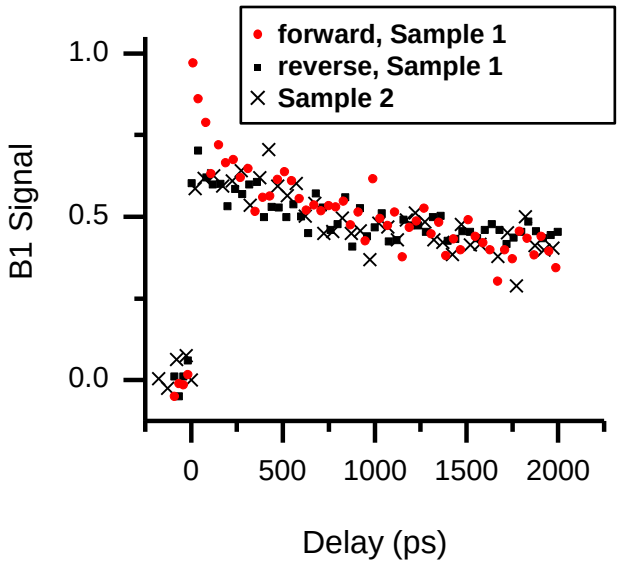

Figure 4.7: B1 bleach of CdSe with SCN Sample 1 at 10 K near beginning (reverse, black square) and end (forward, red square) of an experimental run. B1 bleach recorded previously on SCN Sample 2 is shown with black ×'s. All scans are taken at the same power level as those used in the main text. Decay traces are scaled to match at long times.

To make sure our TRA data are reproducible, and to alert us to any degradation so that we may lower pump power as necessary, the following scans are collected: (1) a reverse sweep from 2 ns to -100 ps; (2) a sweep forward over short delays from -5 ps to 10 ps; (3) a

forward sweep from -100 ps to 2 ns. Short time sweeps are deliberately nested between the lengthy, long time scans so that the latter can provide an upper limit on sample changes during the former. Figure 4.7 shows the reproducibility of these diagnostic long time scans for SCN. Additionally, *TRA measurements are also taken on a set of distinct but identically prepared samples to ensure reproducibility of the dynamics we report here*. Figure 4.7 also shows a TRA measurement on a different SCN sample ("Sample 2") prepared months apart but under identical conditions. One can see that reproducibility among these scans is good to within the noise of the measurement.

4.4.2 Singular Value Decomposition

We use the established method of principle factor analysis to fit TRA maps using singular value decomposition.[155] In general, we seek to decompose a broadband sequence of spectra into physically motivated independent spectral traces and spectral profiles as

$$D(\lambda,t) = \sum_k C_k(t) Q_k(\lambda) \tag{4.1}$$

where $D(\lambda,t)$ is the signal at delay time t and wavelength λ, $C_k(t)$ is the temporal profile of the kth physical component at t, and $Q_k(\lambda)$ is the temporally invariant spectrum of the kth component. In matrix notation,

$$D = CQ^T \tag{4.2}$$

As described in a review by Ruckebusch, *et al.*,[203] this decomposition can be determined either through model-free or physically-motivated methods. One model-free method for determining the total number of independent components using singular value decomposition (SVD):

$$D = USV^T \tag{4.3}$$

where U and V are orthonormal matrices with dimension $m \times n$ and $n \times n$ respectively for m delay points and n wavelengths. The $n \times n$ matrix S is diagonal and contains the singular values which describe the relative weight of the column vectors v_k that compose V.

We apply this global analysis procedure to our binned TRA data in LabVIEW. It is important to note that application of this method assumes that all components are separable and lack spectral migration throughout the measurement

The resultant time traces in the columns of U are not yet physical. We find that the residuals of the TRA maps are very small after subtraction of only three components, suggesting three physical mechanisms underpinning the TRA traces we observe.

To extract physically meaningful information from the SVD analysis, we apply several constraints to these components and perform rotations of the orthogonal vectors in V to determine the physical components $C_{1,2,3}$ and $Q_{1,2,3}$. A similar method was described in Ref [234].

All time traces must be positive definite to represent populations. Simultaneous sign flips on time traces and spectral vectors are permitted without changing the resultant modeled TRA signal. In three dimensions,

$$R_x(\theta) = \begin{pmatrix} 1 & 0 & 0 \\ 0 & \cos(\theta) & -\sin(\theta) \\ 0 & \sin(\theta) & \cos(\theta) \end{pmatrix} \tag{4.4}$$

$$R_y(\theta) = \begin{pmatrix} \cos(\theta) & 0 & \sin(\theta) \\ 0 & 1 & 0 \\ -\sin(\theta) & 0 & \cos(\theta) \end{pmatrix} \tag{4.5}$$

$$R_z(\theta) = \begin{pmatrix} \cos(\theta) & -\sin(\theta) & 0 \\ \sin(\theta) & \cos(\theta) & 0 \\ 0 & 0 & 1 \end{pmatrix} \tag{4.6}$$

We can perform arbitrary rotations among the first three components of U and S by application of these three rotation matrices:

$$D = \underbrace{USR}_{U'}\underbrace{R^T V^T}_{V'^T} \tag{4.7}$$

$$R = \begin{pmatrix} R'(\theta_1, \theta_2\theta_3) & 0 \\ 0 & I_{n-3} \end{pmatrix} \tag{4.8}$$

where I_{n-3} is the $(n-3) \times (n-3)$ identity matrix and

$$R'(\theta_1, \theta_2, \theta_3) = R_z(\theta_1)R_x(\theta_2)R_y(\theta_3). \tag{4.9}$$

is the combined rotation matrix for three separate rotations.

We first adjust θ_2 and θ_3 so that the residuals for long times are minimized. The

contributions D_k from each component of V' are calculated as

$$D_k = U' J^{k,k} V'^T \tag{4.10}$$

where $J^{k,k}$ is the single entry $n \times n$ matrix with $j_{k,k} = 1$ and all other elements 0. When acting on the left or right sides of a matrix $J^{k,k}$ selects rows and columns, respectively, giving us

$$C_k = U' J^{k,k} \tag{4.11}$$

$$Q_k = J^{k,k} V'^T \tag{4.12}$$

This selects the contributions to D from the selected j components of the rotated matrix V'. We then adjust θ_1 such that D_1 decreases to 0 at long times, equivalent to requiring that Q_1 represents the average of scans at long times.

This results in a component Q_3 that accounts for dynamics at very short times in TOPO, SCN, and SCN 100C. The short time dynamics in SCN 200C result in vectors Q_1 and Q_2 that account for nearly all dynamics without Q_3. In Figure 4.8a we show the residuals after subtraction of the first two SVD components which are calculated as

$$Error = TRA - \sum_{k=1,2} U' J^{k,k} V'^T \tag{4.13}$$

$$= TRA - \sum_{k=1,2} C_k(t) Q_k(\lambda) \tag{4.14}$$

after subtraction of temporally scaled components Q_1 and Q_2. In Figures 4.8b,c we show vector Q_3 for all samples and the time decay profile C_3. As previously stated, the temporal profile of SCN 200C appears as noise in this analysis.

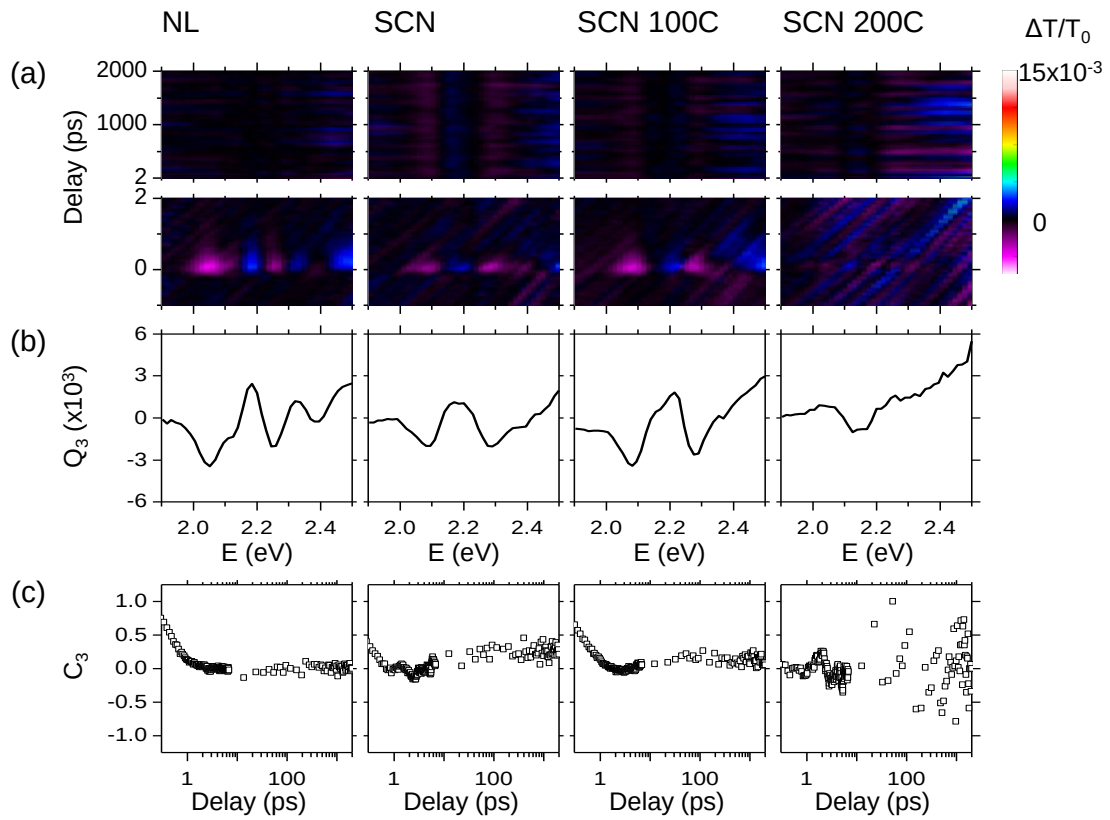

Figure 4.8: (a) Residual signal after subtraction of only the first two SVD components, defined as $[\text{Data} - (C_1Q_1 + C_2Q_2)]$. (b) Spectrum Q_3 and (c) time decay C_3 of the third SVD component. Samples are as labeled in each column.

4.4.3 Substrate preparation

Substrates were pre-scored using the full output of the Spectra-Physics Spitfire. The beam was focused using a 50 mm BK7 lens onto the 0.5 mm fused silica substrates. Cutting beam is pulsed using the SDG to enable and disable after the substrates have been translated to the desired position.

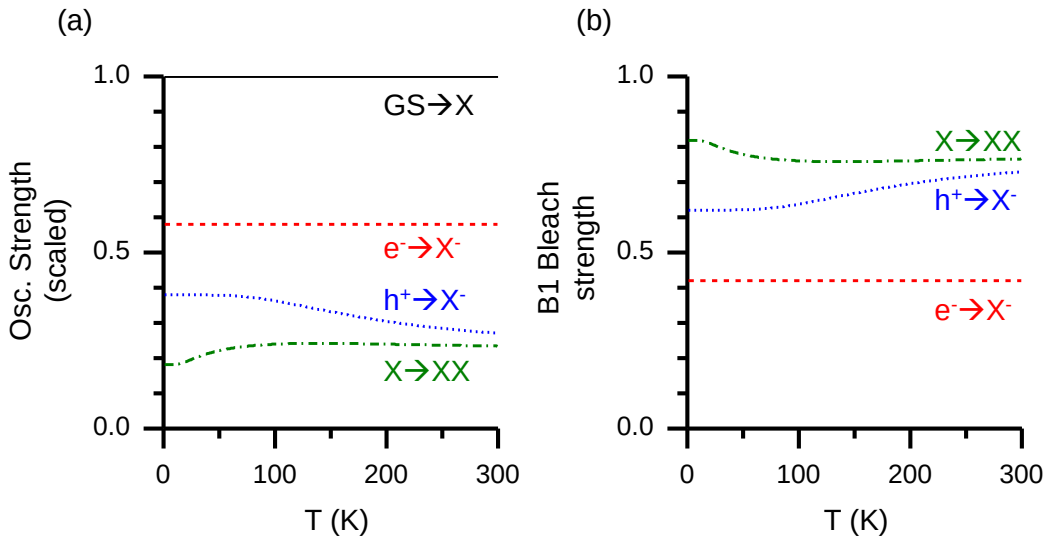

Figure 4.9: Calculations of electron and hole contributions to time-resolved absorption signals. (a) Scaled absorption transition oscillator strength vs. temperature, T. Ground state $|GS\rangle \rightarrow$ single exciton $|X\rangle$ (black, solid line), electron $|e^{-}\rangle \rightarrow |X^{-}\rangle$ (red, dashed line), $|h^{+}\rangle \rightarrow |X^{+}\rangle$ (blue, dotted line), $|X\rangle \rightarrow |XX\rangle$ (green dash-dot). (b) Calculated bleach of the B1 $1S_{3/2h}1S_e$ transition due to different carrier configurations.

4.4.4 Calculations of Electron and Hole Contributions to TRA

At room temperature, the B1 ($1S_{3/2h}1S_e$) transition is conventionally associated with occupation of the $1S_e$ state only. Here, we use calculated transition strengths from Califano, *et. al*, 21, to show that the relative importance of hole and electron occupation in the $1S_{3/2h}1S_e$ state varies with temperature. We use Figures 1 and 4 of Ref. 21 to extract the transition oscillator strengths, initial state relative energies, and thermal occupations of all initial states.

Transition oscillator strengths f_{ij} for transitions from lower state i to upper state j are calculated as

$$f_{ij} = \frac{n_i n_j}{\tau_{ij}} \tag{4.15}$$

where n_i and n_j are the degeneracies listed in Figure 1 of Califano et. al. This calculation

assumes that degeneracies multiply with no forbidden pathways. For example, $e^1h^0 \rightarrow e_1^2h_1^1$ has a degeneracy of $n = (n_i = 2) \times (n_j = 2) = 4$.

We calculate the total transition strength F for each charge configuration as follows:

$$F = \sum_{i,j} f_{ij} \frac{e^{-\beta E_i}}{Z} \tag{4.16}$$

$$Z = \sum_i e^{-\beta E_i} \tag{4.17}$$

$$\beta \equiv \frac{1}{k_B T} \tag{4.18}$$

where E_i is defined relative to lowest energy initial state of each charge configuration extracted from transition energies provided in Figure 4.6 of Califano et al, Z is the partition function, k_B is the Boltzmann constant, and T is temperature. In Figure 4.9a we plot these strengths F relative to the absorption strength of the original ground state $|GS\rangle \rightarrow$ exciton $|X\rangle$ transition strength. This shows that the $|GS\rangle \rightarrow |X\rangle$ and electron $|e^-\rangle \rightarrow$ negative trion $|X^-\rangle$ transitions are temperature independent, while the hole $|h^+\rangle \rightarrow$ positive trion $|X^+\rangle$ and $|X\rangle \rightarrow$ biexciton $|XX\rangle$ transitions are weakly temperature dependent, with the positive trion transition becoming weaker with higher temperature and the biexciton state becoming stronger. In Figure 4.9b we show the corresponding predicted bleach at the $1S_{3/2h}1S_e$ transition due to the presence of an electron, hole, or exciton in the core of the QD, showing that the presence of either charge carrier can substantially bleach the $1S_{3/2h}1S_e$ transition.

Chapter 5

Plasmonic Enhancement of Radiative Lifetimes in CdS Nanowires

5.1 Introduction

In the previous Chapter, we discussed how interactions between the quantum dot core and surface can modify the electron trapping rate in CdSe quantum dots under varied surface treatments. In this chapter, we investigate another way that tunable interactions between excitons and an external system can modify decay kinetics. Here we will study the radiative relaxation of cadmium sulfide nanowires both in the absence and presence of concentric coatings of silica and silver. While the silica coating both passivates the CdS surface and electrically insulates the CdS core from conductive silver coating, the proximal interaction between the CdS core and Ag coating drastically changes the available relaxation pathways in the nanowire by coupling hot exciton emission with surface plasmon polaritons in the Ag at the metal-dielectric (silica) interface. In this Chapter we present evidence for hot-exciton

emission enabled by the presence of this resonant plasmonic whispering-gallery cavity. The sample development and time-integrated experimental work described in this chapter was largely performed by Chang-Hee Cho, Carlos Aspetti, and Sung-Wook Nam in the research group of Professor Ritesh Agarwal here at the University of Pennsylvania. Through our contribution of picosecond time-resolved photoluminescence measurements, we validated the predicted enhanced radiative rate of these plasmonic nanowires. The studies in this Chapter were published and described in greater depth in *Nature Materials*, 2011, **10**, pp 669-675.[26].

5.2 Observations

In this experiment, cadmium sulfide nanowires were grown via a vapor-liquid-solid (VLS) method as described in Ref. [231]. All measured nanowires had diameters greater than 40 nm, significantly larger than the 3 nm Bohr exciton radius in CdS,[49] so the electronic state is purely determined by the bulk properties of CdS without any excitonic confinement effects. Photoluminescence from the photonic nanowires as grown via VLS emerges as a single, broad peak around 2.53 eV, but the addition of a SiO_2 passivation layer (Figure 5.1a) permits observation of the individual *A* and *B* excitons in CdS as seen in Figure 5.2 (bottom, "photonic").

Upon addition of a layer of silver to the exterior of the nanowires (Figure 5.1b), additional sharp peaks appear in the photoluminescence spectrum as shown in blue in Figure 5.2 (top, "plasmonic"). These peaks are separated by the energy $\hbar\omega_{LO}$ associated with the longitudinal-optical (LO) phonon modes in CdS, and their presence hints at an ultrafast radiative rate because LO phonon relaxation typically occurs on picosecond timescales.[246]

Measurements of PL at different laser excitation energies showed that these LO phonon PL peaks shift with the energy of the excitation laser, bolstering the claim that this was hot

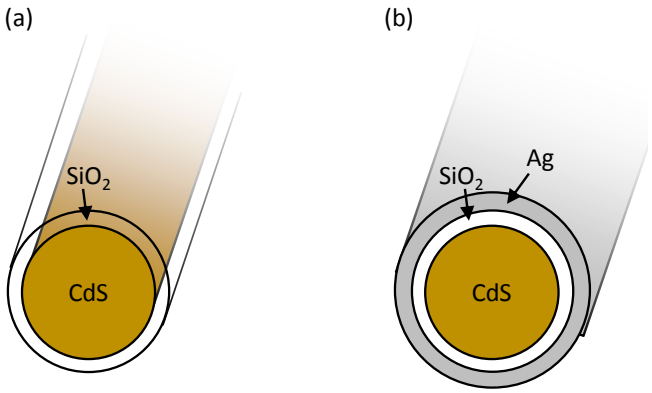

Figure 5.1: Schematic of (a) photonic nanowire and (b) plasmonic nanowire showing conformal SiO_2 and Ag coatings.

emission or resonant Raman scattering. A diagram of this hot emission is shown in Figure 5.3.

The separation of the peaks informs the source of these peaks. For Raman scattering, the phonon progression should occur with nearly identical separation between peaks because the phonons will have very small values of momentum $\vec{k}$. In contrast, a hot exciton phonon progression in the PL spectrum must satisfy momentum conservation with each emitted phonon determined by the intersection of the exciton dispersion and the phonon dispersion of CdS; to create a hot exciton, the system photon generates an LO phonon simultaneously with the exciton for momentum conservation.[181, 188] Although measurements of the 1LO phonon peak position were not available, the presence or absence of this peak would also indicate whether emission is from resonant Raman scattering (present) or hot-exciton emission (absent). Resonant Raman scattering was dismissed because the polarization of the phonon lines matched the polarization of the relaxed exciton, as expected for hot exciton emission.

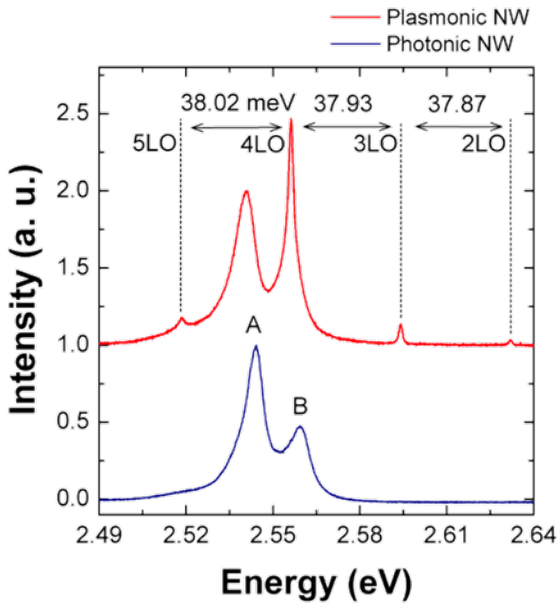

Figure 5.2: Comparison of photoluminescence of photonic nanowire (bottom, blue) and plasmonic nanowire (top, red). Originally published in Ref. 26.

5.3 Plasmonic Enhancement

Time-resolved photoluminescence measurements provided an opportunity to verify that the silver coating enhanced the radiative rate of these nanowires. Using the optical Kerr gate apparatus described in Chapter 3, we measured the time-resolved photoluminescence from ensembles of photonic and plasmonic nanowires.

A significant shortening of the lifetime of the excited state, from 1,600 ps for photonic nanowires to 7 ps for the plasmonic nanowires, was directly shown by these time-resolved photoluminescence measurements (Figure 5.4). The configuration of this experiment measured an ensemble of 300-500 nanowires with an average CdS core diameter of 140 ± 50 nm at room temperature. This shortening of the lifetime of the excited state for the plasmonic system suggest that the change in the dynamics of the excited state is due to the silver coating on the nanowires.

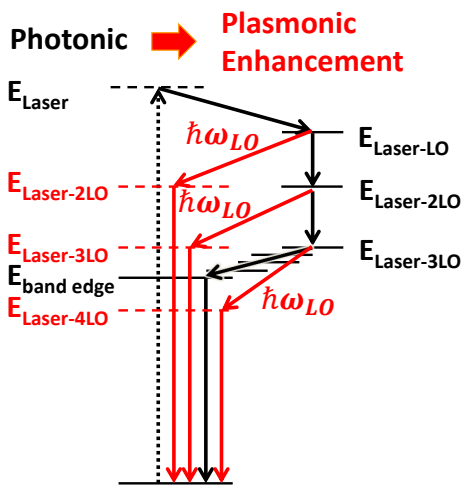

Figure 5.3: Schematic for exciton decay in plasmonic and photonic CdS nanowires.

5.4 Purcell Effect

The physical mechanism underlying this enhancement in radiative rate can be better understood by considering the impact of the Purcell effect on the silver-coated nanowires. In general, a resonant cavity can enhance the radiative rate of an emitter through the Purcell effect. This effect was first described by Edward M. Purcell in a single paragraph in the Physical Review,[193] and it reflects the resonant enhancement of an emitter due to the coupling of a cavity to the electromagnetic vacuum fluctuations in the vacuum.[68] The expected enhancement due to this effect is as follows:

$$\frac{\Gamma_{Purcell}}{\Gamma_0} = \frac{3Q}{4\pi^2}\frac{\lambda^3}{V_{eff}} \tag{5.1}$$

with Q the quality factor of the cavity, V_{eff} the effective mode volume of the cavity, λ the wavelength of the emission in the medium, Γ_0 the spontaneous emission rate of a system, and $\Gamma_{Purcell}$ the radiative rate when an emitter is in resonance with a mode of a surrounding cavity.[193] This enhancement thereby increases as the effective volume of the

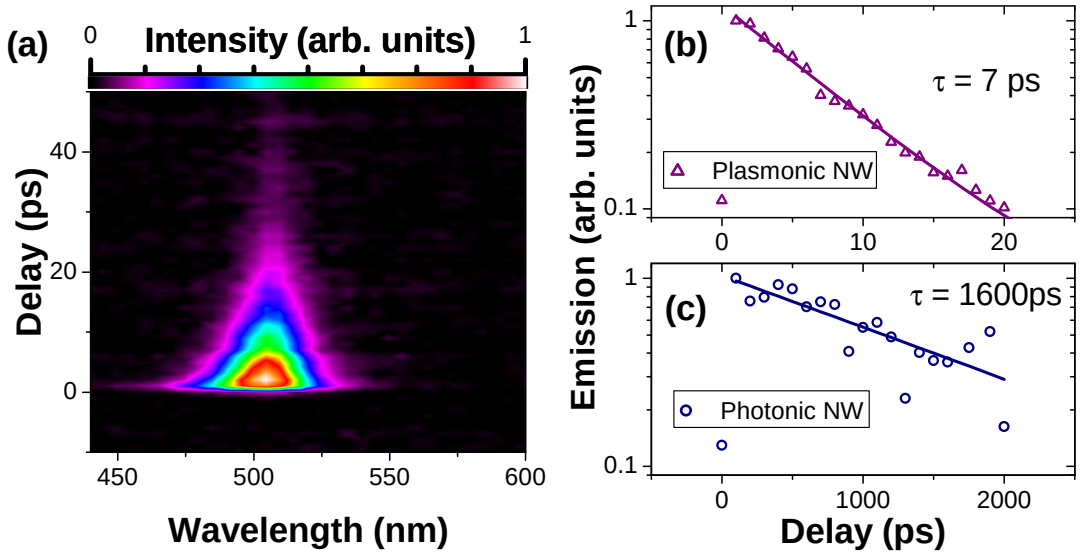

Figure 5.4: (a)Time-resolved photoluminescence spectral map from an ensemble of 300-500 plasmonic nanowires (average CdS core diameter, 140 - 50 nm) at 300 K. Time-resolved integrated emission intensity for plasmonic (b) and photonic (c) nanowires. Solid lines indicate dominant exponential decay lifetimes of 7 ps and 1,600 ps, respectively. Originally published in Ref. 26.

cavity decreases and as the quality factor of the cavity increases.

Purcell originally described this effect in the context of nuclear magnetic moment transitions at radio frequencies for which he calculated a transition rate enhancement of 5×10^{14} in the presence of small metallic particles.[193] Among other systems,[68], it has also been observed in photonic cavity systems, where it enhanced the radiative rate from quantum dots when on-resonance with the cavity and decrease the rate when off-resonance.[176]

Photoluminescence measurements of nanowires with varied CdS diameters demonstrate tuning of this plasmonic enhancement of PL (Figure 5.5a). By tuning the laser excitation to $E_B + 4\omega_{LO}$, three resonance peaks are found at nanowire diameters of 60 nm, 100 nm, and 135 nm. Finite difference time domain (FDTD) calculations, also performed by the Agarwal group, showed that the plasmonic coating creates whispering gallery mode resonant

cavities as shown in Figure 5.5c-e for $m = 2, 3, 4$, respectively. These diameter-dependent measurements and calculations show that the nanowire diameter tunes the resonance and that this radiative rate enhancement is due to the Purcell effet.

5.5 Methods

Time-resolved photoluminescence measurements were acquired using the optical Kerr gate effect as described in Section 3.3. The 800 nm output of a 1 kHz regenerative amplifier (Spectra-Physics Spitfire) was doubled to 400 nm in a β-barium borate crystal and used to excite the sample with a spot size of 75 µm, as estimated from the full-width at half-maximum, with average power densities below 0.4 $\mathrm{W\,cm^{-2}}$. The Kerr medium in this experiment was a 0.76 mm thick Suprasil II plate from Meller Optics. The optical Kerr gate was configured in the on-axis geometry shown in Figure 3.3 with a time-resolution of 240 fs. We built an o-ring-sealed, room-temperature sample holder to preserve the samples in an argon environment and prevent oxidation of the silver coating on the plasmonic nanowires during measurements.

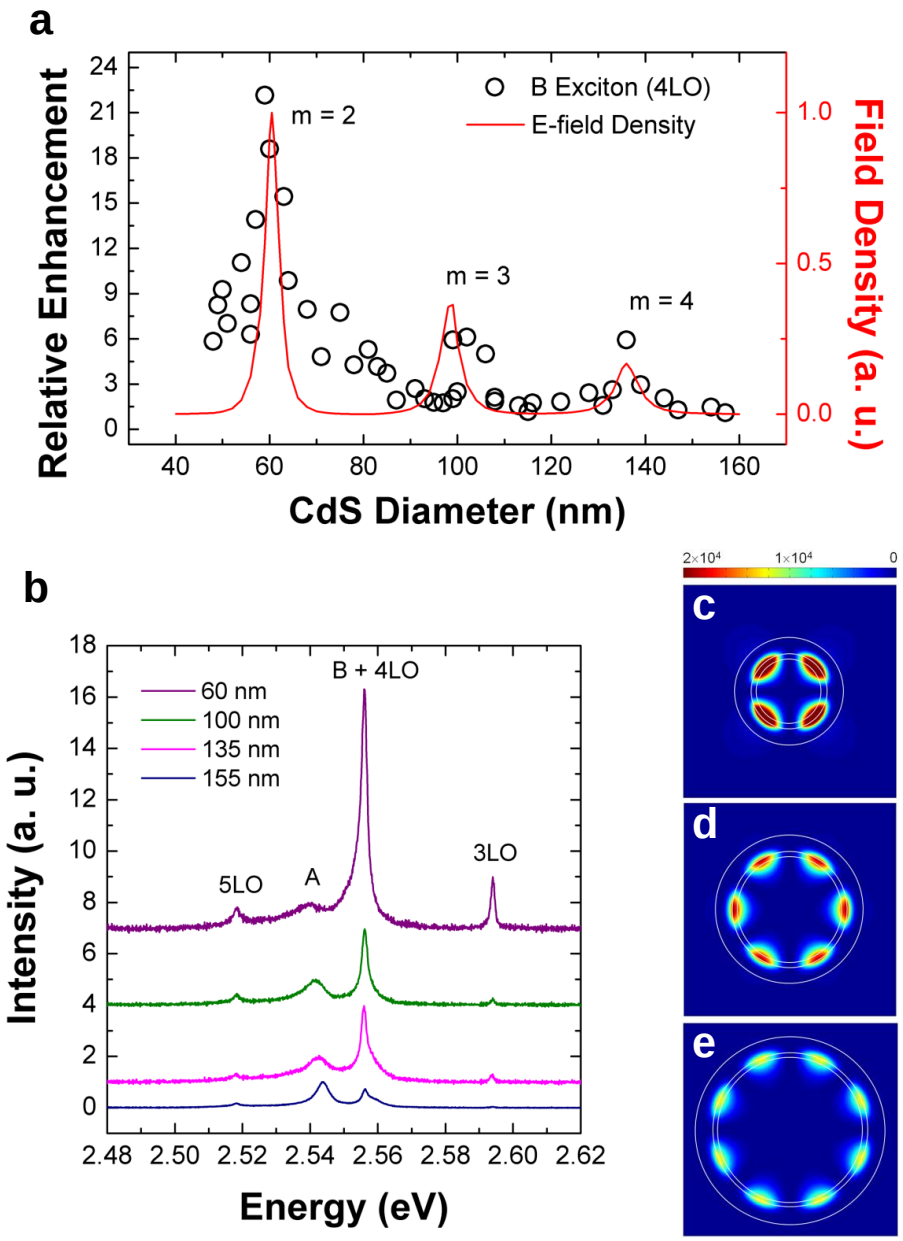

Figure 5.5: Size-dependent properties of the whispering-gallery plasmon nanocavity. (a), Relative enhancement of the 4LO hot-exciton transition vs. CdS nanowire diameter. (b) Photoluminescence spectra for four representative plasmonic nanowires. All the spectra are normalized to their free A-exciton intensity. (c-e) Calculated magnetic field intensities for the resonant cases at the 4LO energy of 2.556 eV, showing the whispering-gallery plasmon cavity modes for CdS nanowire diameters 60 nm, 100 nm and 135 nm with azimuthal mode number m of 2, 3 and 4, respectively. Originally published in Ref. 26.

Chapter 6

Electronic Transport

6.1 Introduction

In Chapter 5 we investigated how a conductive silver coating modified the decay kinetics of excitons in plasmonically enhanced CdS nanowires. In this Chapter and in Chapter 7 we will again study the motion of electrons, but we will primarily focus on disordered transport instead of metallic transport as was necessary in the previous Chapter. We are motivated in this study by further advancements of the chemical processes applied to the nanocrystal films that we studied optically in Chapter 4 and the subsequent construction of high-mobility, air-stable quantum dot field effect transistors. We will show in Chapter 7 that these transistors provide an opportunity to investigate how the inter-dot coupling varies as the Fermi energy is tunably controlled. As necessary for that analysis, here we briefly discuss prior results regarding electrical transport in disordered systems and the nature of the transition from an insulating state to a metallic state. Excellent reviews

of this topic are provided by Mott, Shklovskii, and Efros, Lee and Ramakrishnan,[166, 214, 144] and the models discussed below have been shown applicable to many different physical systems including amorphous carbon and graphene oxide flakes,[72, 199] organic semiconductors,[17] and both amorphous and crystalline inorganic semiconductors.[166]

We start this discussion with a simple definition of metals and insulators as adapted from Ref. 166 : a sample in which no activation energy is required to transport electrons is said to be metallic, whereas a sample in which the Fermi energy lies below the conduction band is termed insulating. We note an important implication of this definition which is sometimes misunderstood: at zero temperature, the defining characteristic of a a metal is a *finite* conductivity, not necessarily an *increasing* conductivity. This empirical definition of "metals" and "insulators" depends only on the temperature dependence of the resistance R rather than the chemical composition of the material which may or may not strictly be metallic. In a metal, the Fermi energy ε_F is greater than the mobility edge and conduction occurs without the need for activation.

6.2 Mott and Anderson Localization

Sir Nevill Mott considered the effect of varying the spatial separation between host sites and found that decreasing this separation can cause a transition to a metallic state.[167] This configuration prevents constructive interference on a large scale from building up among many lattice sites and results in an activation barrier between carriers at the ε_F and conductive states above ε_C.

P. W. Anderson similarly considered the impact of disorder on a regularly spaced lattice of carrier sites. Since its introduction, this model of disorder-induced localization has been shown applicable to many different physical systems as described in Chapter 1, including acoustic waves, light transmission, and photonic bandgap systems. We can see the impact

of this localization phenomenon in the case of electronic transport in the tight-binding approximation. In the presence of a series of regular site potentials V the wavefunctions Ψ are given by

$$\Psi(\vec{r}) = \sum_n \exp(i\vec{k} \cdot a_n)\Psi_n(|\vec{r} - \vec{a_n}|) \tag{6.1}$$

where $\vec{k}$ is the wavevector, a_n is the position of the nth site, and r is the position.

For a system with identical potentials at each site, conductive, delocalized states lie in a band of energy width $B = 2zI$ about V that is defined in terms of the overlap integral between two neighboring sites which quantifies the interaction of neighboring sites I and the coordination number z describing the number of neighboring atoms:

$$I = \int \Psi(|\vec{r} - \vec{a}_n|)H\Psi(|\vec{r} - \vec{a}_{n+1}|)\,\mathrm{d}^3x \tag{6.2}$$

Anderson considered random variations to this potential where the potential energy of each site is randomly uniformly distributed about V from $V - \frac{V_0}{2}$ to $V + \frac{V_0}{2}$.[5] He found that a critical value of V_0 exists above which free diffusion of carriers is impossible. In that case, the wavefunctions are localized with an exponential decay profile away from some central point:[167]

$$\Psi = \exp(-r/\xi)\sum_n c_n \exp(i\phi_n)\Psi_n(\vec{r} - \vec{a}_n) \tag{6.3}$$

For sufficiently high carrier energy, conduction again becomes possible. This energetic threshold is termed the "mobility edge" ε_C. For carriers with energy ε below ε_C wavefunctions are localized, whereas more energetic carriers may be delocalized. Therefore, if ε_F can be raised above ε_C, a metal-insulator transition may be achieved as carriers can access extended, conductive states.

6.3 Insulating Transport Regimes

As we will discuss next, at lower temperatures, the interplay of the wavefunction decay in electron tunneling to neighboring sites, the density of available states, and the probability of thermal activation to the conduction band result in several different regimes of transport.

Although there is some overlap, we can in general classify a transport regime based on the temperature dependence of conductivity. All hopping conduction models can be written as:

$$\sigma = \sigma_0 \exp\left(\left(-\frac{T_0}{T}\right)^p\right) \tag{6.4}$$

with conductivities σ, σ_0, sample temperature T, and characteristic temperature T_0. We can therefore use the exponent p to describe the temperature dependence of the electrical transport.

6.3.1 Activation to a Mobility Edge

At sufficiently high temperatures, thermal fluctuations in the randomly acquired energy of charge carriers are sufficient to reach the mobility edge, and the conductivity σ scales as [166]

$$\sigma = \sigma_0 \exp\left(-\frac{\Delta\varepsilon}{k_B T}\right) \tag{6.5}$$

with

$$\Delta\varepsilon \equiv \varepsilon_0 - \varepsilon_F. \tag{6.6}$$

The carriers then diffuse until losses from inelastic scattering drop their energy below the mobility edge. In this case, $p = 1$.

6.3.2 Nearest Neighbor Hopping

In this situation, an electron absorbs sufficient energy from phonons to surmount the potential barrier to the nearest neighbor site. This conduction model is also characterized by $p = 1$ and is described as "activated:"

$$\sigma = \sigma_3 \exp\left(-\frac{\varepsilon_3}{k_B T}\right) \tag{6.7}$$

and ε_3 is related to the density of states as $\varepsilon_3 \sim 1/N(\varepsilon_F)a^d$ in d dimensions.[166, 159]

6.3.3 Variable Range Hopping

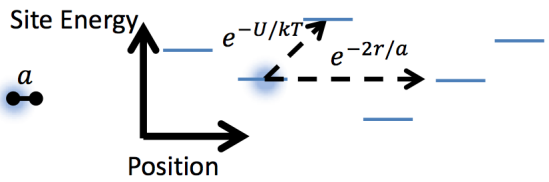

Figure 6.1: Schematic for energetic cost of tunneling as described in text.

Miller and Abrahams [159] considered the question of hopping among sites below the mobility edge and found that the rate Γ of a particular (nearest neighbor) hop (proportional to the probability of that hop) varied as [166]

$$\Gamma \propto \nu_{ph} \exp\left(-\frac{2r}{\xi} - \frac{U}{k_B T}\right) \tag{6.8}$$

where ν_{ph} relates to the strength of interactions with phonons, r is the distance to the site, and U is the difference between final and initial energies (Figure 6.1). If hops are always to the nearest neighbor, this results in

$$\sigma \propto \exp\left(-\frac{U}{k_B T}\right). \tag{6.9}$$

Mott considered the question of hopping conductivity given a constant density of states ($N(\varepsilon)$. [166] Considering a hop to a distance R, a greater distance permits greater selection of possible states in resonance with the initial state:

$$N(V,E) \propto V_n r^n N(E) \tag{6.10}$$

$$U \sim \frac{1}{N(V,E)} \sim \frac{1}{V_n r^n N(E)} \tag{6.11}$$

where $N(V,E)$ is the number of states per (volume times energy), V_n is the volume of an n-ball in n-dimensions ($V_1 = 2$, $V_2 = \pi$, $V_3 = \frac{4}{3}\pi$). For a hop to a given site at distance r, the minimum energy difference between initial and final sites will decrease with that distance. The conductivity is found through judicious use of eq. (6.8).

By noting that the rate is exponentially dependent on the energy difference U, the temperature dependence can be determined by finding the optimal r.

$$\Gamma \propto v_{ph} \exp\left(-\frac{2r}{\xi} - \frac{U}{k_B T}\right) \tag{6.12}$$

$$\frac{d\Gamma}{dr} \propto \left(-\frac{2}{\xi} + \frac{n}{V_n r^{n+1} N(E) k_B T}\right)\Gamma \tag{6.13}$$

Setting $\frac{d\Gamma}{dr} = 0$, one finds

$$r = \left(\frac{n\xi}{2V_n N(E) k_B}\frac{1}{T}\right)^{1/(n+1)} \tag{6.14}$$

$$r = (\beta/T)^{1/(n+1)} \tag{6.15}$$

and therefore that

$$\Gamma \propto v_{ph} \exp\left(\left(\frac{1}{T^{1/(n+1)}}\right)(\text{const.})\right) \tag{6.16}$$

and we see that Γ and thereby R are both exponentially dependent on $T^{-1/(n+1)}$ in n dimensions, giving $p = 1/(d+1)$.

$$R(T) = R_0 \exp\left(T_0/T\right)^{\frac{1}{n+1}} \tag{6.17}$$

6.3.4 Coulomb Gap

So far in this Chapter, these models for transport have neglected the impacts of electron-electron interactions in transport. Efros and Shklovskii showed that multi-particle Coulomb interactions can decrease the density of states at the Fermi level ε_F, in effect producing a gap between filled and unfilled states.[44] With this consideration, they showed that a $p = 1/2$ temperature dependence could arise independent of the dimensionality of the system. This is sometimes also referred to as "Efros-Shklovskii variable range hopping."

6.4 Magnetoresistance

Magnetoresistance, defined numerically as $\Delta\rho/\rho_0 \equiv \frac{R(B)-R(B=0)}{R(B=0)}$, generally provides additional insight into transport mechanisms at low temperature. The application of a magnetic field can illuminate the transport properties in ways otherwise difficult to experimentally unravel.

The list of mechanisms that can produce positive and negative MR, even in nominally non-magnetic systems such as these, is extensive, and possibilities for positive and negative MR mechanisms have been enumerated in the works of Vavro,[233] Vora,[235],

di Vittorio,[39], and Fung.[61] Negative MR can arise from weak localization[13, 113] and Zeeman modulation of the mobility gap[60]. Positive MR can arise from wave-function shrinkage[214], electron spin blockade [39, 82], and classical disorder induced magnetoresistance[185]. Additionally, quantum corrections in the hopping regime can produce both positive and negative MR.[215, 174]

In systems with relatively little disorder, quantum interference effects can enhance the resistance of the sample at zero magnetic field. When magnetic field is applied, the electrons acquires a different phase by traversing a path in one direction versus the same path in the opposite direction as described by Bergmann. [13]

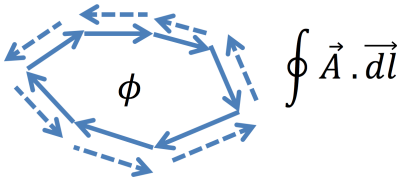

Figure 6.2: Schematic for weak localization path interference.

A magnetic field can also cause asymmetric shrinkage of the wavefunction, thereby decreasing the overlap with nearby hopping sites. This decreased overlap causes lower conductivity and thus positive magnetoresistance.[214],

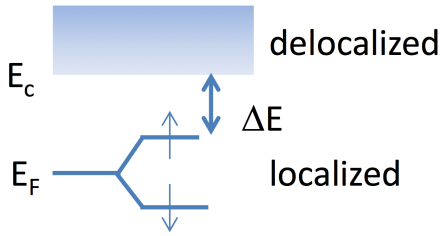

Figure 6.3: Zeeman splitting of spin states.

The presence of a magnetic field will induce Zeeman splitting of electronic states based on the spin. This splitting is schematically depicted in Figure 6.3, where states with one electron spin are raised closer to the mobility gap. Because the conductivity is exponentially

rather than linearly dependent, the presence of a magnetic field will induce an overall decrease in the sample resistance and therefore a negative magnetoresistance.

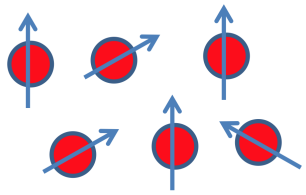

Figure 6.4: Schematic for exchange-coupling magnetoresistance.

Similarly, if there is a large exchange coupling between electrons on adjacent sites, a positive (saturating) magnetoresistance can occur as all spins line up with the applied field (Figure 6.4).[39, 82]

As shown by Parish and Littlewood, classic disorder at the macroscale in a material can lead to linear, positive magnetoresistance.[185, 186] Parish and Littlewood used a classical model of a disordered resistor network to justify the positive magnetoresistance observed in silver chalcogenide samples.[244, 143, 96]

6.5 Nanocrystal Transport and Electronic Devices

A recent review of electrical transport in QD films was provided by Guyot-Sionnest.[80]. As we discuss below, all of the insulating transport regimes listed in Section 6.3 have been previously observed in close-packed nanocrystal samples from $p = 1/4$ up to $p = 1$. Transport in quantum dot films has also been modeled theoretically, emphasizing the importance of charge doping, spatial separation, and spatial disorder on the observed conductivity in these films.[253, 25, 216, 247, 8] Electrical transport in quantum dot films has been investigated using electrical, electrochemical, and optical techniques.

6.5.1 Transport Regimes

Early studies observed activated transport ($p = 1$) in many examples of semiconductor QD films.[69] Looking at annealed PbSe QD films in a grounded back gate configuration shown in Figure 6.5a, Romero, *et al.*, found activated transport above 200 K and CG behavior at temperatures below 200 K.[202] Yu, *et al.*, observed activated transport in CdSe QDs thin films doped with potassium (above 100 K) and in electrolytically charged thin films (from 80 K to 200 K) similar to Figure 6.5c where the mobility was modulated as the $1S_e$ and $1P_e$ states were fillled electrochemically.[248] The electrolyte solution is used to modify the carrier concentration and the samples must be raised to above the electrolyte melting point order to modify this concentration.

Coulomb-gapped transport ($p = 1/2$, Section 6.3.4) has also been observed in quantum dot films. In a follow-up to Ref 248, the Guyot-Sionnest group observed a transition from activated transport at temperatures above 120 K to Coulomb-gapped variable range hopping at lower temperatures,[249] a transition expected to occur when sufficient thermal energy is available to make nearest neighbor hops most likely. Kang, *et al.*, also observed this transition in PbSe QD FETs, finding that the corresponding localization length scaled linearly and activation energies scaled inversely with the constituent nanocrystal diameters.[112]

Variable range hopping (Section 6.3.3) in three dimensions ($p = 1/4$) has also been observed in QD films. Talapin and Murray studied hydrazine-treated PbSe films in a FET configuration (7.1b) that could switch from n-type to p-type by vacuum or heat treatments, finding that low-temperature conductance scaled with $p = 1/4$.[221] In electrolytically gated CdSe QD films, Guyot-Sionnest's group observed both $p = 1/4$ at charging levels corresponding to full conduction band states ($n \sim 0$ and $n \sim 2$) at low temperature, with $p = 1/2$ at higher temperature and in all other charging levels.[145] Studying ZnO nanocrystal solids, Wang and Greenham also observed $p = 1/4$, but they attributed this transport to

surface or defect states rather than among core electron conduction band states in the nanocrystal core.[236]

Finally, a novel exponent of $p = 2/3$ has also been observed in ZnO[91] and gold nanoparticles.[252] For ZnO, Houtepen, *et al.*, attributed this exponent to thermal broadening of energy levels available for hopping transport and a modified effective transfer rate (Equation (6.8)) due to these energy fluctuations, leading to Gaussian broadening of the energy levels. By decreasing the length of linker molecules connecting Au nanoparticles, an insulator-to-metal transition was observed in the film previously demonstrating $p \approx 2/3$.[252]

We note that in experimental attempts to measure the temperature dependence of conductivity, it is key to control and understand any bias-dependent effects.[249] The electric field between electrodes can drastically modify the temperature dependence by creating a potential energy gradient across the sample. This shifts the likelihood of hopping against the field, and will create the appearance of greater conductivity than would appear with lower source-drain bias. Increasing the bias can in fact even give the appearance of a false voltage-induced metal insulator transition.[38, 192] However, controlled modification of this source-drain bias across the samples can also permit measurements of additional regimes of transport as shown by Yu, *et al.*, using electrolytically gated CdSe samples drop cast between interdigitated platinum electrodes.[249]

6.5.2 Applications

In the context of these different hopping regimes previously observed, it is timely to note the recent, fast advances in electron mobility, well summarized by Hetsch, *et al.*[86] Initial studies of electrical transport in quantum dot films demonstrated a remarkably low conductivity and mobility ($1 \times 10^{-4}\,\mathrm{cm^2\,V^{-1}\,s^{-1}}$).[69] Several years ago the development

of ligand exchange methods for short molecules caused significant mobility increases using hydroxide and thiocyanate.[111, 52] Further studies of the metal-chalcogenide complexes by the Talapin group and annealing of indium contacts in the Kagan group brought mobilities to record high levels of $27\,\mathrm{cm^2\,V^{-1}\,s^{-1}}$ and above. [27, 30] Additional efforts have also made progress with InAs,[146] PbS,[134] and PbSe;[182, 148] in this thesis we focus on the thiocyanate exchange of CdSe as developed in the Kagan group here at Penn.[52, 27, 182] A better understanding of the low temperature transport mechanisms may further inform the nature of electronic interactions in devices. As we will discuss in Chapter 7, the samples described in this dissertation are electronically gated in a transistor configuration (Figure 6.5b). In contrast with the electrolytic technique frequently used, the gate bias is free to change at low temperatures without reaching a physical melting point in the system.

In terms of applications, QD solids have been used to realize solar cells, photodetectors, light emitting devices, and transistors and circuits.[213, 137, 120, 134, 118] In all these examples, charge transport is important, and recent advances have led to high carrier mobilities in QD solids through a combination of strong coupling (*via* short ligands[142, 27, 223] and/or thermal annealing [142, 30, 27]) and doping to shift the Fermi level (by introducing impurities[27] or exploiting non-stoichiometry[182]). The high mobility in these samples has been discussed in the framework of an Anderson mobility edge,[5] ε_0, which lies above the Fermi level, ε_F, and separates low energy, localized states from higher energy, delocalized, bandlike states[27] (see Section 6.2). Both experiment and theory have suggested that such delocalized states may then be accessed through thermal [27] or optical[27, 211] excitation, the latter proceeding through an Auger process of QD ionization.[211]

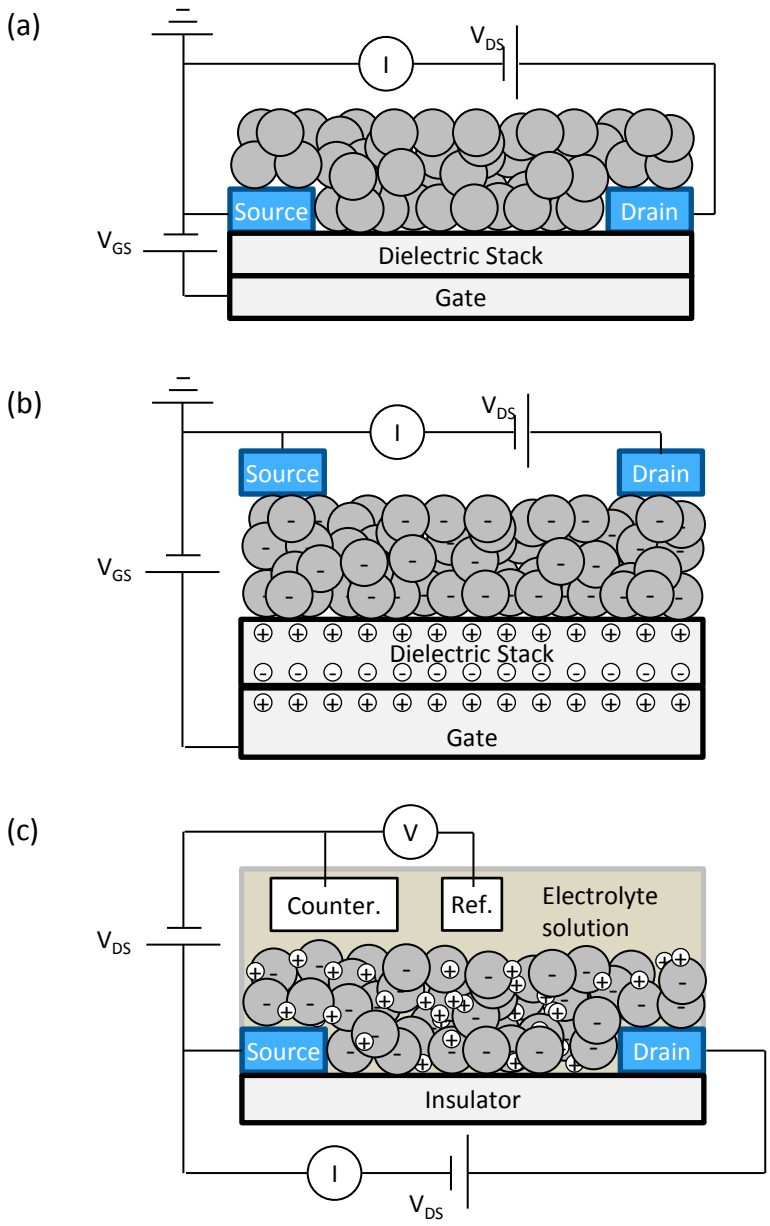

Figure 6.5: Quantum dot film transport measurement schematic. (a,b) Field effect transistor configurations. (c) Electrolytic gating configuration.

Chapter 7

Gate-Induced Carrier Delocalization in Quantum Dot Field Effect Transistors

7.1 Introduction

In the context of disordered electrical transport and previous measurements on nanocrystal solids as described in Chapter 6, we now describe efforts to study the onset and gate dependence of charge delocalization in recently developed high mobility QD field effect transistors (FETs) due to interactions among neighboring quantum dots. Both experiment and theory have suggested that such delocalized states may then be accessed through thermal [27] or optical[27, 211] excitation, the latter proceeding through an Auger process of QD ionization.[211]

The quantum dot transistors described in this chapter were fabricated using similar procedures to the QD films studied in Chapter 4 with several additional steps; details of fabrication and characterization were previously described in Refs. 27 and 28. Briefly, highly monodisperse, 4 nm diameter CdSe QDs capped with long-chain aliphatic ligands are synthesized, and these ligands are exchanged for compact SCN (thiocyanate) ligands, allowing dispersion in polar solvents. Thin films are prepared by spin-casting SCN-exchanged CdSe QDs dispersed in dimethylformamide (DMF) onto Al_2O_3 (20 nm) / SiO_2 (250 nm) / n^+-doped Si substrates, which serve as the dielectric stack (Al_2O_3/SiO_2) and back gate and support (Si) for the device. In/Au electrodes are then thermally deposited on the QD films to define a 40 μm channel length and a 600 μm channel width. Thermal annealing at 250 °C for 10 minutes promotes indium diffusion and doping and decomposes the SCN ligands, thereby further reducing QD separation.[27] A 40 nm thick layer of Al_2O_3 is evaporated *via* atomic layer deposition (ALD) to render the devices air stable.[147, 28] A schematic of these samples is shown in Figure 7.1. Devices prepared this way have typical room temperature field effect electron mobilities of $\sim$27 cm^2/Vs, and for the present study the characteristic room temperature mobility is 8-12 cm^2/Vs as demonstrated in Section 7.2 below.

After electrical connections are made, the sample is then transferred into the bore of a 9 Tesla Quantum Design Physical Property Measurement System for which magnetic field B is aligned with the sample normal. Temperature dependent resistance and magnetoresistance measurements are collected in a $\sim$ 5 Torr helium gas atmosphere. All electrical measurements are collected using a Keithley model 237 Source-Measure Unit to provide drain-source bias, V_{DS}, and a Keithley model 2410 Source-Measure Unit to provide gate bias, V_G, relative to the grounded source. Samples are thermally contacted using Apiezon N grease which also affixes samples to the Quantum Design sample puck. Electrical contacts to devices are made with gold wire (99.995%, Alfa Aesar, 0.05 mm diameter) soldered to

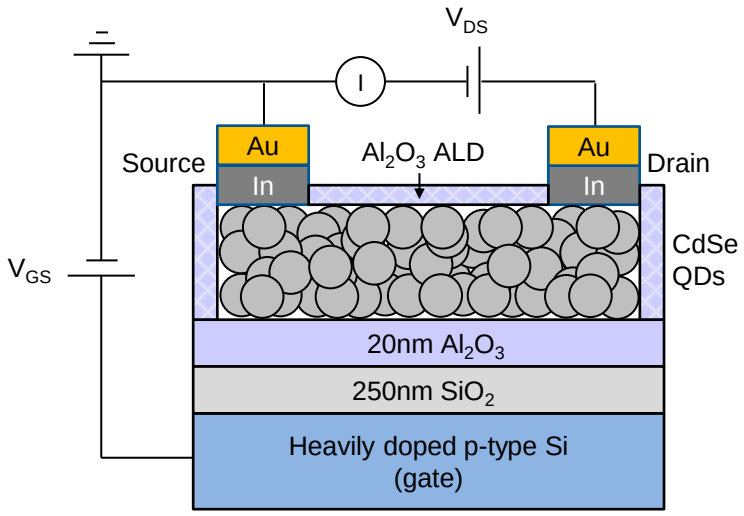

Figure 7.1: Quantum dot field effect transistor schematic.

the sample puck and contacted to the device using DuPont 4929N conductor paste.

The high mobility in these samples has been discussed in the framework of an Anderson mobility edge,[5] ε_0, which lies above the Fermi level, ε_F, and separates low energy, localized states from higher energy, delocalized, bandlike states[27] (see Section 6.2). By working in the low temperature limit (kT much less than the mobility gap $\Delta\varepsilon$), all states participating in conduction lie within the mobility gap and are thus non-extended. We are therefore able to use changes in variable range hopping (VRH)[166] to detect enhanced electron delocalization as the Fermi energy is increased, in accord with the presence of an Anderson mobility gap.[5] As we will describe below, under any reasonable assumptions for the dielectric constant of these quantum dot transistors, the electron localization length increases significantly beyond the particle diameter in response to a gate voltage. Magnetoresistance (MR) measurements reveal an MR component whose sign, magnitude, and temperature dependence agree with that implied by the Anderson model after the Zeeman spin energy is included within a VRH framework.

7.2 Room Temperature Characterization

Initial characterization of all samples is performed at room temperature prior to cooldown to verify electrical contacts and proper transistor behavior of samples. Room temperature I vs V_G curves used to calculate the sample mobility, μ, are shown in Figure 7.2. Mobility is calculated in the linear region using

$$I_{DS} = C_i \mu \frac{W}{L}(V_G - V_T)V_{DS} \tag{7.1}$$

where C_i is the capacitance per unit area, calculated to be 13.3 nF/cm^2 using $\kappa = 3.9$ for SiO_2 and $\kappa = 9$ for Al_2O_3[200], $W = 600$ μm is the channel width, $L = 40$ μm is the channel length, V_G is the gate bias, V_T is the threshold bias, and V_{DS}= 1 V is the drain-source bias used to collect the data in Figure 7.2.[90]

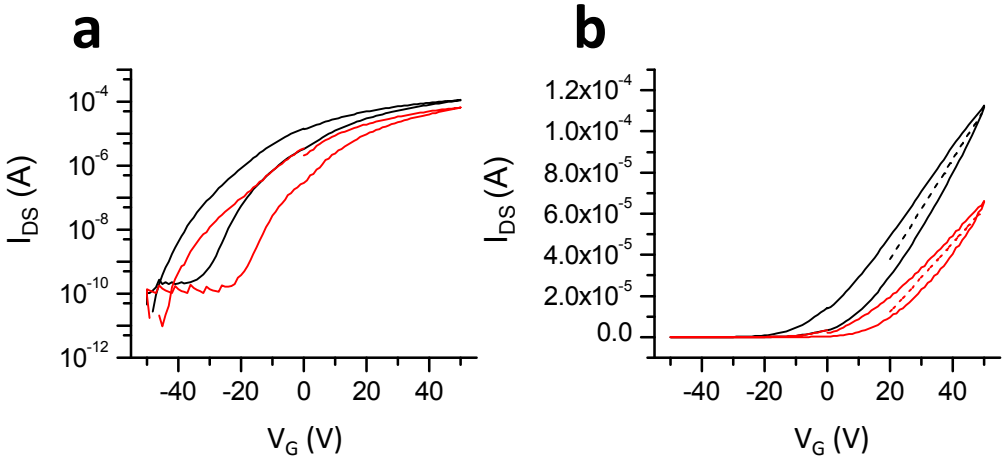

Figure 7.2: I_{DS} vs V_G with I_{DS} plotted (a) logarithmically and (b) linearly for two measurements taken at different times on our sample during the course of our study (black and red). Dashed lines are fits used to calculate mobilities of Measurement 1 (black, 12 cm^2/Vs) and Measurement 2 (red, 8 cm^2/Vs).

For all devices, we also measure I vs V_{DS} at varied V_G to observe saturation currents. A representative plot is shown in Figure 7.3. We note that during initial testing after a sample

has rested at room temperature for several days at V_G=0 V, the initial I vs V_{DS} curve at V_G=0 V was uncharacteristically resistive. After measuring I vs V_{DS} curves at V_G ranging from 10 V to 50 V, the conductance at V_G=0 V was significantly greater. We tentatively associate this with initial charging of the conductive channel, but this was not a primary direction of investigation.

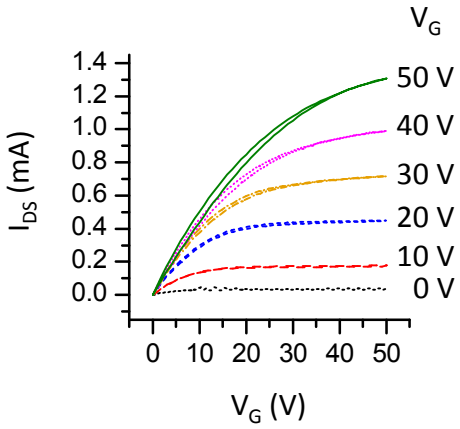

Figure 7.3: I_{DS} vs V_{DS} for QD FET for various V_G at room temperature.

7.3 Low-Temperature Measurements

At low temperatures, the devices demonstrate a temperature- and magnetic field-dependent resistance settling time when modifying V_G and, to a lesser extent, V_{DS}. An example of this effect is shown in Figure 7.4. In black and red we show the representative curves of the settling time of I_{DS} when changing the gate bias of two devices at 10 K and 64 K, respectively. Changing V_G at 10 K and 0 T (black) results in a slow settling time that clearly has not yet reached equilibrium after 250 s. These effects are mitigated by changing V_G and V_{DS} at or above 60 K (red) and pausing to settle the sample resistance prior to low

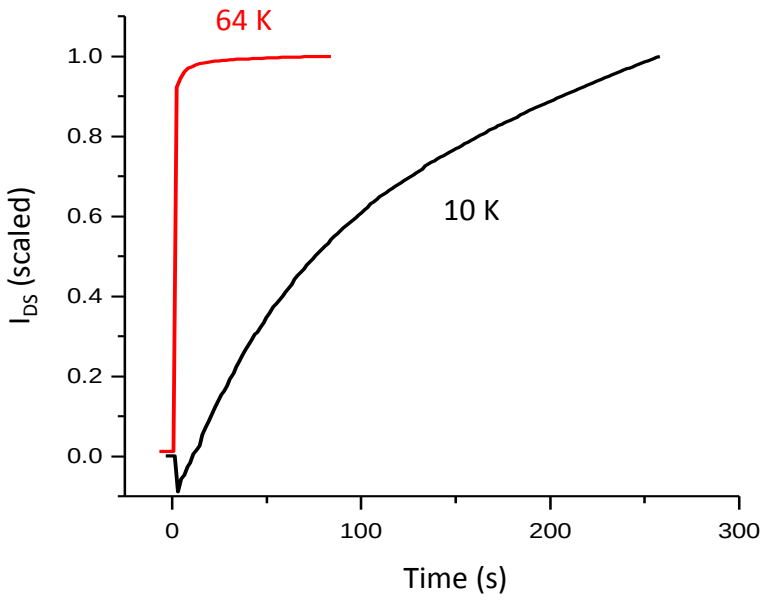

Figure 7.4: Temperature dependence of QD FET resistance settling after changes in V_G at 10 K (black) and 64 K (red), scaled by the maximum current recorded in each run.

temperature MR measurements, as shown by the red curve in Figure 7.4. We will further discuss the importance of setting V_G at high temperatures in Section 7.4.

Although we did not investigate this effect further, we also observed a magnetic field dependent settling time to the steady-state resistance of the sample when V_G was changed at low temperatures. Prior to these measurements, the gate bias was changed at 10 K to 50 V followed by adaptive changes to V_G between 30 V and 45 V in an attempt to quickly settle at a sample resistance with long term stability. We show in Figure 7.5 unexpected dynamics as the magnetic field is swept through zero field and note several interesting patterns in the resistance drift with time of the sample. At a field of 9 T, R increases with time, while at smaller B values, as shown by the downward drift at -3 T, the resistance decreases. This downward drift at constant field seems to produce artifacts in the magnetoresistance sweeps shown here; as the field sweeps through small magnitudes, the overall resistance

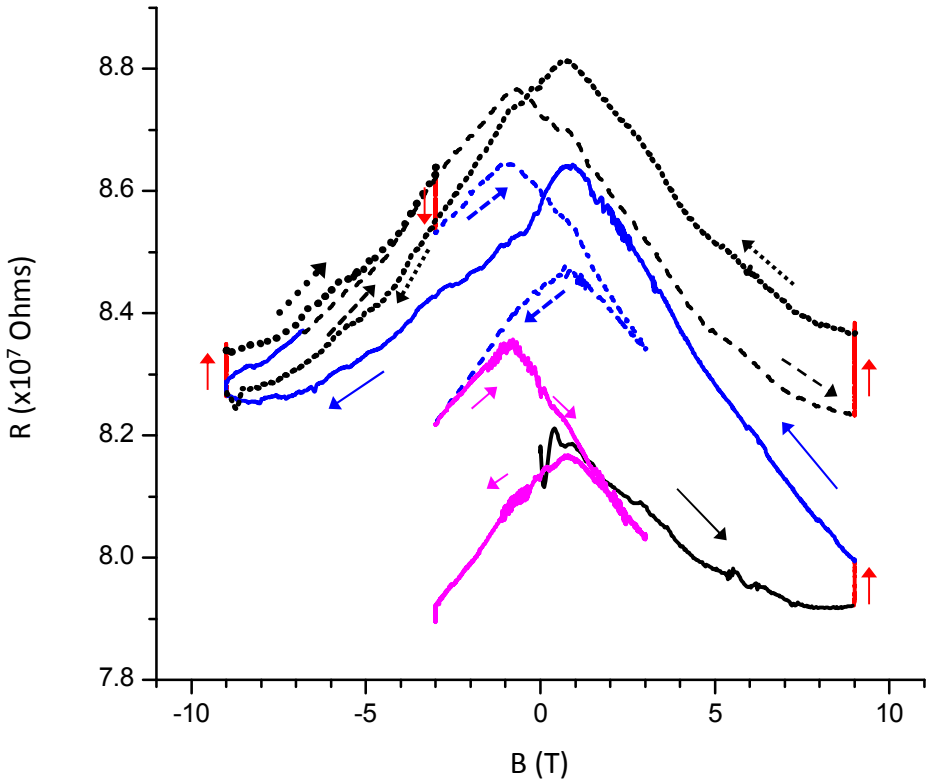

Figure 7.5: Asymmetric magnetoresistance measurements when V_G is changed at 10 K. Magnetic field B is swept at 1.2 T min^{-1}, 0.5 T min^{-1} and 0.25 T min^{-1} in the black, blue, and purple curves, respectively. Arrows denote the direction of the field sweep, and red curves represent pauses in the field sweep. Sweeps at the same rate are shown in different line styles to permit identification.

of the sample decreases. Because the field is sweeping, the decrease in resistance with time appears as a magnetoresistance feature. We hypothesize that there may be interesting physics in the field-dependent settling of the conductive channel resistance, but at this time we have focused primarily on the steady-state dynamics after settling, which we access by allowing the QD FET quickly settle at a particular V_G at temperatures above 60 K. This results in the symmetric, stable magnetoresistance curves shown in Section 7.4.

Temperature-dependent resistance measurements for various gate voltages V_G are shown in Figure 7.6a. We note that for zero gate bias the sample resistance exceeds our

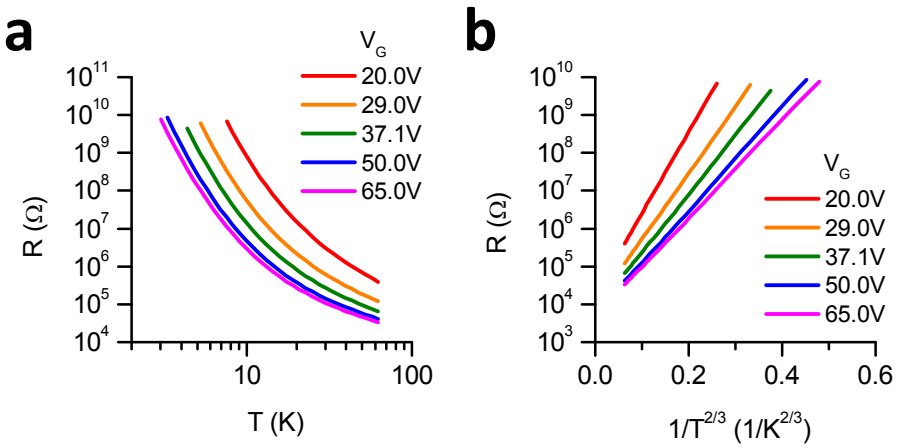

Figure 7.6: (a) Low temperature resistance, R, of a QD FET for different gate biases, V_G, as a function of temperature, T. (b) Resistance for different V_G plotted versus $1/T^{2/3}$. Data collected with $V_{DS} = 0.1$ V.

instrumentation limit below 60 K, and is thus not shown. All curves demonstrate insulating behavior obeying the VRH law (Equation (6.17)),

$$R(T) = R_0 \exp(T_0/T)^p \tag{7.2}$$

with temperature T, characteristic temperature T_0, resistance R, and characteristic resistance R_0. The hopping exponent p and the physical interpretation of T_0 depend on the transport mechanism. Our data show a compellingly linear relationship between $\log(R)$ and $T^{-2/3}$ for all gate biases (Figure 7.6b). For comparison, clearly non-linear curves are formed by assuming $p = 1/2$ instead of $2/3$ in a similar plot (Figure 7.7a).

For samples with a resistance R of the form in Equation (7.2), the reduced activation

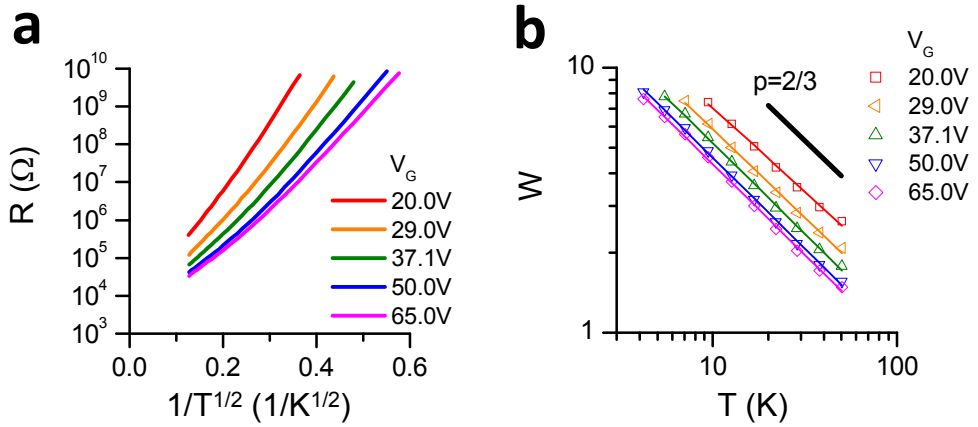

Figure 7.7: (a) Resistance, R, vs. $T^{-1/2}$ for different V_G. (b) Reduced activation energy $W = -\frac{d\ln R}{d\ln T}$ vs. T for a QD FET at V_G = 65 V. Lines indicate fits to the data yielding p equal to 0.63, 0.66, 0.68, 0.69 and 0.68 for V_G = 20.0, 29.0, 37.1, 50.0 and 65.0 V, respectively.

energy W can be used to extract p and T_0 objectively, where W is defined as follows:

$$W \equiv -\frac{d\ln R}{d\ln T} \tag{7.3}$$

$$= p\left(\frac{T_0}{T}\right)^p \tag{7.4}$$

$$\log W = \log\left(p(T_0)^p\right) - p\log T \tag{7.5}$$

A plot of $\log W$ vs $\log T$ is shown in Figure 7.7b with extracted values for T_0 and p. We can then extract numerical fits for p and T_0. Such analysis shown in Figure 7.7b, and yields values of p equal to 0.63, 0.66, 0.68, 0.69 and 0.68 for V_G = 20, 29, 37.1, 50 and 65 V, respectively.

It has been suggested that $p = 2/3$ could be observed as an admixture of $p = 1/2$ and $p = 1$ in an inhomogeneous sample.[80] We have some opportunity to test the relevance of this hypothesis to our samples because gate voltage adjustments have a dramatic influence on our measured resistances all the way down to the lowest measurable temperatures. Over a range of V_G from 20 to 65 V, the low temperature resistance drops by more than 3 orders

of magnitude, yet p remains constant. This behavior seems difficult to reconcile with a picture in which the VRH exponent is due to a competition between, for example, Coulomb gap and Arrhenius behavior. One would then expect such dramatic responses to gate voltage to represent a redistribution between Coulomb gap and Arrhenius contributions, and thus to produce a systematic variation in p, which we do not observe.

As shown in Figure 7.8, the measured $R(T)$ and $W(T)$ depend strongly on the applied drain-source bias of the sample, so we must be careful to ensure that the fitted values of p are not distorted by electric field activation.[192, 6] To this end, we measure the drain-source (V_{DS}) bias dependence of the reduced activation energy for all gate voltages. Figure 7.8 shows the most severe V_{DS} changes. The signature of metallicity, $\lim_{T\to 0} \frac{d\ln W}{d\ln T} > 0$, is seen for $V_{DS} > 1$ V (Figure 7.8b). Reducing V_{DS} shows this behavior is entirely due to field activation, not a metal insulator transition in our sample, and that limiting behavior in the slope of W, which determines p, is obtained for $V_{DS} = 0.1$ V. The data shown in Figure 7.6 are taken under these conditions and cut off when the current drops below 1×10^{-11} Amperes, which occurs before $I_{GS} > 0.1\ I_{DS}$. Leakage measurements between source/drain and gate electrode were acquired at V_{DS}=0.0001 V and subtracted from the warming curve to increase fidelity at low temperatures where the leakage current becomes relevant.

Hopping conduction can be connected to the presence of a mobility gap because VRH depends on both the localization length, a, and the dielectric constant, κ, and these quantities should both increase as $\Delta\varepsilon$ decreases. Algebraically, one expects[1, 114] $a \propto (\Delta\varepsilon)^{-\beta}$ and $\kappa \propto (\Delta\varepsilon)^{-\delta}$, where β and δ are critical exponents of order unity.[5, 85] Since gate bias adjusts ε_F and thus $\Delta\varepsilon$, the predictions of the Anderson model can be tested. In particular, the changes in slope that we observe for different V_G in Figure 7.6b arise from changes in T_0, which in turn depends on $a\kappa$. We denote the latter the "localization product," and for

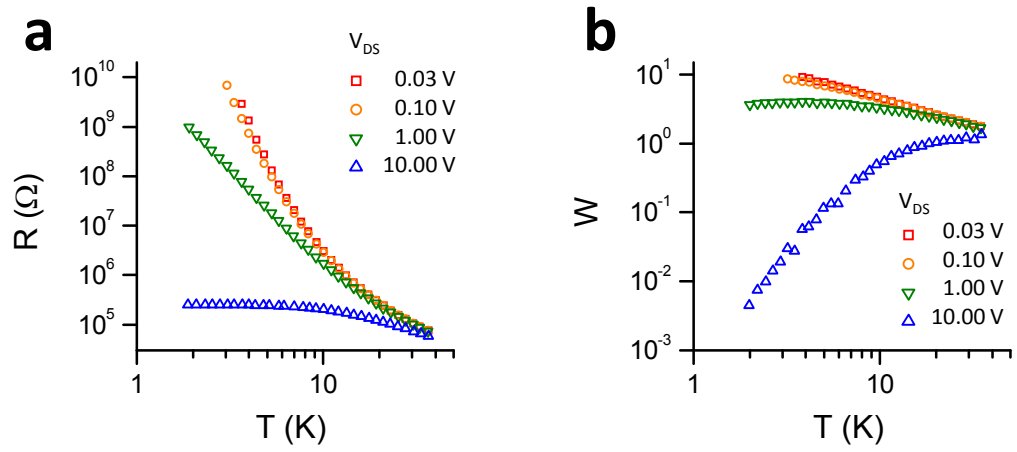

Figure 7.8: Drain-source bias dependence of (a) resistance and (b) reduced activation energy $W = -\frac{d\ln R}{d\ln T}$ vs temperature for a QD FET at $V_G = 65V$.

the $p = 2/3$ model of Coulomb gap plus thermal broadening, T_0 is given by

$$T_0 = \frac{3\sqrt{3}e^2}{8\pi a\kappa\varepsilon_0\sqrt{C_V k_B}} \qquad \text{(CG+thermal broadening)} \qquad (7.6)$$

with e the electron charge, ε_0 the permittivity of free space, k_B the Boltzmann constant, and $C_V = 3k_B$ the heat capacity of the conduction electron [91]. The black squares in Figure 7.9a show the localization product extracted from this equation and its dependence on V_G. A positive V_G increases the electron concentration, thereby raising ε_F and decreasing $\Delta\varepsilon$. The localization product increases as V_G ($\Delta\varepsilon$) increases (decreases). In addition, Figure 7.9b shows the dependence of a on V_G implied by assuming constant values of κ within a range expected for this system (see Ref. 237 and ellipsometry measurements in Figure 7.11).

We emphasize that our data, as shown in Figure 7.7, strongly support the assignment of $p = 2/3$. Nevertheless, for comparative purposes we also compute the localization product

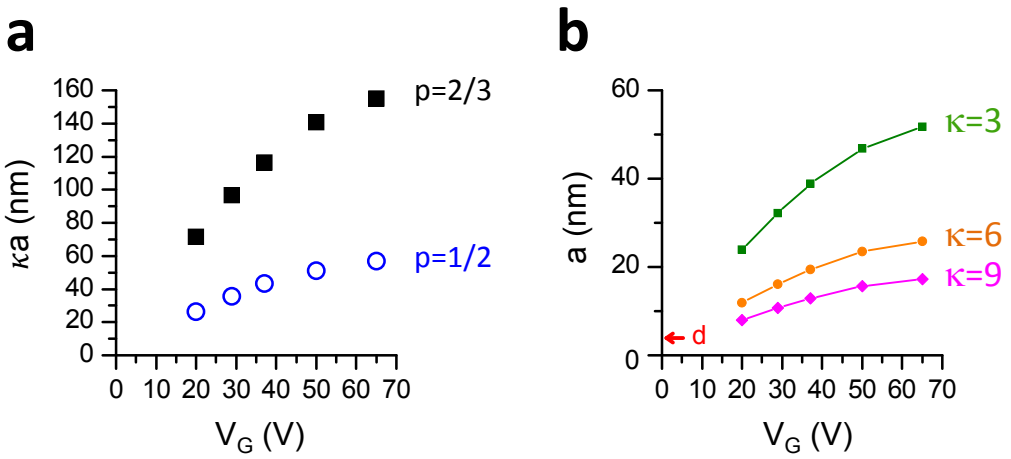

Figure 7.9: Gate bias dependence of (a) localization product, κa, plotted versus gate bias, V_G, for $p = 2/3$ (black filled squares) and $p = 1/2$ (blue open circles), as described in the text. (b) Gate bias dependence of localization lengths for κ = 3, 6 and 9 as indicated. Values in (b) computed for $p = 2/3$.

for the Coulomb gap model[214] according to

$$T_0 = \frac{2.8e^2}{4\pi a \kappa \varepsilon_0 k_B} \qquad \text{(CG)} \qquad (7.7)$$

where T_0 is determined self-consistently from (poor) fits of our data to $p = 1/2$. The result is shown in Figure 7.9a and shows that our qualitative conclusions are not model dependent.

A visual extrapolation of a toward the particle diameter at zero bias appears reasonable for κ somewhere between 3 and 6. As noted above, changes in both a and κ may be expected as the gate bias is applied so precise determination of a is not possible from this data. That being said, if the localization length is held fixed to the particle diameter, the range of κ implied is quite large and physically hard to justify without a concomitant change in a. Figure 7.10 shows the implied changes to the dielectric constant κ if the localization length were to remain unchanged with applied gate bias. Figure 7.11 shows the dielectric constant κ as measured in ellipsometry is around $\kappa \approx 6$. Thus, our data suggest that gate

bias expands the localization length beyond the particle diameter.

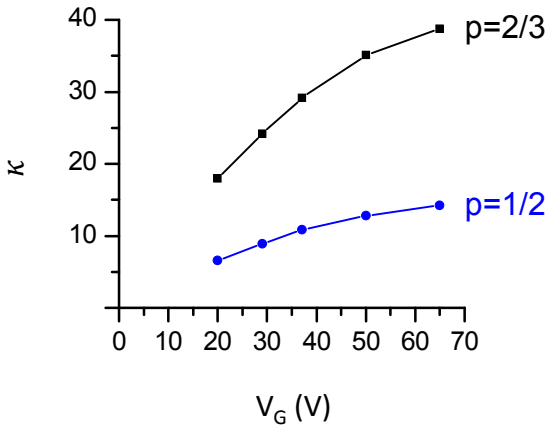

Figure 7.10: Dielectric constant κ that results if the localization length a is held fixed at the QD diameter.

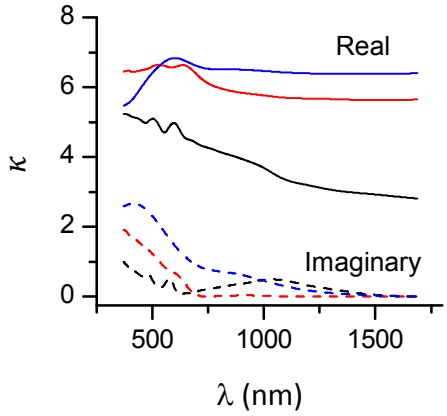

Figure 7.11: Measured dielectric constant from ellipsometry. Black: as-deposited, red: annealed without indium at 250 °C, blue: annealed with indium at 250 °C.

7.4 Magnetotransport Measurements

As described in Section 6.4, magnetoresistance (MR) measurements provide a complement to temperature dependent measurements. Representative MR measurements on the QD

FET, shown in Figure 7.12, display both positive and negative MR contributions whose magnitudes depend on both temperature (Figure 7.12a) and gate bias (Figure 7.12b). A more comprehensive cross-section of the data appears in Figure 7.13. We note that a low-field ($|B| \sim 100$ mT) positive MR component is barely visible in the data presented here but strengthens with high drain-source bias. This latter feature and its V_{DS} dependence has been extensively discussed elsewhere and assigned to a "spin blockade" due to random nuclear field mixing of spin singlets and triplets[82]. Here we focus on the more dominant features seen across entire field range.

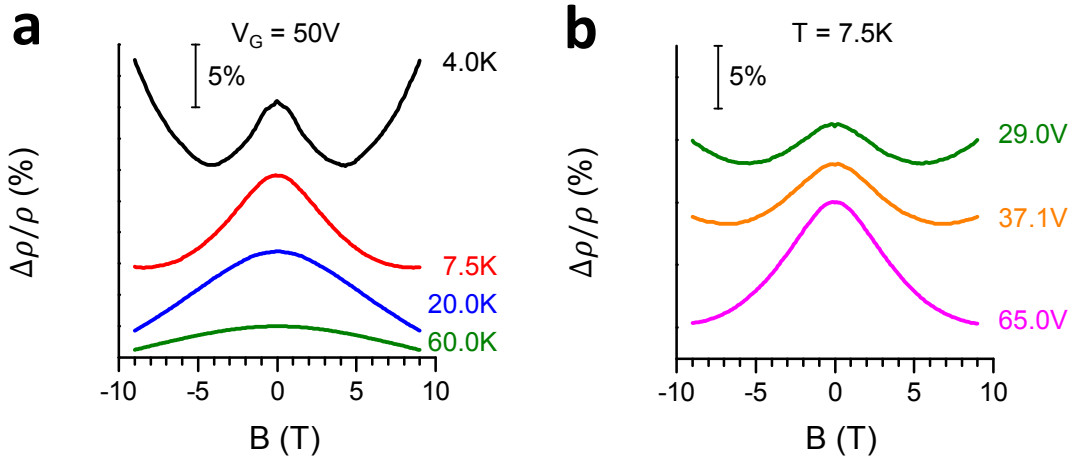

Figure 7.12: (a,b) Temperature and gate bias dependence of magnetoresistance of a QD FET at $V_G = 50$ V and T = 7.5 K, respectively. Plots are vertically offset for clarity. Data collected at $V_{DS} = 1$ V to improve signal to noise. No V_{DS} dependence of these large-field features was observed up to $V_{DS} = 10$ V.

MR at V_G= 20V maintained the presence of a positive high-field feature for all temperatures measured and was resultantly not used in the scaling analysis shown in the body text. For temperatures below 7.5K, V_G= 20V MR is not shown because the signal to noise ratio is insufficient.

Bi-directional sweeps of B are binned and averaged to produce all individual MR curves, and no hysteresis is seen in the forward and reverse field sweeps. Care is taken to ensure

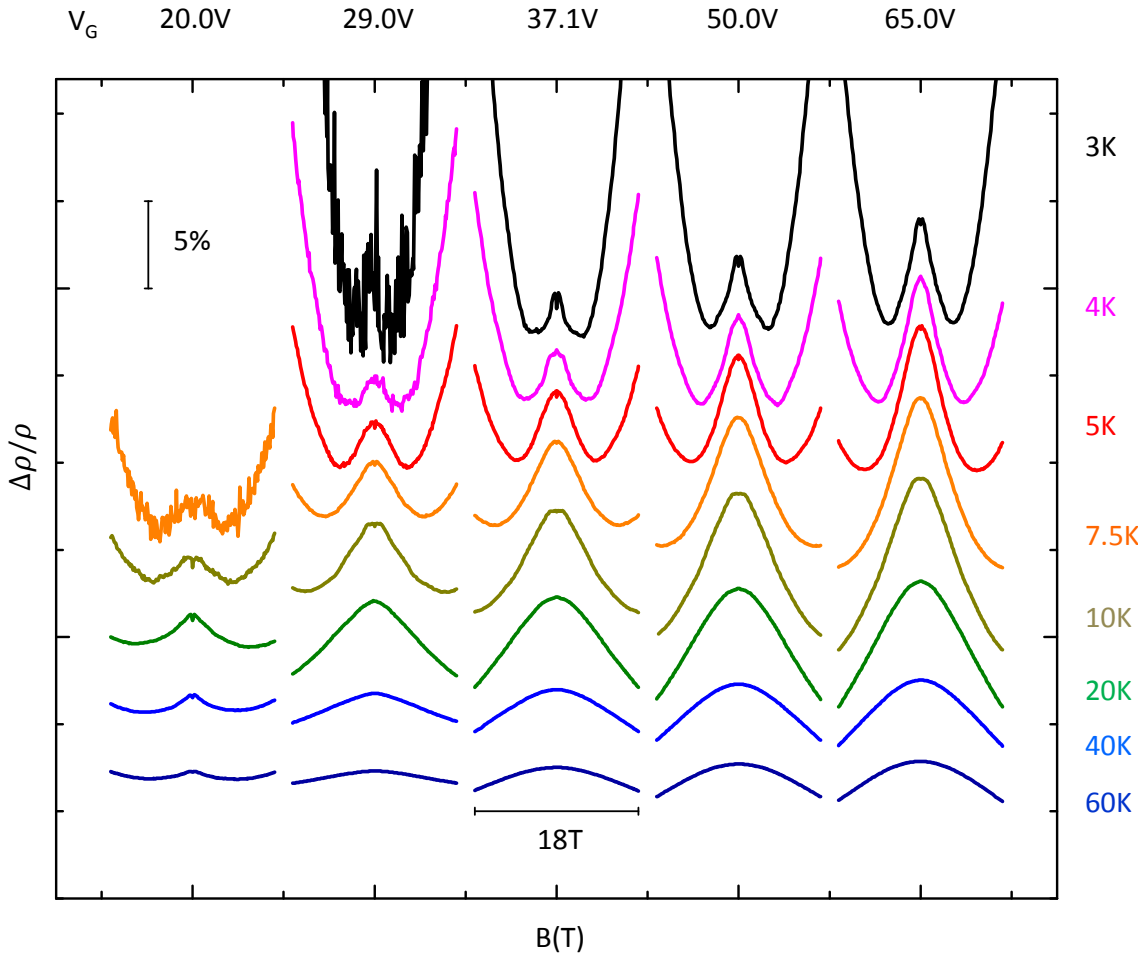

Figure 7.13: Magnetoresistance (MR) of a QD FET *vs.* applied gate bias V_G and temperature T. Plots are vertically and horizontally offset for clarity.

that MR of the Cernox temperature sensor is not convolved with sample MR at temperatures where $|dR/dT|$ is very large. In Appendix A, we elaborate on the method used to remove these effects.

To help filter the possible sources of magnetoresistance effects as described in Section 6.4, we now show that the MR data can be deconstructed as the superposition of two relatively simple line shapes with inverse power law temperature dependences T^{-x}. We first note that we observe a universal lineshape describing negative MR for higher temperatures

($T \geq 20$ K). Accordingly, for a given V_G we average the data from 20 K, 40 K, and 60 K to obtain this univeral line shape (Figure 7.14b, red curve), and find that its amplitude at those three temperatures obeys a scaling law T^{-x_1}. The values of x_1 are plotted in Figure 7.14c (red $\times$). This temperature dependence is then extrapolated to lower temperatures and subtracted from the MR data (Figures 7.14a,b), yielding a remaining positive MR contribution (Figure 7.14b, blue curve) with a predominantly parabolic form. Remarkably, the temperature dependence of the positive component is T^{-x_2} with x_2 very close to 2.0 (Figure 7.14c, blue +). Thus, our MR data set is well described by (1) a negative MR contribution with a characteristic line shape shown in Figure 7.14b (red curve) that has a temperature dependence T^{-x_1} and (2) a positive, parabolic MR contribution proportional to T^{-2}. We note that the alternative fitting method that starts by fitting the positive MR component produced largely similar values for the power law dependences on temperature.

The temperature dependence of (2) can be compared to theoretical predictions for the positive MR mechanisms described above. The associated exponent $x_2 = -2$ is well received by all mechanisms with known temperature predictions. Quantum corrections in VRH[215, 174] and wavefunction shrinkage in the presence of a transverse field[214] both scale as [215, 174] $T^{-3p} = T^{-2}$, and spin blockade scales as [82] T^{-2}. We note that the latter is conventionally associated with nuclear spin disorder, and saturates at very low fields, whereas (2) does not. Classical disorder induced MR does not have a clear temperature prediction for our system, but its characteristic signature is a transition to a linear behavior at high fields which we do not observe here.[186]

The temperature dependence of (1) is more telling. The hopping nature of conduction in these samples makes weak localization physically inappropriate, and the spin blockade mechanism is that associated with the weak, low-field positive MR signal discussed above. Quantum corrections to hopping interference are mostly negative but, as discussed above, predict T^{-2}, which is far from what we observe here. Zeeman energy modulation of the

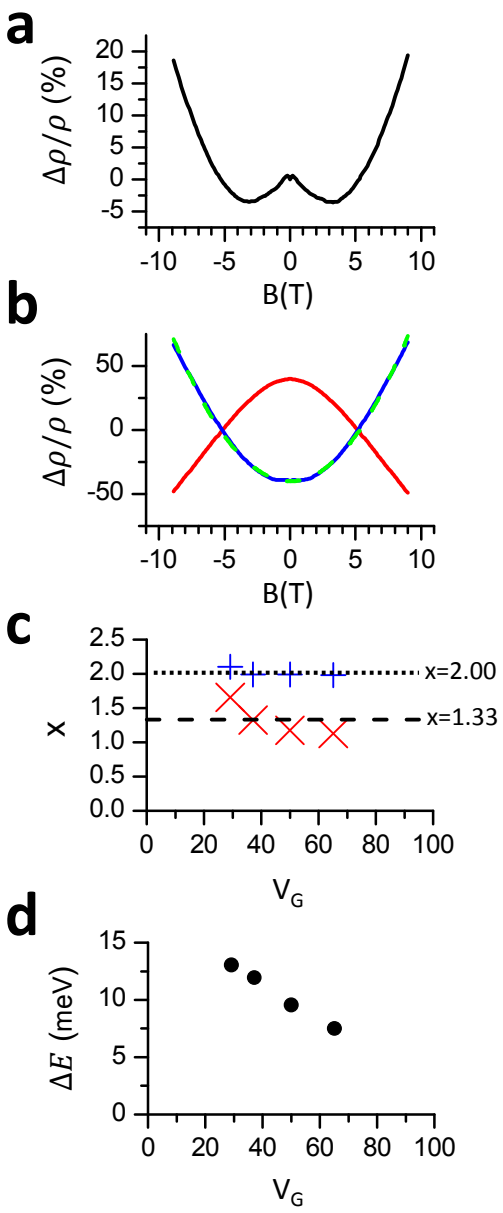

Figure 7.14: (a) Magnetoresistance of a QD FET at $V_G = 50$ V, T = 3 K. (b) Decomposition of (a) into negative (red) and positive (blue) components as described in text. Green shows a parabolic fit to the positive component. (c) Exponents of temperature dependence, x_1 (red $\times$) and x_2 (blue +), describing power law temperature dependence, MR $\propto T^{-x}$, for negative and positive components of the MR. Point sizes indicate error bars. (d) Mobility gap $\Delta\varepsilon$ extracted using $p = 2/3$.

mobility gap predicts[60]

$$\frac{\Delta\rho}{\rho_0} = -\frac{1}{2}\big(p(\beta+\delta)d\big)^2 \frac{(\frac{1}{2}g\mu_B B)^2}{\Delta\varepsilon^2}\left(\frac{T_0}{T}\right)^{2p} \tag{7.8}$$

where $g \sim 1.2$ is the electron g-factor for CdSe[78], μ_B is the Bohr magneton, d is the dimensionality of the system, and β, δ and $\Delta\varepsilon$ are defined above. Note that here we modify the expression found in Ref. 60 to include the divergence of the dielectric constant, κ. The associated temperature dependence for $p = 2/3$ is $T^{-1.33}$, which is shown as a dotted line in Figure 7.14c and for which the values of x_1 show relatively good agreement.

Thus, Zeeman modulation of the mobility gap fits the negative MR signal best, and in many ways it is a magnetic counterpart to the application of a gate bias. In contrast to a gate bias, however, the exact variation in the gap is known from the g-factor. Thus, Eqn. 7.8 gives a value for the mobility gap, which we can obtain for each value of V_G. Figure 7.14d shows the inferred mobility gap taking $\beta \sim 1$ and $\delta \sim 1$,[5, 85] setting $d = 3$, and using $p = 2/3$ and the magnitude of the MR at 1 T. Values of T_0 are those collected synchronously with MR data and vary slightly from those listed earlier. With increasing gate bias the calculated mobility gap clearly decreases, and the trend of the gate bias dependence indicates that for sufficiently high values of V_G the devices may transition to a metallic state characterized by delocalized states.

7.5 Conclusion

In conclusion, by combining the analysis of the temperature-dependent resistance and MR, a cohesive picture of electrical transport in these QD FETs emerges. The low temperature transport studied in this report is consistent with a Coulomb gapped density of states with thermal broadening in an Anderson localized insulator. The negative MR feature is

consistent with that expected from Zeeman splitting in the presence of Anderson localization. The data provide strong evidence that gate bias delocalizes electrons in this system beyond the particle diameter, a behavior consistent with a Fermi level approaching the mobility edge in a system with a mobility gap. Magnetoresistance shows both positive and negative components, with the latter bearing a temperature dependence and magnitude also consistent with a mobility gap that acquires a magnetic field dependence through the spin Zeeman energy. These data provide compelling motivation for further studies that pursue high gate biases in an effort to observe an insulator-metal transition in these systems. We also see justification to further study the V_{DS} dependence as well as the temperature- and field-dependent settling of resistance when changing V_G at low temperatures.

Chapter 8

Conclusions

In this dissertation, we described several studies of optical and electronic interactions in nanometer scale semiconductor systems. We first described in Chapter 3 the construction and optimization of an integrated time-resolved photoluminescence and absorption apparatus to probe charge carrier relaxation dynamics on the femtosecond to nanosecond timescales.

In Chapter 4 we used this apparatus to study the interaction among CdSe quantum dots and between the quantum dot core states and surface states, demonstrating that the sample treatment described there led to increased electron trapping to quantum dot surface states. We also showed that the conventional interpretation of a signal in time-resolved absorption spectra of CdSe quantum dots must be interpreted differently than previously understood.

In Chapter 5 we also used this time-resolved photoluminsence microscope to prove that a interactions between electron oscillations in a resonant, plasmonic cavity and excitons in a CdS nanowire core can increase the radiative rate, leading to the observation of hot-exciton luminescence due to the Purcell effect.

We came full circle and concluded in Chapter 7 with purely electronic studies of electrical transport in high-mobility CdSe quantum dot field effect transistors in which

inter-dot interactions are fundamentally important. In this chapter, we demonstrated that the application of a gate bias to the transistor leads to an increasingly delocalized electrons to significantly greater than the quantum dot diameter. In magnetotransport measurements, we observed a negative magnetoresistance component consistent with Anderson Zeeman magnetoresistance, and from the variations in the magnitude of this component with applied gate bias, we observed that the mobility gap separating localized and extended states becomes progressively smaller with increases in applied gate bias.

Appendix A

Cernox Corrections to Magnetoresistance

A.1 Cernox

The Quantum Design Physical Property Measurement System has a built-in calibration table to correct for magnetoresistance effects in the reported resistance, and thereby temperature, of the Cernox temperature sensor measuring the sample temperature. Features that we observed in magnetoresistance curves of the QD FET (Figure A.1) appears segmented in a manner that does not vary smoothly, raising the possibility of a miscalibration of the Cernox temperature sensor.

In the case of the QD FETs measured in Chapter 7, the strong temperature dependence of resistance means any deviations of the reported temperature from the actual temperature will appear in the MR curves. In Figure A.2 we compare the temperature dependence of the Cernox resistance versus a representative curve of the temperature dependence of the QD FET at V_G=50 V. This Figure shows the high sensitivity of the QD FET to temperature; both curves are scaled by $R(T = 5K)$. The relatively fast changes in the resistance of the

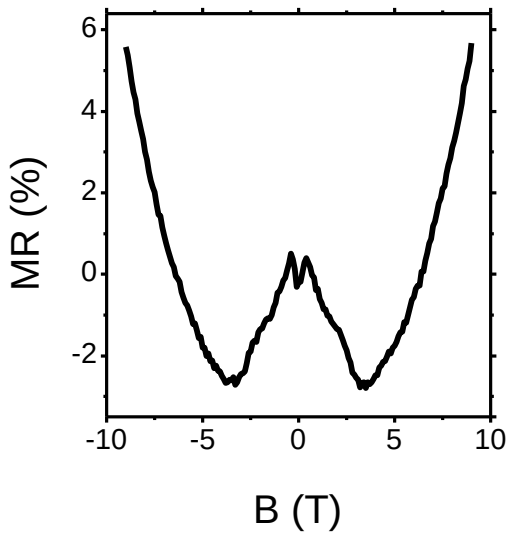

Figure A.1: Uncorrected magnetoresistance (MR) of a QD FET *vs.* temperature T at V_G=29.1 V and V_{DS}=1 V.

QD FET as compared to the Cernox sensor suggest that any miscalibrations in the MR dependence of the PPMS temperature sensor will propagate into the measured MR curves for the sample.

The calibration table stored in the PPMS reports the percent error in the reported temperature as for a set of 20 temperatures and magnetic field magnitudes. A color plot of this table is shown in Figure A.3a. In order to determine the interpolation method the PPMS uses to apply this calibration during experiments, we measured the resistance of the Cernox vs. B and then converted this reported resistance to an error in temperature using the R(T) curve. If we interpolate the PPMS temperature table using a 2D bicubic spline method (interpolated values shown in A.3b and A.4a), we find that good agreement with measured correction. Errors are shown in Figure A.4b. We have therefore verified our interpretation of the calibration table and can correct out the unphysical features produced by the table.

To do this, we manually generated a new calibration table in which the high-frequency

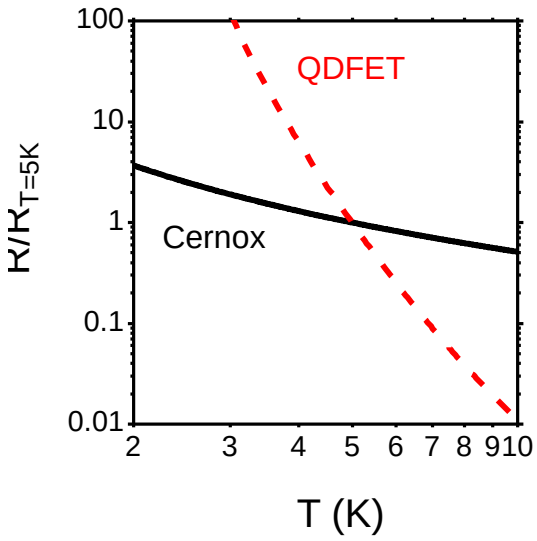

Figure A.2: Temperature dependence of resistance R for QD FET (red dash) and Cernox temperature sensor (black solid), scaled as $R/R(T = 5K)$

oscillations near zero field have been removed. These oscillations could be produced by impulse heating due to fast magnetic field changes. This calibration is created by fitting an n^{th} order polynomial to the calibration curve from -9 T to 9 T. The resultant interpolated temperature error map is shown in Figure A.3c and clearly removes many of the unphysical features.

Our correction procedure to remove this miscalibration is as follows:

1. Calculate difference $\Delta C(T,B) = C_F(T,B) - C'(T,B)$ between factory temperature error calibration table C_F and corrected calibration table C' at all magnetic field B and temperature T values.

2. Interpolate $\Delta C(T,B)$ at temperature and field values used in scan using bicubic spline, providing the percent error in the reported temperature.

3. Compare the measured R versus the expected R for the erroneous temperature:

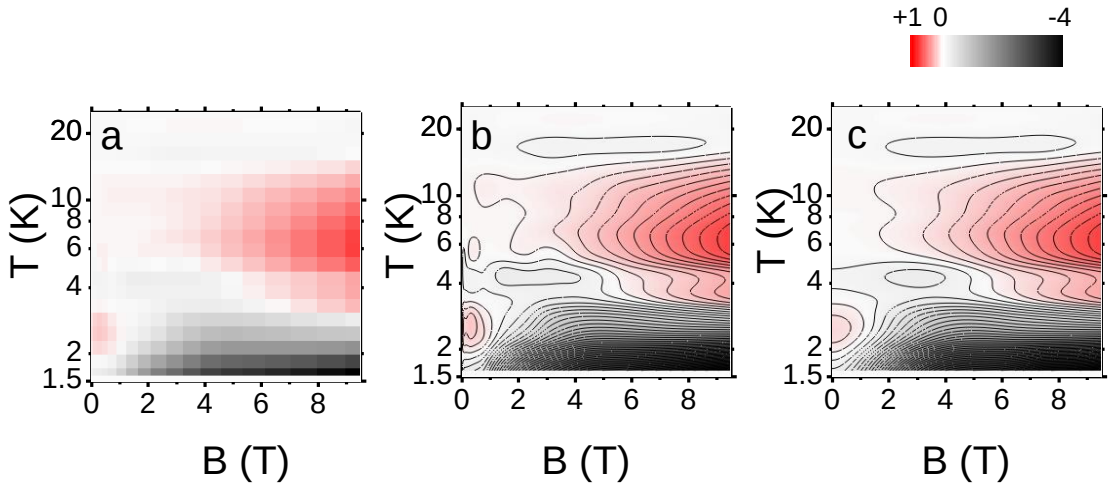

Figure A.3: PPMS temperature error calibration. (a) Table values. (b) Interpolated values of factory calibration. (c) Smoothed values with high frequency oscillations removed.

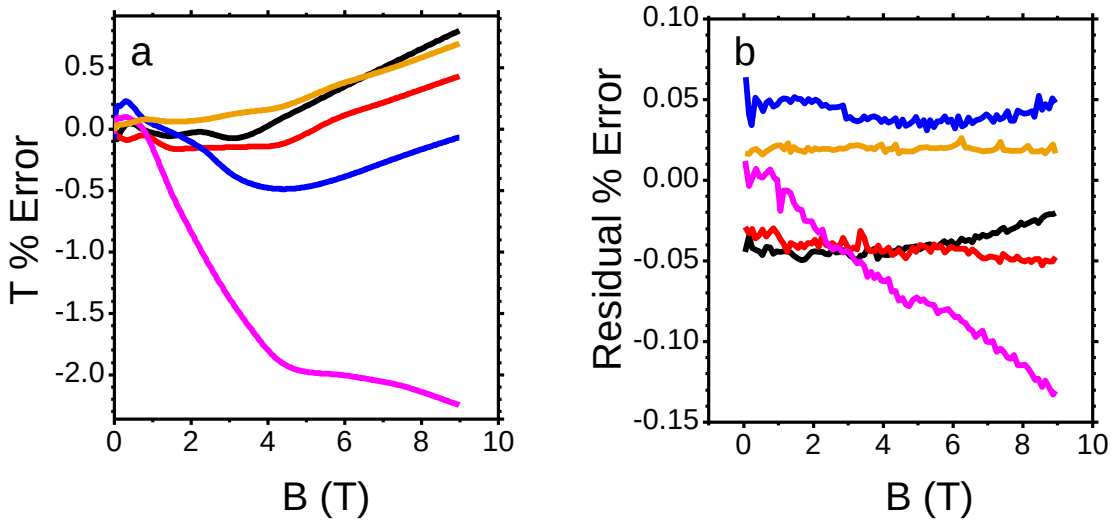

Figure A.4: PPMS Cernox temperature corrections. (a) Interpolated values of table using 2D bicubic spline. (b) Error between interpolated values and measured equivalent temperature from Cernox.

(a) Calculate the actual temperature of sample, $T_a(B) = \left(1 - \frac{\Delta C(T,B)}{100}\right) T_m$ at each field position using measured temperature T_m.

(b) Sample resistance at temperature T may deviate from expectation from $R_e(T)$ curve. We scale the measured $R(B)$ by this factor α to remove this deviation. $\alpha = \frac{R_e(T)}{R_e(T_a(|B|))}$

(c) Actual MR is determined as:

$$MR_a(\%) = 100 \left(\underbrace{\left(1 + \frac{MR(\%)}{100}\right)}_{R(B)/R(B=0)} \alpha - 1 \right) \tag{A.1}$$

The correction is applied by interpolating the difference between the smoothed calibration table and the factory calibration table. We show this comparison for S2D1 at V_G=29 V in Figure A.5 where (a) shows the MR curves with factory calibration, (b) shows with corrected calibration, and (c) shows the temperature error that has been removed from the factory calibration.

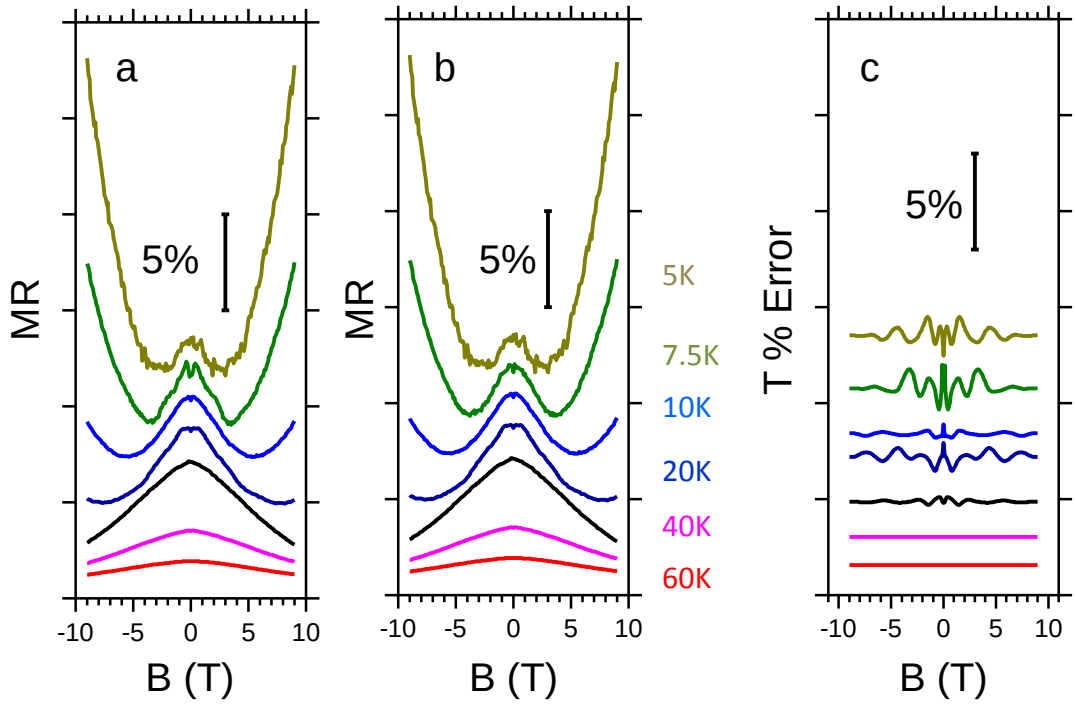

Figure A.5: Example PPMS temperature correction method. MR (a) before and (b) after (c) PPMS temperature calibration correction applied.

Bibliography

[1] E. Abrahams, P. W. Anderson, D. C. Licciardello, and T. V. Ramakrishnan. Scaling theory of localization: Absence of quantum diffusion in two dimensions. *Phys. Rev. Lett.*, 42(10):673–676, Mar 1979. doi:10.1103/PhysRevLett.42.673.

[2] M. Achermann, J. A. Hollingsworth, and V. I. Klimov. Multiexcitons confined within a subexcitonic volume: Spectroscopic and dynamical signatures of neutral and charged biexcitons in ultrasmall semiconductor nanocrystals. *Phys. Rev. B*, 68: 245302, 2003. doi:10.1103/PhysRevB.68.245302.

[3] Marc Achermann, Melissa A. Petruska, Scott A. Crooker, and Victor I. Klimov. Picosecond energy transfer in quantum dot langmuir-blodgett nanoassemblies. *J. Phys. Chem. B*, 107(50):13782–13787, 2003. doi:10.1021/jp036497r.

[4] Gleb M. Akselrod, Ferry Prins, Lisa V. Poulikakos, Elizabeth M. Y. Lee, Mark C. Weidman, A. Jolene Mork, Adam P. Willard, Vladimir Bulović, and William A. Tisdale. Subdiffusive exciton transport in quantum dot solids. *Nano Letters*, 14(6): 3556–3562, 2014. doi:10.1021/nl501190s.

[5] P. W. Anderson. Absence of diffusion in certain random lattices. *Phys. Rev.*, 109: 1492–1505, Mar 1958. doi:10.1103/PhysRev.109.1492.

[6] N. Apsley and H. P. Hughes. Temperature- and field-dependence of hopping conduction in disordered systems, ii. *Philosophical Magazine*, 31(6):1327–1339, 1975. doi:10.1080/00318087508228686.

[7] Akhilesh K. Arora, M. Rajalakshmi, T. R. Ravindran, and V. Sivasubramanian. Raman spectroscopy of optical phonon confinement in nanostructured materials. *Journal of Raman Spectroscopy*, 38(6):604–617, 2007. doi:10.1002/jrs.1684.

[8] M. V. Artemyev, A. I. Bibik, L. I. Gurinovich, S. V. Gaponenko, and U. Woggon. Evolution from individual to collective electron states in a dense quantum dot ensemble. *Phys. Rev. B*, 60:1504–1506, Jul 1999. doi:10.1103/PhysRevB.60.1504.

[9] S. Arzhantsev and M. Maroncelli. Design and characterization of a femtosecond fluorescence spectrometer based on optical kerr gating. *Appl. Spectrosc.*, 59(2): 206–220, Feb 2005. doi:10.1366/0003702053085007.

[10] David R. Baker and Prashant V. Kamat. Tuning the emission of cdse quantum dots by controlled trap enhancement. *Langmuir*, 26(13):11272–11276, 2010. doi:10.1021/la100580g.

[11] William L. Barnes, Alain Dereux, and Thomas W. Ebbesen. Surface plasmon subwavelength optics. *Nature*, 424(6950):824–830, 2003. doi:10.1038/nature01937.

[12] H. Benisty, C. M. Sotomayor-Torrès, and C. Weisbuch. Intrinsic mechanism for the poor luminescence properties of quantum-box systems. *Phys. Rev. B*, 44:10945–10948, Nov 1991. doi:10.1103/PhysRevB.44.10945.

[13] Gerd Bergmann. Weak localization in thin films: a time-of-flight experiment with conduction electrons. *Physics Reports*, 107(1):1 – 58, 1984. doi:10.1016/0370-1573(84)90103-0.

[14] Juliette Billy, Vincent Josse, Zhanchun Zuo, Alain Bernard, Ben Hambrecht, Pierre Lugan, David Clement, Laurent Sanchez-Palencia, Philippe Bouyer, and Alain Aspect. Direct observation of anderson localization of matter waves in a controlled disorder. *Nature*, 453(7197):891–894, June 2008.

[15] Simon C. Boehme, T. Ardaan Walvis, Ivan Infante, Ferdinand C. Grozema, Danil Vanmaekelbergh, Laurens D. A. Siebbeles, and Arjan J. Houtepen. Electrochemical control over photoinduced electron transfer and trapping in cdse-cdte quantum-dot solids. *ACS Nano*, 8(7):7067–7077, 2014. doi:10.1021/nn501985e.

[16] M.J. Bowers II, J.R. McBride, M.D. Garrett, J.A. Sammons, A.D. Dukes III, M.A. Schreuder, T.L. Watt, A.R. Lupini, S.J. Pennycook, and S.J. Rosenthal. Structure and ultrafast dynamics of white-light-emitting cdse nanocrystals. *Journal of the American Chemical Society*, 131(16):5730–5731, 2009. doi:10.1021/ja900529h.

[17] A.R. Brown, C.P. Jarrett, D.M. de Leeuw, and M. Matters. Field-effect transistors made from solution-processed organic semiconductors. *Synthetic Metals*, 88(1):37 – 55, 1997. doi:10.1016/S0379-6779(97)80881-8.

[18] Jannise J. Buckley, Elsa Couderc, Matthew J. Greaney, James Munteanu, Carson T. Riche, Stephen E. Bradforth, and Richard L. Brutchey. Chalcogenol ligand toolbox for cdse nanocrystals and their influence on exciton relaxation pathways. *ACS Nano*, 8(3):2512–2521, 2014. doi:10.1021/nn406109v.

[19] C. Burda, T. C. Green, S. Link, and M. A. El-Sayed. Electron shuttling across the interface of cdse nanoparticles monitored by femtosecond laser spectroscopy. *J. Phys. Chem. B*, 103(11):1783–1788, 1999. doi:10.1021/jp9843050.

[20] Marco Califano and Francisco M. Gomez-Campos. Universal trapping mech-

anism in semiconductor nanocrystals. *Nano Letters*, 13(0):2047–2052, 2013. doi:10.1021/nl4003014.

[21] Marco Califano, Alberto Franceschetti, and Alex Zunger. Lifetime and polarization of the radiative decay of excitons, biexcitons, and trions in cdse nanocrystal quantum dots. *Phys. Rev. B*, 75:115401, Mar 2007. doi:10.1103/PhysRevB.75.115401.

[22] J. W. Chan, T. Huser, S. Risbud, and D. M. Krol. Structural changes in fused silica after exposure to focused femtosecond laser pulses. *Opt. Lett.*, 26(21):1726–1728, Nov 2001. doi:10.1364/OL.26.001726.

[23] Ou Chen, He Wei, Axel Maurice, Moungi Bawendi, and Peter Reiss. Pure colors from coreshell quantum dots. *MRS Bulletin*, 38:696–702, 9 2013. doi:10.1557/mrs.2013.179.

[24] Ou Chen, Jing Zhao, Vikash P. Chauhan, Jian Cui, Cliff Wong, Daniel K. Harris, He Wei, Hee-Sun Han, Dai Fukumura, Rakesh K. Jain, and Moungi G. Bawendi. Compact high-quality cdse-cds core-shell nanocrystals with narrow emission linewidths and suppressed blinking. *Nat Mater*, 12(5):445–451, May 2013. doi:10.1038/nmat3539.

[25] Tianran Chen, Brian Skinner, and B. I. Shklovskii. Cooperative charging in a nanocrystal assembly gated by ionic liquid. *Phys. Rev. B*, 84:245304, Dec 2011. doi:10.1103/PhysRevB.84.245304.

[26] Chang-Hee Cho, Carlos O. Aspetti, Michael E. Turk, James M. Kikkawa, Sung-Wook Nam, and Ritesh Agarwal. Tailoring hot-exciton emission and lifetimes in semiconducting nanowires via whispering-gallery nanocavity plasmons. *Nature Materials*, 10:669–675, 2011. doi:10.1038/nmat3067.

[27] Ji-Hyuk Choi, Aaron T. Fafarman, Soong Ju Oh, Dong-Kyun Ko, David K. Kim, Benjamin T. Diroll, Shin Muramoto, J. Greg Gillen, Christopher B. Murray, and Cherie R. Kagan. Bandlike transport in strongly coupled and doped quantum dot solids: A route to high-performance thin-film electronics. *Nano Letters*, 12(5): 2631–2638, 2012. doi:10.1021/nl301104z.

[28] Ji-Hyuk Choi, Soong Ju Oh, Yuming Lai, David K. Kim, Tianshuo Zhao, Aaron T. Fafarman, Benjamin T. Diroll, Christopher B. Murray, and Cherie R. Kagan. In situ repair of high-performance, flexible nanocrystal electronics for large-area fabrication and operation in air. *ACS Nano*, 7(9):8275–8283, Sep 2013. doi:10.1021/nn403752d.

[29] Chi-Hung Chuang, Xiaobo Chen, and Clemens Burda. Femtosecond time-resolved hot carrier energy distributions of photoexcited semiconductor quantum dots. *Annalen der Physik*, 525(1-2):43–48, 2013. doi:10.1002/andp.201200129.

[30] Dae Sung Chung, Jong-Soo Lee, Jing Huang, Angshuman Nag, Sandrine Ithurria, and Dmitri V. Talapin. Low voltage, hysteresis free, and high mobility transistors from all-inorganic colloidal nanocrystals. *Nano Letters*, 12(4):1813–1820, 2012. doi:10.1021/nl203949n.

[31] Neslihan Cicek, Sedat Nizamoglu, Tuncay Ozel, Evren Mutlugun, Durmus Ugur Karatay, Vladimir Lesnyak, Tobias Otto, Nikolai Gaponik, Alexander Eychmller, and Hilmi Volkan Demir. Structural tuning of color chromaticity through nonradiative energy transfer by interspacing cdte nanocrystal monolayers. *Applied Physics Letters*, 94(6):061105, 2009. doi:10.1063/1.3079679.

[32] C. Conti and A. Fratalocchi. Dynamic light diffusion, three-dimensional anderson localization and lasing in inverted opals. *Nat Phys*, 4(10):794–798, October 2008.

[33] R.R. Cooney, S.L. Sewall, E.A. Dias, D.M. Sagar, K.E.H. Anderson, and P. Kambhampati. Unified picture of electron and hole relaxation pathways in semiconductor quantum dots. *Physical Review B - Condensed Matter and Materials Physics*, 75 (24):245311, 2007. doi:10.1103/PhysRevB.75.245311.

[34] Ryan R. Cooney, Samuel L. Sewall, D. M. Sagar, and Patanjali Kambhampati. Gain control in semiconductor quantum dots via state-resolved optical pumping. *Phys. Rev. Lett.*, 102:127404, Mar 2009. doi:10.1103/PhysRevLett.102.127404.

[35] Ryan W Crisp, Joel N Schrauben, Matthew C Beard, Joseph M Luther, and Justin C Johnson. Coherent exciton delocalization in strongly coupled quantum dot arrays. *Nano Letters*, 13(10):4862–4869, 2013.

[36] S. A. Crooker, J. A. Hollingsworth, S. Tretiak, and V. I. Klimov. Spectrally resolved dynamics of energy transfer in quantum-dot assemblies: Towards engineered energy flows in artificial materials. *Phys. Rev. Lett.*, 89:186802, 2002. doi:10.1103/PhysRevLett.89.186802.

[37] S. A. Crooker, T. Barrick, J. A. Hollingsworth, and V. I. Klimov. Multiple temperature regimes of radiative decay in cdse nanocrystal quantum dots: Intrinsic limits to the dark-exciton lifetime. *Applied Physics Letters*, 82(17):2793–2795, 2003. doi:10.1063/1.1570923.

[38] A. S. Dhoot, G. M. Wang, D. Moses, and A. J. Heeger. Voltage-induced metal-insulator transition in polythiophene field-effect transistors. *Phys. Rev. Lett.*, 96: 246403, Jun 2006. doi:10.1103/PhysRevLett.96.246403.

[39] S. L. di Vittorio, M. S. Dresselhaus, M. Endo, and T. Nakajima. Magnetotransport at the metal-insulator transition in fluorine-intercalated graphite fibers. *Phys. Rev. B*, 43:12304–12315, May 1991. doi:10.1103/PhysRevB.43.12304.

[40] Eva A. Dias, Jonathan I. Saari, Pooja Tyagi, and Patanjali Kambhampati. Improving optical gain performance in semiconductor quantum dots via coupled quantum shells. *The Journal of Physical Chemistry C*, 116(9):5407–5413, 2012. doi:10.1021/jp211325x.

[41] M.S. Dresselhaus, G. Dresselhaus, R. Saito, and A. Jorio. Raman spectroscopy of carbon nanotubes. *Physics Reports*, 409(2):47 – 99, 2005. doi:http://dx.doi.org/10.1016/j.physrep.2004.10.006.

[42] M. A. Duguay and J. W. Hansen. An ultrafast light gate. *Applied Physics Letters*, 15 (6):192–194, 1969. doi:10.1063/1.1652962.

[43] A. L. Efros. Fine structure and polarization properties of band-edge excitons in semiconductor nanocrystals. In V. I. Klimov, editor, *Nanocrystal Quantum Dots*, chapter 3. CRC Press, 2nd edition, 2010.

[44] A L Efros and B I Shklovskii. Coulomb gap and low temperature conductivity of disordered systems. *Journal of Physics C: Solid State Physics*, 8(4):L49, 1975.

[45] A.L. Efros and M. Rosen. Electronic structure of semiconductor nanocrystals. *Annual Review of Materials Science*, 30:475–521, 2000. doi:10.1146/annurev.matsci.30.1.475.

[46] Al. L. Efros and A. L. Efros. Interband absorption of light in a semiconductor sphere. *Soviet Physics Semiconductors*, 16:772–775, 1982.

[47] Al. L. Efros, V.A. Kharchenko, and M. Rosen. Breaking the phonon bottleneck in nanometer quantum dots: Role of auger-like processes. *Solid State Communications*, 93(4):281 – 284, 1995. doi:10.1016/0038-1098(94)00760-8.

[48] Al. L. Efros, M. Rosen, M. Kuno, M. Nirmal, D. J. Norris, and M. Bawendi. Band-edge exciton in quantum dots of semiconductors with a degenerate valence band: Dark and bright exciton states. *Phys. Rev. B*, 54:4843–4856, Aug 1996. doi:10.1103/PhysRevB.54.4843.

[49] A. I. Ekimov and A. A. Onushchenko. Size quantization of the electron energy spectrum in a microscopic semiconductor crystal. *JETP Letters*, 40:1136, 1985.

[50] A. I. Ekimov, F. Hache, M. C. Schanne-Klein, D. Ricard, C. Flytzanis, I. A. Kudryavtsev, T. V. Yazeva, A. V. Rodina, and Al. L. Efros. Absorption and intensity-dependent photoluminescence measurements on cdse quantum dots: assignment of the first electronic transitions. *J. Opt. Soc. Am. B*, 10(1):100–107, Jan 1993. doi:10.1364/JOSAB.10.000100.

[51] Annemarie L. Exarhos, Michael E. Turk, and James M. Kikkawa. Ultrafast spectral migration of photoluminescence in graphene oxide. *Nano Letters*, 13(2):344–349, 2013. doi:10.1021/nl302624p.

[52] Aaron T. Fafarman, Weon-kyu Koh, Benjamin T. Diroll, David K. Kim, Dong-Kyun Ko, Soong Ju Oh, Xingchen Ye, Vicky Doan-Nguyen, Michael R. Crump, Danielle C. Reifsnyder, Christopher B. Murray, and Cherie R. Kagan. Thiocyanate-capped nanocrystal colloids: Vibrational reporter of surface chemistry and solution-based route to enhanced coupling in nanocrystal solids. *J. Am. Chem. Soc.*, 133(39): 15753–15761, 2011. doi:10.1021/ja206303g.

[53] Mark J. Fernée, Chiara Sinito, Yann Louyer, Christian Potzner, Tich-Lam Nguyen, Paul Mulvaney, Philippe Tamarat, and Brahim Lounis. Magneto-optical properties of trions in non-blinking charged nanocrystals reveal an acoustic phonon bottleneck. *Nat Commun*, 3:1287, December 2012.

[54] G. R. Fleming. *Chemical Applications of Ultrafast Spectroscopy*. Oxford University Press, 1986.

[55] Edward E. Foos. The complex interaction of spectroscopic shifts and electronic properties in semiconductor nanocrystal films. *The Journal of Physical Chemistry Letters*, 4(4):625–632, 2013. doi:10.1021/jz3021364.

[56] A. Franceschetti, H. Fu, L. W. Wang, and A. Zunger. Many-body pseudopotential theory of excitons in inp and cdse quantum dots. *Phys. Rev. B*, 60:1819–1829, Jul 1999. doi:10.1103/PhysRevB.60.1819.

[57] Alberto Franceschetti and Alex Zunger. Direct pseudopotential calculation of exciton coulomb and exchange energies in semiconductor quantum dots. *Phys. Rev. Lett.*, 78:915–918, Feb 1997. doi:10.1103/PhysRevLett.78.915.

[58] Matthew T. Frederick and Emily A. Weiss. Relaxation of exciton confinement in cdse quantum dots by modification with a conjugated dithiocarbamate ligand. *ACS Nano*, 4(6):3195–3200, 2010. doi:10.1021/nn1007435.

[59] Huaxiang Fu, Lin-Wang Wang, and Alex Zunger. Comparison of the kp and the direct diagonalization approaches for describing the electronic structure of quantum dots. *Applied Physics Letters*, 71(23):3433, 1997. doi:10.1063/1.120421.

[60] Hidetoshi Fukuyama and Kei Yoshida. Negative magnetoresistance in the anderson localized states. *Journal of the Physical Society of Japan*, 46(1):102–105, 1979. doi:10.1143/JPSJ.46.102.

[61] A. W. P. Fung, M. S. Dresselhaus, and M. Endo. Transport properties near the metal-insulator transition in heat-treated activatedrotect carbon fibers. *Phys. Rev. B*, 48(20):14953–14962, Nov 1993. doi:10.1103/PhysRevB.48.14953.

[62] Yunan Gao, Elise Talgorn, Michiel Aerts, M. Tuan Trinh, Juleon M. Schins, Arjan J. Houtepen, and Laurens D. A. Siebbeles. Enhanced hot-carrier cooling and ultrafast spectral diffusion in strongly coupled pbse quantum-dot solids. *Nano Lett.*, 11(12): 5471–5476, Dec 2011. doi:10.1021/nl203235u.

[63] Yunan Gao, C. S. Suchand Sandeep, Juleon M. Schins, Arjan J. Houtepen, and Laurens D. A. Siebbeles. Disorder strongly enhances auger recombination in conductive quantum-dot solids. *Nat Commun*, 4:3329, 2013. doi:10.1038/ncomms3329.

[64] Florencio Garcìa-Santamarà, Yongfen Chen, Javier Vela, Richard D. Schaller, Jennifer A. Hollingsworth, and Victor I. Klimov. Suppressed auger recombination in "giant" nanocrystals boosts optical gain performance. *Nano Letters*, 9(10):3482–3488, 2009. doi:10.1021/nl901681d.

[65] F. García-Santamaría, S. Brovelli, R. Viswanatha, J.A. Hollingsworth, H. Htoon, S.A. Crooker, and V.I. Klimov. Breakdown of volume scaling in auger recombination in cdse/cds heteronanocrystals: The role of the core-shell interface. *Nano Letters*, 11 (2):687–693, 2011. doi:10.1021/nl103801e.

[66] Maria Danielle Garrett, Albert D. Dukes III, James R. McBride, Nathanael J. Smith, Stephen J. Pennycook, and Sandra J. Rosenthal. Band edge recombination in cdse, cds and cdsxse1-x alloy nanocrystals observed by ultrafast fluorescence upconversion: The effect of surface trap states. *The Journal of Physical Chemistry C*, 112(33): 12736–12746, 2008. doi:10.1021/jp803708r.

[67] M.D. Garrett, M.J. Bowers II, J.R. McBride, R.L. Orndorff, S.J. Pennycook, and S.J. Rosenthal. Band edge dynamics in cdse nanocrystals observed by ultrafast fluorescence upconversion. *Journal of Physical Chemistry C*, 112(2):436–442, 2008. doi:10.1021/jp7099306.

[68] J. M. Gérard, B. Sermage, B. Gayral, B. Legrand, E. Costard, and V. Thierry-Mieg. Enhanced spontaneous emission by quantum boxes in a monolithic optical microcavity. *Phys. Rev. Lett.*, 81:1110–1113, Aug 1998. doi:10.1103/PhysRevLett.81.1110.

[69] D. S. Ginger and N. C. Greenham. Charge injection and transport in films of cdse nanocrystals. *Journal of Applied Physics*, 87(3):1361–1368, 2000. doi:10.1063/1.372021.

[70] D.E. Gómez, M. Califano, and P. Mulvaney. Optical properties of single semiconductor nanocrystals. *Physical Chemistry Chemical Physics*, 8(43):4989–5011, 2006. doi:10.1039/b607661k.

[71] Francisco M. Gomez-Campos and Marco Califano. Hole surface trapping in cdse nanocrystals: Dynamics, rate fluctuations, and implications for blinking. *Nano Letters*, 12(9):4508–4517, 2012. doi:10.1021/nl3016279.

[72] Cristina Gomez-Navarro, R. Thomas Weitz, Alexander M. Bittner, Matteo Scolari, Alf Mews, Marko Burghard, and Klaus Kern. Electronic transport properties of individual chemically reduced graphene oxide sheets. *Nano Lett.*, 7(11):3499–3503, 2007. doi:10.1021/n1072090c.

[73] Dmitri K. Gramotnev and Sergey I. Bozhevolnyi. Plasmonics beyond the diffraction limit. *Nat Photon*, 4(2):83–91, February 2010.

[74] Graham B. Griffin, Sandrine Ithurria, Dmitriy S. Dolzhnikov, Alexander Linkin, Dmitri V. Talapin, and Gregory S. Engel. Two-dimensional electronic spectroscopy of cdse nanoparticles at very low pulse power. *The Journal of Chemical Physics*, 138 (1):014705, 2013. doi:10.1063/1.4772465.

[75] L. Guardia, M.J. Fernández-Merino, J.I. Paredes, P. Solís-Fernández, S. Villar-Rodil,

A. Martínez-Alonso, and J.M.D. Tascón. High-throughput production of pristine graphene in an aqueous dispersion assisted by non-ionic surfactants. *Carbon*, 49(5): 1653 – 1662, 2011. doi:10.1016/j.carbon.2010.12.049.

[76] S. Gunasekaran and S. Ponnusamy. Growth and characterization of cadmium magnesium tetra thiocyanate crystals. *Crystal Research and Technology*, 41(2):130–137, 2006. doi:10.1002/crat.200510544.

[77] Lars Gundlach and Piotr Piotrowiak. Femtosecond kerr-gated wide-field fluorescence microscopy. *Opt. Lett.*, 33(9):992–994, May 2008. doi:10.1364/OL.33.000992.

[78] J. A. Gupta, D. D. Awschalom, Al. L. Efros, and A. V. Rodina. Spin dynamics in semiconductor nanocrystals. *Phys. Rev. B*, 66:125307, Sep 2002. doi:10.1103/PhysRevB.66.125307.

[79] P. Guyot-Sionnest, M. Shim, C. Matranga, and M. Hines. Intraband relaxation in cdse quantum dots. *Physical Review B - Condensed Matter and Materials Physics*, 60(4):R2181–R2184, 1999. doi:10.1103/PhysRevB.60.R2181.

[80] Philippe Guyot-Sionnest. Electrical transport in colloidal quantum dot films. *The Journal of Physical Chemistry Letters*, 3(9):1169–1175, May 2012. doi:10.1021/jz300048y.

[81] Philippe Guyot-Sionnest, Brian Wehrenberg, and Dong Yu. Intraband relaxation in cdse nanocrystals and the strong influence of the surface ligands. *The Journal of Chemical Physics*, 123(7):074709, 2005. doi:10.1063/1.2004818.

[82] Philippe Guyot-Sionnest, Dong Yu, Pei-hsun Jiang, and Woowon Kang. Spin blockade in the conduction of colloidal cdse nanocrystal films. *The Journal of Chemical Physics*, 127(1):014702, 2007. doi:10.1063/1.2748765.

[83] Anders. Hagfeldt and Michael. Graetzel. Light-induced redox reactions in nanocrystalline systems. *Chemical Reviews*, 95(1):49–68, 1995. doi:10.1021/cr00033a003.

[84] Daniel C. Hannah, Nicholas J. Dunn, Sandrine Ithurria, Dmitri V. Talapin, Lin X. Chen, Matthew Pelton, George C. Schatz, and Richard D. Schaller. Observation of size-dependent thermalization in cdse nanocrystals using time-resolved photoluminescence spectroscopy. *Phys. Rev. Lett.*, 107:177403, Oct 2011. doi:10.1103/PhysRevLett.107.177403.

[85] Harald F. Hess, Keith DeConde, T. F. Rosenbaum, and G. A. Thomas. Giant dielectric constants at the approach to the insulator-metal transition. *Phys. Rev. B*, 25:5578–5580, Apr 1982. doi:10.1103/PhysRevB.25.5578.

[86] Frederik Hetsch, Ni Zhao, Stephen V. Kershaw, and Andrey L. Rogach. Quantum dot field effect transistors. *Materials Today*, 16(9):312–325, Sep 2013. doi:10.1016/j.mattod.2013.08.011.

[87] Douglas A. Hines and Prashant V. Kamat. Recent advances in quantum dot surface chemistry. *ACS Applied Materials & Interfaces*, 6(5):3041–3057, 2014. doi:10.1021/am405196u.

[88] Margaret A. Hines and Philippe Guyot-Sionnest. Synthesis and characterization of strongly luminescing zns-capped cdse nanocrystals. *The Journal of Physical Chemistry*, 100(2):468–471, 1996. doi:10.1021/jp9530562.

[89] P. P. Ho and R. R. Alfano. Optical kerr effect in liquids. *Phys. Rev. A*, 20(5): 2170–2187, Nov 1979. doi:10.1103/PhysRevA.20.2170.

[90] Gilles Horowitz. Organic field-effect transistors. *Advanced Materials*,

10(5):365–377, 1998. doi:10.1002/(SICI)1521-4095(199803)10:5<365::AID-ADMA365>3.0.CO;2-U.

[91] Arjan J. Houtepen, Daan Kockmann, and Daniel Vanmaekelbergh. Reappraisal of variable-range hopping in quantum-dot solids. *Nano Lett.*, 8(10):3516–3520, Oct 2008. doi:10.1021/nl8020347.

[92] J. Huang, Z. Huang, Y. Yang, H. Zhu, and T. Lian. Multiple exciton dissociation in cdse quantum dots by ultrafast electron transfer to adsorbed methylene blue. *Journal of the American Chemical Society*, 132(13):4858–4864, 2010. doi:10.1021/ja100106z.

[93] Jier Huang, Zhuangqun Huang, Shengye Jin, and Tianquan Lian. Exciton dissociation in cdse quantum dots by hole transfer to phenothiazine. *The Journal of Physical Chemistry C*, 112(49):19734–19738, 2008. doi:10.1021/jp808291u.

[94] Jier Huang, Dave Stockwell, Zhuangqun Huang, Debra L. Mohler, and Tianquan Lian. Photoinduced ultrafast electron transfer from cdse quantum dots to re-bipyridyl complexes. *Journal of the American Chemical Society*, 130(17):5632–5633, 2008. doi:10.1021/ja8003683.

[95] D. Hulin, J. Etchepare, A. Antonetti, L. L. Chase, G. Grillon, A. Migus, and A. Mysyrowicz. Subpicosecond timeresolved luminescence spectroscopy of highly excited cucl. *Applied Physics Letters*, 45(9):993–995, 1984. doi:10.1063/1.95443.

[96] A. Husmann, J. B. Betts, G. S. Boebinger, A. Migliori, T. F. Rosenbaum, and M. L. Saboungi. Megagauss sensors. *Nature*, 417(6887):421–424, 05 2002.

[97] J. Jasieniak, L. Smith, J. Van Embden, P. Mulvaney, and M. Califano. Re-examination

of the size-dependent absorption properties of cdse quantum dots. *Journal of Physical Chemistry C*, 113(45):19468–19474, 2009. doi:10.1021/jp906827m.

[98] Jacek Jasieniak and Paul Mulvaney. From cd-rich to se-rich - the manipulation of cdse nanocrystal surface stoichiometry. *Journal of the American Chemical Society*, 129(10):2841–2848, 2007. doi:10.1021/ja066205a.

[99] Jacek Jasieniak, Marco Califano, and Scott E. Watkins. Size-dependent valence and conduction band-edge energies of semiconductor nanocrystals. *ACS Nano*, 5(7): 5888–5902, 2011. doi:10.1021/nn201681s.

[100] Marcus Jones and Gregory D. Scholes. On the use of time-resolved photoluminescence as a probe of nanocrystal photoexcitation dynamics. *J. Mater. Chem.*, 20(18): 3533–3538, 2010. doi:10.1039/C000165A.

[101] Marcus Jones, Shun S. Lo, and Gregory D. Scholes. Signatures of exciton dynamics and carrier trapping in the time-resolved photoluminescence of colloidal cdse nanocrystals. *The Journal of Physical Chemistry C*, 113(43):18632–18642, 2009. doi:10.1021/jp9078772.

[102] Marcus Jones, Shun S. Lo, and Gregory D. Scholes. Quantitative modeling of the role of surface traps in cdse/cds/zns nanocrystal photoluminescence decay dynamics. *Proceedings of the National Academy of Sciences*, 106(9):3011–3016, 2009. doi:10.1073/pnas.0809316106.

[103] Joshua Jortner. Temperature dependent activation energy for electron transfer between biological molecules. *The Journal of Chemical Physics*, 64(12):4860–4867, 1976. doi:10.1063/1.432142.

[104] C. R. Kagan, C. B. Murray, and M. G. Bawendi. Long-range resonance transfer of

electronic excitations in close-packed cdse quantum-dot solids. *Phys. Rev. B*, 54: 8633–8643, 1996. doi:10.1103/PhysRevB.54.8633.

[105] C.R. Kagan, C.B. Murray, M. Nirmal, and M.G. Bawendi. Electronic energy transfer in CdSe quantum dot solids. *Phys. Rev. Lett.*, 76(9):1517–1520, 1996. doi:10.1103/PhysRevLett.76.1517.

[106] Michael A. Kahlow, Wlodzimierz Jarzęba, Thomas P. DuBruil, and Paul F. Barbara. Ultrafast emission spectroscopy in the ultraviolet by time-gated upconversion. *Review of Scientific Instruments*, 59(7):1098–1109, 1988. doi:http://dx.doi.org/10.1063/1.1139734.

[107] G. Kalyuzhny and R.W. Murray. Ligand effects on optical properties of cdse nanocrystals. *Journal of Physical Chemistry B*, 109(15):7012–7021, 2005. doi:10.1021/jp045352x.

[108] P. Kambhampati. Unraveling the structure and dynamics of excitons in semiconductor quantum dots. *Accounts of Chemical Research*, 44(1):1–13, 2011. doi:10.1021/ar1000428.

[109] Patanjali Kambhampati. Hot exciton relaxation dynamics in semiconductor quantum dots: Radiationless transitions on the nanoscale. *The Journal of Physical Chemistry C*, 115(0):22089–22109, 2011. doi:10.1021/jp2058673.

[110] Evan O. Kane. Band structure of indium antimonide. *Journal of Physics and Chemistry of Solids*, 1(4):249 – 261, 1957. doi:10.1016/0022-3697(57)90013-6.

[111] Moon Sung Kang, Ayaskanta Sahu, David J. Norris, and C. Daniel Frisbie. Size-dependent electrical transport in cdse nanocrystal thin films. *Nano Lett.*, 10(9): 3727–3732, Sep 2010. doi:10.1021/nl102356x.

[112] Moon Sung Kang, Ayaskanta Sahu, David J. Norris, and C. Daniel Frisbie. Size- and temperature-dependent charge transport in pbse nanocrystal thin films. *Nano Lett.*, 11(9):3887–3892, 2011. doi:10.1021/nl2020153.

[113] A. Kawabata. Theory of negative magnetoresistance in three-dimensional systems. *Solid State Communications*, 34(6):431 – 432, 1980.

[114] Arisato Kawabata. Scaling theory of anderson localization. *Progress of Theoretical Physics Supplement*, 84:16–46, 1985. doi:10.1143/PTPS.84.16.

[115] Joseph D. Keene, James R. McBride, Noah J. Orfield, and Sandra J. Rosenthal. Elimination of hole-surface overlap in graded cdsxse1-x nanocrystals revealed by ultrafast fluorescence upconversion spectroscopy. *ACS Nano*, 8(0):10665–10673, 2014. doi:10.1021/nn504235w.

[116] Svetlana V. Kilina, Dmitri S. Kilin, and Oleg V. Prezhdo. Breaking the phonon bottleneck in pbse and cdse quantum dots: Time-domain density functional theory of charge carrier relaxation. *ACS Nano*, 3(1):93–99, 2008. doi:10.1021/nn800674n.

[117] DaeGwi Kim, Shinya Okahara, Masaaki Nakayama, and YongGu Shim. Experimental verification of förster energy transfer between semiconductor quantum dots. *Phys. Rev. B*, 78:153301, Oct 2008. doi:10.1103/PhysRevB.78.153301.

[118] David K. Kim, Yuming Lai, Benjamin T. Diroll, Christopher B. Murray, and Cherie R. Kagan. Flexible and low-voltage integrated circuits constructed from high-performance nanocrystal transistors. *Nature Communications*, 3:1216, Nov 2012. doi:10.1038/ncomms2218.

[119] David K. Kim, Aaron T. Fafarman, Benjamin T. Diroll, Silvia H. Chan, Thomas R. Gordon, Christopher B. Murray, and Cherie R. Kagan. Solution-based stoichiometric

control over charge transport in nanocrystalline cdse devices. *ACS Nano*, 7(10): 8760–8770, 2013. doi:10.1021/nn403132x.

[120] Jin Young Kim, Oleksandr Voznyy, David Zhitomirsky, and Edward H. Sargent. 25th anniversary article: Colloidal quantum dot materials and devices: A quarter-century of advances. *Advanced Materials*, 25(36):4986–5010, 2013. doi:10.1002/adma.201301947.

[121] Tae-Ho Kim, Kyung-Sang Cho, Eun Kyung Lee, Sang Jin Lee, Jungseok Chae, Jung Woo Kim, Do Hwan Kim, Jang-Yeon Kwon, Gehan Amaratunga, Sang Yoon Lee, Byoung Lyong Choi, Young Kuk, Jong Min Kim, and Kinam Kim. Full-colour quantum dot displays fabricated by transfer printing. *Nat Photon*, 5(3):176–182, March 2011.

[122] Tadd C. Kippeny, Michael J. Bowers, II, Albert D. Dukes, III, James R. McBride, Rebecca L. Orndorff, Maria Danielle Garrett, and Sandra J. Rosenthal. Effects of surface passivation on the exciton dynamics of cdse nanocrystals as observed by ultrafast fluorescence upconversion spectroscopy. *The Journal of Chemical Physics*, 128(8):084713, 2008. doi:10.1063/1.2834692.

[123] V. Klimov, P. Haring Bolivar, and H. Kurz. Ultrafast carrier dynamics in semiconductor quantum dots. *Phys. Rev. B*, 53:1463–1467, 1996. doi:10.1103/PhysRevB.53.1463.

[124] V. I. Klimov, D. W. McBranch, C. A. Leatherdale, and M. G. Bawendi. Electron and hole relaxation pathways in semiconductor quantum dots. *Phys. Rev. B*, 60: 13740–13749, Nov 1999. doi:10.1103/PhysRevB.60.13740.

[125] V. I. Klimov, Ch. J. Schwarz, D. W. McBranch, C. A. Leatherdale, and M. G. Bawendi. Ultrafast dynamics of inter- and intraband transitions in semiconductor

nanocrystals: Implications for quantum-dot lasers. *Phys. Rev. B*, 60:R2177, 1999. doi:10.1103/PhysRevB.60.R2177.

[126] V. I. Klimov, A. A. Mikhailovsky, D. W. McBranch, C. A. Leatherdale, and M. G. Bawendi. Mechanisms for intraband energy relaxation in semiconductor quantum dots: The role of electron-hole interactions. *Phys. Rev. B*, 61:R13349–R13352, May 2000. doi:10.1103/PhysRevB.61.R13349.

[127] V. I. Klimov, A. A. Mikhailovsky, Su Xu, A. Malko, J. A. Hollingsworth, C. A. Leatherdale, H.-J. Eisler, and M. G. Bawendi. Optical gain and stimulated emission in nanocrystal quantum dots. *Science*, 290(5490):314–317, 2000. doi:10.1126/science.290.5490.314.

[128] V.I. Klimov. Optical nonlinearities and ultrafast carrier dynamics in semiconductor nanocrystals. *Journal of Physical Chemistry B*, 104(26):6112–6123, 2000. doi:10.1021/jp9944132.

[129] V.I. Klimov, A.A. Mikhailovsky, D.W. McBranch, C.A. Leatherdale, and M.G. Bawendi. Quantization of multiparticle auger rates in semiconductor quantum dots. *Science*, 287(5455):1011–1014, 2000. doi:10.1126/science.287.5455.1011.

[130] Victor I. Klimov. Spectral and dynamical properties of multiexcitons in semiconductor nanocrystals. *Annual Review of Physical Chemistry*, 58(1):635–673, 2007. doi:10.1146/annurev.physchem.58.032806.104537.

[131] Victor I. Klimov, editor. *Nanocrystal Quantum Dots*. CRC Press, 2010.

[132] Kathryn E. Knowles, Daniel B. Tice, Eric A. McArthur, Gemma C. Solomon, and Emily A. Weiss. Chemical control of the photoluminescence of cdse quantum dot-

organic complexes with a series of para-substituted aniline ligands. *Journal of the American Chemical Society*, 132(3):1041–1050, 2010. doi:10.1021/ja907253s.

[133] Kathryn E. Knowles, Eric A. McArthur, and Emily A. Weiss. A multi-timescale map of radiative and nonradiative decay pathways for excitons in cdse quantum dots. *ACS Nano*, 5(3):2026–2035, 2011. doi:10.1021/nn2002689.

[134] Weon-kyu Koh, Sangameshwar R. Saudari, Aaron T. Fafarman, Cherie R. Kagan, and Christopher B. Murray. Thiocyanate-capped pbs nanocubes: Ambipolar transport enables quantum dot based circuits on a flexible substrate. *Nano Lett.*, 11(11): 4764–4767, 2011. doi:10.1021/nl202578g.

[135] Marek Korkusinski, Oleksandr Voznyy, and Pawel Hawrylak. Fine structure and size dependence of exciton and biexciton optical spectra in cdse nanocrystals. *Phys. Rev. B*, 82:245304, Dec 2010. doi:10.1103/PhysRevB.82.245304.

[136] B. Kraabel, A. Malko, J. Hollingsworth, and V. I. Klimov. Ultrafast dynamic holography in nanocrystal solids. *Applied Physics Letters*, 78(13):1814–1816, 2001. doi:10.1063/1.1358365.

[137] Illan J. Kramer and Edward H. Sargent. The architecture of colloidal quantum dot solar cells: Materials to devices. *Chemical Reviews*, 114(1):863–882, Jan 2014. doi:10.1021/cr400299t.

[138] M. Kuno, J. K. Lee, B. O. Dabbousi, F. V. Mikulec, and M. G. Bawendi. The band edge luminescence of surface modified cdse nanocrystallites: Probing the luminescing state. *The Journal of Chemical Physics*, 106(23):9869–9882, 1997. doi:10.1063/1.473875.

[139] Ad Lagendijk, Bart van Tiggelen, and Diederik S. Wiersma. Fifty

years of anderson localization. *Physics Today*, 62(8):24–29, 2009. doi:http://dx.doi.org/10.1063/1.3206091.

[140] C. A. Leatherdale and M. G. Bawendi. Observation of solvatochromism in cdse colloidal quantum dots. *Phys. Rev. B*, 63:165315, Apr 2001. doi:10.1103/PhysRevB.63.165315.

[141] C.A. Leatherdale, W.-K. Woo, F.V. Mikulec, and M.G. Bawendi. On the absorption cross section of cdse nanocrystal quantum dots. *Journal of Physical Chemistry B*, 106(31):7619–7622, 2002. doi:10.1021/jp025698c.

[142] Jong-Soo Lee, Maksym V. Kovalenko, Jing Huang, Dae Sung Chung, and Dmitri V. Talapin. Band-like transport, high electron mobility and high photoconductivity in all-inorganic nanocrystal arrays. *Nat Nano*, 6(6):348–352, 2011. doi:10.1038/nnano.2011.46.

[143] M. Lee, T. F. Rosenbaum, M.-L. Saboungi, and H. S. Schnyders. Band-gap tuning and linear magnetoresistance in the silver chalcogenides. *Phys. Rev. Lett.*, 88:066602, Jan 2002. doi:10.1103/PhysRevLett.88.066602.

[144] Patrick A. Lee and T. V. Ramakrishnan. Disordered electronic systems. *Rev. Mod. Phys.*, 57:287–337, Apr 1985. doi:10.1103/RevModPhys.57.287.

[145] Heng Liu, Alexandre Pourret, and Philippe Guyot-Sionnest. Mott and efros-shklovskii variable range hopping in cdse quantum dots films. *ACS Nano*, 4(9): 5211–5216, Sep 2010. doi:10.1021/nn101376u.

[146] Wenyong Liu, Jong-Soo Lee, and Dmitri V. Talapin. Iii-v nanocrystals capped with molecular metal chalcogenide ligands: High electron mobility and ambipolar

photoresponse. *Journal of the American Chemical Society*, 135(4):1349–1357, 2013. doi:10.1021/ja308200f.

[147] Yao Liu, Markelle Gibbs, Craig L. Perkins, Jason Tolentino, Mohammad H. Zarghami, Jorge Bustamante, and Matt Law. Robust, functional nanocrystal solids by infilling with atomic layer deposition. *Nano Letters*, 11(12):5349–5355, 2011. doi:10.1021/nl2028848.

[148] Yao Liu, Jason Tolentino, Markelle Gibbs, Rachelle Ihly, Craig L. Perkins, Yu Liu, Nathan Crawford, John C. Hemminger, and Matt Law. Pbse quantum dot field-effect transistors with air-stable electron mobilities above 7 cm2 v1 s1. *Nano Letters*, 13 (4):1578–1587, 2013. doi:10.1021/nl304753n.

[149] M. Lorenc, M. Ziolek, R. Naskrecki, J. Karolczak, J. Kubicki, and A. Maciejewski. Artifacts in femtosecond transient absorption spectroscopy. *Applied Physics B: Lasers and Optics*, 74:19–27, 2002. doi:10.1007/s003400100750.

[150] Manuela Lunz, A. Louise Bradley, Wei-Yu Chen, and Yurii K. Gun'ko. Two-dimensional förster resonant energy transfer in a mixed quantum dot monolayer: Experiment and theory. *The Journal of Physical Chemistry C*, 113(8):3084–3088, 2009. doi:10.1021/jp8087034.

[151] Manuela Lunz, A. Louise Bradley, Wei-Yu Chen, Valerie A. Gerard, Stephen J. Byrne, Yurii K. Gun'ko, Vladimir Lesnyak, and Nikolai Gaponik. Influence of quantum dot concentration on förster resonant energy transfer in monodispersed nanocrystal quantum dot monolayers. *Phys. Rev. B*, 81:205316, May 2010. doi:10.1103/PhysRevB.81.205316.

[152] J. M. Luttinger. Quantum theory of cyclotron resonance in semiconductors: General theory. *Phys. Rev.*, 102:1030–1041, May 1956. doi:10.1103/PhysRev.102.1030.

[153] J. M. Luttinger and W. Kohn. Motion of electrons and holes in perturbed periodic fields. *Phys. Rev.*, 97:869–883, Feb 1955. doi:10.1103/PhysRev.97.869.

[154] Abhinandan Makhal, Hongdan Yan, Peter Lemmens, and Samir Kumar Pal. Light harvesting semiconductor core-shell nanocrystals: Ultrafast charge transport dynamics of cdse-zns quantum dots. *The Journal of Physical Chemistry C*, 114(1):627–632, 2010. doi:10.1021/jp908376b.

[155] E. R. Malinowski. *Factor Analysis in Chemistry*. John Wiley & Sons Inc., 3 edition, 2002.

[156] P. Maly, J. Kudrna, F. Trojanek, D. Mikes, P. Nemec, A. C. Maciel, and J. F. Ryan. Dominant role of surface states in photoexcited carrier dynamics in cdse nanocrystalline films prepared by chemical deposition. *Applied Physics Letters*, 77(15): 2352–2354, 2000. doi:10.1063/1.1317536.

[157] P Maly, F Trojanek, T Miyoshi, K Yamanaka, K Luterova, I Pelant, and P Nemec. Ultrafast carrier dynamics in cdse nanocrystalline films on crystalline silicon substrate. *Thin Solid Films*, 403404(0):462 – 466, 2002. doi:10.1016/S0040-6090(01)01542-5.

[158] P. Matousek, M. Towrie, C. Ma, W. M. Kwok, D. Phillips, W. T. Toner, and A. W. Parker. Fluorescence suppression in resonance raman spectroscopy using a high-performance picosecond kerr gate. *Journal of Raman Spectroscopy*, 32(12):983–988, 2001. doi:10.1002/jrs.784.

[159] Allen Miller and Elihu Abrahams. Impurity conduction at low concentrations. *Phys. Rev.*, 120:745–755, Nov 1960. doi:10.1103/PhysRev.120.745.

[160] Jonathan Mooney and Patanjali Kambhampati. Get the basics right: Jacobian conversion of wavelength and energy scales for quantitative analysis of emis-

sion spectra. *The Journal of Physical Chemistry Letters*, 4(19):3316–3318, 2013. doi:10.1021/jz401508t.

[161] Jonathan Mooney, Michael M. Krause, Jonathan I. Saari, and Patanjali Kambhampati. A microscopic picture of surface charge trapping in semiconductor nanocrystals. *The Journal of Chemical Physics*, 138(20):204705, 2013. doi:10.1063/1.4807054.

[162] Jonathan Mooney, Michael M. Krause, Jonathan I. Saari, and Patanjali Kambhampati. Challenge to the deep-trap model of the surface in semiconductor nanocrystals. *Phys. Rev. B*, 87:081201, Feb 2013. doi:10.1103/PhysRevB.87.081201.

[163] Jonathan Mooney, Michael M. Krause, and Patanjali Kambhampati. Connecting the dots: The kinetics and thermodynamics of hot, cold, and surface-trapped excitons in semiconductor nanocrystals. *The Journal of Physical Chemistry C*, 118(14): 7730–7739, 2014. doi:10.1021/jp502102a.

[164] Iwan Moreels, Gabriele Rain, Raquel Gomes, Zeger Hens, Thilo Stferle, and Rainer F. Mahrt. Band-edge exciton fine structure of small, nearly spherical colloidal cdse/zns quantum dots. *ACS Nano*, 5(10):8033–8039, 2011. doi:10.1021/nn202604z.

[165] G. Morello, M. Anni, P.D. Cozzoli, L. Manna, R. Cingolani, and M. De Giorgi. Picosecond photoluminescence decay time in colloidal nanocrystals: The role of intrinsic and surface states. *Journal of Physical Chemistry C*, 111(28):10541–10545, 2007. doi:10.1021/jp072783h.

[166] N. F. Mott. *Conduction in Non-Crystalline Materials*. Oxford University Press, 1987.

[167] N. F. Mott. *Metal Insulator Transitions*. Oxford University Press, 1987.

[168] C.B. Murray, D.J. Norris, and M.G. Bawendi. Synthesis and characterization of nearly monodisperse cde (e = s, se, te) semiconductor nanocrystallites. *Journal of the American Chemical Society*, 115(19):8706–8715, 1993. doi:10.1021/ja00072a025.

[169] R. Nakamura and Y. Kanematsu. Femtosecond spectral snapshots based on electronic optical kerr effect. *Review of Scientific Instruments*, 75(3):636–644, 2004. doi:10.1063/1.1646739.

[170] J. Nanda, S. A. Ivanov, H. Htoon, I. Bezel, A. Piryatinski, S. Tretiak, and V. I. Klimov. Absorption cross sections and auger recombination lifetimes in inverted core-shell nanocrystals: Implications for lasing performance. *Journal of Applied Physics*, 99 (3):034309, 2006. doi:10.1063/1.2168032.

[171] Gustavo A. Narvaez, Gabriel Bester, Alberto Franceschetti, and Alex Zunger. Excitonic exchange effects on the radiative decay time of monoexcitons and biexcitons in quantum dots. *Phys. Rev. B*, 74:205422, Nov 2006. doi:10.1103/PhysRevB.74.205422.

[172] Ute Natura, Oliver Sohr, Rolf Martin, Michael Kahlke, and Gabriele Fasold. Mechanisms of radiation-induced defect generation in fused silica. *Proc. SPIE*, 5273: 155–164, 2004. doi:10.1117/12.521739.

[173] Amanda J. Neukirch, Kim Hyeon-Deuk, and Oleg V. Prezhdo. Time-domain ab initio modeling of excitation dynamics in quantum dots. *Coordination Chemistry Reviews*, 263-264(0):161–181, 2013. doi:10.1016/j.ccr.2013.08.035.

[174] V. L. Nguen, B. Z. Spivak, and B. I. Shklovskii. Tunnel hopping in disordered systems. *Sov. Phys. JETP*, 62:1021, 1985.

[175] M. Nirmal, D.J. Norris, M. Kuno, M.G. Bawendi, Al.L. Efros, and M. Rosen.

Observation of the “dark exciton” in cdse quantum dots. *Physical Review Letters*, 75 (20):3728–3731, 1995. doi:10.1103/PhysRevLett.75.3728.

[176] Susumu Noda, Masayuki Fujita, and Takashi Asano. Spontaneous-emission control by photonic crystals and nanocavities. *Nat Photon*, 1(8):449–458, August 2007.

[177] D. J. Norris. Electronic structure in semiconductor nanocrystals: Optical experiment. In V. I. Klimov, editor, *Nanocrystal Quantum Dots*, chapter 2. CRC Press, 2nd edition, 2010.

[178] D. J. Norris and M. G. Bawendi. Measurement and assignment of the size-dependent optical spectrum in cdse quantum dots. *Phys. Rev. B*, 53:16338–16346, Jun 1996. doi:10.1103/PhysRevB.53.16338.

[179] D. J. Norris, Al. L. Efros, M. Rosen, and M. G. Bawendi. Size dependence of exciton fine structure in cdse quantum dots. *Phys. Rev. B*, 53:16347–16354, Jun 1996. doi:10.1103/PhysRevB.53.16347.

[180] Arthur J Nozik. Spectroscopy and hot electron relaxation dynamics in semiconductor quantum wells and quantum dots. *Annual Review of Physical Chemistry*, 52(1): 193–231, 2001. doi:10.1146/annurev.physchem.52.1.193.

[181] Michel A. Nusimovici, Minko Balkanski, and Joseph L. Birman. Lattice dynamics of wurtzite: Cds. ii. *Phys. Rev. B*, 1(2):595–603, 1970. doi:10.1103/PhysRevB.1.595.

[182] Soong Ju Oh, Nathaniel E. Berry, Ji-Hyuk Choi, E. Ashley Gaulding, Taejong Paik, Sung-Hoon Hong, Christopher B. Murray, and Cherie R. Kagan. Stoichiometric control of lead chalcogenide nanocrystal solids to enhance their electronic and optoelectronic device performance. *ACS Nano*, 7(3):2413–2421, 2013. doi:10.1021/nn3057356.

[183] Anshu Pandey and Philippe Guyot-Sionnest. Slow electron cooling in colloidal quantum dots. *Science*, 322(5903):929–932, 2008. doi:10.1126/science.1159832.

[184] Matthew G. Panthani and Brian A. Korgel. Nanocrystals for electronics. *Annu. Rev. Chem. Biomol. Eng.*, 3(1):287–311, Jul 2012. doi:10.1146/annurev-chembioeng-062011-081040.

[185] M. M. Parish and P. B. Littlewood. Non-saturating magnetoresistance in heavily disordered semiconductors. *Nature*, 426(6963):162–165, 2003. doi:10.1038/nature02073.

[186] Meera M. Parish and Peter B. Littlewood. Classical magnetotransport of inhomogeneous conductors. *Phys. Rev. B*, 72:094417, Sep 2005. doi:10.1103/PhysRevB.72.094417.

[187] Xiaogang Peng, J. Wickham, and A. P. Alivisatos. Kinetics of ii-vi and iii-v colloidal semiconductor nanocrystal growth:"focusing" of size distributions. *Journal of the American Chemical Society*, 120(21):5343–5344, 1998. doi:10.1021/ja9805425.

[188] S. Permogorov. Hot excitons in semiconductors. *physica status solidi (b)*, 68(1): 9–42, 1975. doi:10.1002/pssb.2220680102.

[189] Mark D. Peterson, Laura C. Cass, Rachel D. Harris, Kedy Edme, Kimberly Sung, and Emily A. Weiss. The role of ligands in determining the exciton relaxation dynamics in semiconductor quantum dots. *Annual Review of Physical Chemistry*, 65 (1):317–339, 2014. doi:10.1146/annurev-physchem-040513-103649.

[190] Lisa V. Poulikakos, Ferry Prins, and William A. Tisdale. Transition from thermodynamic to kinetic-limited excitonic energy migration in colloidal quantum dot solids. *The Journal of Physical Chemistry C*, 118(15):7894–7900, 2014. doi:10.1021/jp502961v.

[191] S. S. Prabhu, A. S. Vengurlekar, S. K. Roy, and Jagdeep Shah. Nonequilibrium dynamics of hot carriers and hot phonons in cdse and gaas. *Phys. Rev. B*, 51: 14233–14246, May 1995. doi:10.1103/PhysRevB.51.14233.

[192] Vladimir Prigodin and Arthur Epstein. Comment on voltage-induced metal-insulator transition in polythiophene field-effect transistors. *Physical Review Letters*, 98(25): 259703, Jun 2007. doi:10.1103/physrevlett.98.259703.

[193] E. M. Purcell. Proceedings of the american physical society. *Phys. Rev.*, 69(11-12): 681, Jun 1946. doi:10.1103/PhysRev.69.674.2.

[194] Lianhua Qu and Xiaogang Peng. Control of photoluminescence properties of cdse nanocrystals in growth. *Journal of the American Chemical Society*, 124(9):2049–2055, 2002. doi:10.1021/ja017002j.

[195] Gabriele Raino, Iwan Moreels, Antti Hassinen, Thilo Stoferle, Zeger Hens, and Rainer F. Mahrt. Exciton dynamics within the band-edge manifold states: The onset of an acoustic phonon bottleneck. *Nano Letters*, 12(10):5224–5229, 2012. doi:10.1021/nl302390b.

[196] Peter Reiss, Myriam Protiére, and Liang Li. Core/shell semiconductor nanocrystals. *Small*, 5(2):154–168, 2009. doi:10.1002/smll.200800841.

[197] István Robel, Vaidyanathan Subramanian, Masaru Kuno, and Prashant V. Kamat. Quantum dot solar cells. harvesting light energy with cdse nanocrystals molecularly linked to mesoscopic tio2 films. *Journal of the American Chemical Society*, 128(7): 2385–2393, 2006. doi:10.1021/ja056494n.

[198] István Robel, Masaru Kuno, and Prashant V. Kamat. Size-dependent electron

injection from excited cdse quantum dots into tio2 nanoparticles. *Journal of the American Chemical Society*, 129(14):4136–4137, 2007. doi:10.1021/ja070099a.

[199] J. Robertson. Amorphous carbon. *Advances in Physics*, 35(4):317–374, 1986.

[200] J. Robertson. High dielectric constant oxides. *The European Physical Journal - Applied Physics*, 28:265–291, 12 2004. doi:10.1051/epjap:2004206.

[201] Emil Roduner. Size matters: why nanomaterials are different. *Chem. Soc. Rev.*, 35: 583–592, 2006. doi:10.1039/B502142C.

[202] Hugo Romero and Marija Drndic. Coulomb blockade and hopping conduction in Pbse quantum dots. *Physical Review Letters*, 95(15):156801, Oct 2005. doi:10.1103/physrevlett.95.156801.

[203] C. Ruckebusch, M. Sliwa, P. Pernot, A. de Juan, and R. Tauler. Comprehensive data analysis of femtosecond transient absorption spectra: A review. *Journal of Photochemistry and Photobiology C: Photochemistry Reviews*, 13(1):1 – 27, 2012. doi:http://dx.doi.org/10.1016/j.jphotochemrev.2011.10.002.

[204] Jonathan I. Saari, Eva A. Dias, Danielle Reifsnyder, Michael M. Krause, Brenna R. Walsh, Christopher B. Murray, and Patanjali Kambhampati. Ultrafast electron trapping at the surface of semiconductor nanocrystals: Excitonic and biexcitonic processes. *The Journal of Physical Chemistry B*, 117(0):4412–4421, 2013. doi:10.1021/jp307668g.

[205] D.M. Sagar, R.R. Cooney, S.L. Sewall, E.A. Dias, M.M. Barsan, I.S. Butler, and P. Kambhampati. Size dependent, state-resolved studies of exciton-phonon couplings in strongly confined semiconductor quantum dots. *Physi-*

cal Review B - Condensed Matter and Materials Physics, 77(23):235321, 2008. doi:10.1103/PhysRevB.77.235321.

[206] B. Schmidt, S. Laimgruber, W. Zinth, and P. Gilch. A broadband kerr shutter for femtosecond fluorescence spectroscopy. *Applied Physics B: Lasers and Optics*, 76: 809–814, 2003. doi:10.1007/s00340-003-1230-7.

[207] Samuel L. Sewall, Ryan R. Cooney, and Patanjali Kambhampati. Experimental tests of effective mass and atomistic approaches to quantum dot electronic structure: Ordering of electronic states. *Applied Physics Letters*, 94(24):243116, 2009. doi:10.1063/1.3157269.

[208] Samuel L. Sewall, Ryan R. Cooney, Eva A. Dias, Pooja Tyagi, and Patanjali Kambhampati. State-resolved observation in real time of the structural dynamics of multiexcitons in semiconductor nanocrystals. *Phys. Rev. B*, 84:235304, Dec 2011. doi:10.1103/PhysRevB.84.235304.

[209] S.L. Sewall, R.R. Cooney, K.E.H. Anderson, E.A. Dias, and P. Kambhampati. State-to-state exciton dynamics in semiconductor quantum dots. *Physical Review B - Condensed Matter and Materials Physics*, 74(23):235328, 2006. doi:10.1103/PhysRevB.74.235328.

[210] S.L. Sewall, A. Franceschetti, R.R. Cooney, A. Zunger, and P. Kambhampati. Direct observation of the structure of band-edge biexcitons in colloidal semiconductor cdse quantum dots. *Physical Review B - Condensed Matter and Materials Physics*, 80(8): –, 2009. doi:10.1103/PhysRevB.80.081310.

[211] Andrew Shabaev, Alexander L. Efros, and Alexei L. Efros. Dark and photoconductivity in ordered array of nanocrystals. *Nano Letters*, 13(11):5454–5461, Nov 2013. doi:10.1021/nl403033f.

[212] J. Shah. Ultrafast luminescence spectroscopy using sum frequency generation. *Quantum Electronics, IEEE Journal of*, 24(2):276–288, Feb 1988. doi:10.1109/3.124.

[213] Yasuhiro Shirasaki, Geoffrey J. Supran, Moungi G. Bawendi, and Vladimir Bulovic. Emergence of colloidal quantum-dot light-emitting technologies. *Nat Photon*, 7(1): 13–23, 2013. doi:10.1038/nphoton.2012.328.

[214] A.L. Shklovskii, B.I.; Efros. *Electronic Properties of Doped Semiconductors*. Springer Verlag, 1984.

[215] U. Sivan, O. Entin-Wohlman, and Y. Imry. Orbital magnetoconductance in the variable-range¡i¿¡/i¿hopping regime. *Phys. Rev. Lett.*, 60:1566–1569, Apr 1988. doi:10.1103/PhysRevLett.60.1566.

[216] Brian Skinner, Tianran Chen, and B. I. Shklovskii. Theory of hopping conduction in arrays of doped semiconductor nanocrystals. *Phys. Rev. B*, 85:205316, May 2012. doi:10.1103/PhysRevB.85.205316.

[217] V. N. Soloviev, A. Eichhöfer, D. Fenske, and U. Banin. Molecular limit of a bulk semiconductor: size dependence of the band gap in cdse cluster molecules. *Journal of the American Chemical Society*, 122(11):2673–2674, 2000. doi:10.1021/ja9940367.

[218] Aike Stortelder, Joost B. Buijs, Jaap Bulthuis, Cees Gooijer, and Gert van der Zwan. Fast-gated intensified charge-coupled device camera to record time-resolved fluorescence spectra of tryptophan. *Appl. Spectrosc.*, 58(6):705–710, Jun 2004.

[219] Martin Störzer, Peter Gross, Christof M. Aegerter, and Georg Maret. Observation of the critical regime near anderson localization of light. *Phys. Rev. Lett.*, 96:063904, Feb 2006. doi:10.1103/PhysRevLett.96.063904.

[220] J. Takeda, K. Nakajima, S. Kurita, S. Tomimoto, S. Saito, and T. Suemoto. Time-resolved luminescence spectroscopy by the optical kerr-gate method applicable to ultrafast relaxation processes. *Phys. Rev. B*, 62(15):10083–10087, Oct 2000. doi:10.1103/PhysRevB.62.10083.

[221] Dmitri V. Talapin and Christopher B. Murray. Pbse nanocrystal solids for n- and p-channel thin film field-effect transistors. *Science*, 310(5745):86–89, 2005. doi:10.1126/science.1116703.

[222] Dmitri V. Talapin, Jong-Soo Lee, Maksym V. Kovalenko, and Elena V. Shevchenko. Prospects of colloidal nanocrystals for electronic and optoelectronic applications. *Chemical Reviews*, 110(1):389–458, Jan 2010. doi:10.1021/cr900137k.

[223] Elise Talgorn, Yunan Gao, Michiel Aerts, Lucas T. Kunneman, Juleon M. Schins, SavenijeT. J., van HuisMarijn A., van der ZantHerre S. J., Arjan J. Houtepen, and Laurens D. A. Siebbeles. Unity quantum yield of photogenerated charges and band-like transport in quantum-dot solids. *Nat Nano*, 6(11):733–739, 2011. doi:10.1038/nnano.2011.159.

[224] Vasily V. Temnov. Ultrafast acousto-magneto-plasmonics. *Nat Photon*, 6(11):728–736, November 2012.

[225] William A. Tisdale, Kenrick J. Williams, Brooke A. Timp, David J. Norris, Eray S. Aydil, and X.-Y. Zhu. Hot-electron transfer from semiconductor nanocrystals. *Science*, 328(5985):1543–1547, 2010. doi:10.1126/science.1185509.

[226] Michael E. Turk, Ji-Hyuk Choi, Soong Ju Oh, Aaron T. Fafarman, Benjamin T. Diroll, Christopher B. Murray, Cherie R. Kagan, and James M. Kikkawa. Gate-induced carrier delocalization in quantum dot field effect transistors. *Nano Letters*, 14(10): 5948–5952, 2014. doi:10.1021/nl5029655.

[227] Michael E. Turk, Patrick M. Vora, Aaron T. Fafarman, Benjamin T. Diroll, Christopher B. Murray, Cherie R. Kagan, and James M. Kikkawa. Ultrafast electron trapping in ligand-exchanged quantum dot assemblies. *ACS Nano*, 9(2):1440–1447, 2015. doi:10.1021/nn505862g.

[228] Kevin Tvrdy and Prashant V. Kamat. Substrate driven photochemistry of cdse quantum dot films: Charge injection and irreversible transformations on oxide surfaces. *The Journal of Physical Chemistry A*, 113(16):3765–3772, 2009. doi:10.1021/jp808562x.

[229] D.F. Underwood, T. Kippeny, and S.J. Rosenthal. Ultrafast carrier dynamics in cdse nanocrystals determined by femtosecond fluorescence upconversion spectroscopy. *Journal of Physical Chemistry B*, 105(2):436–443, 2001. doi:10.1021/jp003088b.

[230] J. van Embden, J. Jasieniak, D. E. Gómez, P. Mulvaney, and M. Giersig. Review of the synthetic chemistry involved in the production of core/shell semiconductor nanocrystals. *Aust. J. Chem.*, 60(7):457–471, 2007.

[231] Lambert K. van Vugt, Brian Piccione, Chang-Hee Cho, Carlos Aspetti, Aaron D. Wirshba, and Ritesh Agarwal. Variable temperature spectroscopy of as-grown and passivated cds nanowire optical waveguide cavities. *The Journal of Physical Chemistry A*, 115(16):3827–3833, 2011. doi:10.1021/jp108167t.

[232] Danil Vanmaekelbergh and Peter Liljeroth. Electron-conducting quantum dot solids: novel materials based on colloidal semiconductor nanocrystals. *Chemical Society Reviews*, 34(4):299, 2005. doi:10.1039/b314945p.

[233] J. Vavro, J. M. Kikkawa, and J. E. Fischer. Metal-insulator transition in doped single-wall carbon nanotubes. *Phys. Rev. B*, 71(15):155410, 2005. doi:10.1103/PhysRevB.71.155410.

[234] J. von Frese, S. A. Kovalenko, and N. P. Ernsting. Interactive curve resolution by using latent projections in polar coordinates. *Journal of Chemometrics*, 21(1-2):2–9, 2007. doi:10.1002/cem.1008.

[235] P. M. Vora, P. Gopu, M. Rosario-Canales, C. R. Pérez, Y. Gogotsi, J. J. Santiago-Avilés, and J. M. Kikkawa. Correlating magnetotransport and diamagnetism of sp^2-bonded carbon networks through the metal-insulator transition. *Phys. Rev. B*, 84: 155114, Oct 2011. doi:10.1103/PhysRevB.84.155114.

[236] Jianpu Wang and Neil C. Greenham. Charge transport in colloidal ZnO nanocrystal solids: The significance of surface states. *Appl. Phys. Lett.*, 104(19):193111, May 2014. doi:10.1063/1.4878257.

[237] Lin-Wang Wang and Alex Zunger. Pseudopotential calculations of nanoscale cdse quantum dots. *Phys. Rev. B*, 53:9579–9582, Apr 1996. doi:10.1103/PhysRevB.53.9579.

[238] Xiaoyong Wang, Xiaofan Ren, Keith Kahen, Megan A. Hahn, Manju Rajeswaran, Sara Maccagnano-Zacher, John Silcox, George E. Cragg, Alexander L. Efros, and Todd D. Krauss. Non-blinking semiconductor nanocrystals. *Nature*, 459(7247): 686–689, June 2009.

[239] R.L. Weaver. Anderson localization of ultrasound. *Wave Motion*, 12(2):129 – 142, 1990. doi:http://dx.doi.org/10.1016/0165-2125(90)90034-2.

[240] Damon A. Wheeler and Jin Z. Zhang. Exciton dynamics in semiconductor nanocrystals. *Advanced Materials*, 25:2878–2896, 2013. doi:10.1002/adma.201300362.

[241] Diederik S. Wiersma, Paolo Bartolini, Ad Lagendijk, and Roberto Righini. Local-

ization of light in a disordered medium. *Nature*, 390(6661):671–673, December 1997.

[242] Cathy Y. Wong and Gregory D. Scholes. Using two-dimensional photon echo spectroscopy to probe the fine structure of the ground state biexciton of cdse nanocrystals. *Journal of Luminescence*, 131(3):366 – 374, 2011. doi:10.1016/j.jlumin.2010.09.015. Selected papers from DPC'10.

[243] Sander F. Wuister, Celso de Mello Donega, and Andries Meijerink. Influence of thiol capping on the exciton luminescence and decay kinetics of cdte and cdse quantum dots. *J. Phys. Chem. B*, 108(45):17393–17397, 2004. doi:10.1021/jp047078c.

[244] R. Xu, A. Husmann, T. F. Rosenbaum, M. L. Saboungi, J. E. Enderby, and P. B. Littlewood. Large magnetoresistance in non-magnetic silver chalcogenides. *Nature*, 390(6655):57–60, 11 1997.

[245] S. Xu, A. A. Mikhailovsky, J. A. Hollingsworth, and V. I. Klimov. Hole intraband relaxation in strongly confined quantum dots: Revisiting the "phonon bottleneck" problem. *Phys. Rev. B*, 65:045319, Jan 2002. doi:10.1103/PhysRevB.65.045319.

[246] C. H. Yang, Jean M. Carlson-Swindle, S. A. Lyon, and J. M. Worlock. Hot-electron relaxation in gaas quantum wells. *Phys. Rev. Lett.*, 55(21):2359–2361, Nov 1985. doi:10.1103/PhysRevLett.55.2359.

[247] Jun Yang and Frank W. Wise. Effects of disorder on electronic properties of nanocrystal assemblies. *The Journal of Physical Chemistry C*, 119(6):3338–3347, 2015. doi:10.1021/jp5098469.

[248] Dong Yu, Congjun Wang, and Philippe Guyot-Sionnest. n-type con-

ducting cdse nanocrystal solids. *Science*, 300(5623):1277–1280, 2003. doi:10.1126/science.1084424.

[249] Dong Yu, Congjun Wang, Brian L. Wehrenberg, and Philippe Guyot-Sionnest. Variable range hopping conduction in semiconductor nanocrystal solids. *Phys. Rev. Lett.*, 92:216802, May 2004. doi:10.1103/PhysRevLett.92.216802.

[250] W.W. Yu, L. Qu, W. Guo, and X. Peng. Experimental determination of the extinction coefficient of cdte, cdse, and cds nanocrystals. *Chemistry of Materials*, 15(14): 2854–2860, 2003. doi:10.1021/cm034081k.

[251] Zhihao Yu, Lars Gundlach, and Piotr Piotrowiak. Efficiency and temporal response of crystalline kerr media in collinear optical kerr gating. *Opt. Lett.*, 36(15):2904–2906, Aug 2011. doi:10.1364/OL.36.002904.

[252] Amir Zabet-Khosousi, Paul-Emile Trudeau, Yoshinori Suganuma, Al-Amin Dhirani, and Bryan Statt. Metal to insulator transition in films of molecularly linked gold nanoparticles. *Physical Review Letters*, 96(15):156403, Apr 2006. doi:10.1103/physrevlett.96.156403.

[253] Jingshan Zhang and Boris I. Shklovskii. Density of states and conductivity of a granular metal or an array of quantum dots. *Phys. Rev. B*, 70:115317, Sep 2004. doi:10.1103/PhysRevB.70.115317.

[254] H. Zhu, N. Song, and T. Lian. Wave function engineering for ultrafast charge separation and slow charge recombination in type ii core/shell quantum dots. *Journal of the American Chemical Society*, 133(22):8762–8771, 2011. doi:10.1021/ja202752s.